UNIVERSITÀ DEGLI STUDI DI PADOVA

Dipartimento di Ingegneria Industriale DII
Corso di Laurea Magistrale in Ingegneria Aerospaziale

TESI DI LAUREA

DESIGN OF A COMPOSITE OXIDIZER TANK FOR A HYBRID SOUNDING ROCKET

Relatore: Prof. Pavarin Daniele
Correlatore: PhD Barato Francesco

Laureando: Manuel Stella

Anno Accademico 2018-2019

Abstract

In 2019, the University of Padua, relying on its spin-off company *T4i* - *"Technology for Propulsion and Innovation"*, began the development of a sounding rocket propelled by a hybrid system which uses a grain of paraffin as a solid fuel and liquid hydrogen peroxide as oxidizer. The goal of the project is to design and manufacture the rocket so that, by the beginning of 2020, a flight campaign can be set up. The first launch target is an altitude of about 10 km in order to validate the hybrid engine technology, later on, the target will be set at higher altitudes with high scientific interest. The author of this thesis took part in the design of the fluidic line and, particularly , in conceiving the tank that contains the liquid oxidizer. The entire development process of this structural component is described in this thesis, whose objective is to provide requirements, design and sizing that led to the realization of the first prototype, ready to be tested. The innovation introduced in this type of component compared to the state of the art, is the use of carbon fiber composite materials without the presence of a metallic or plastic liner inside the tank itself. In the test phase, therefore, it will be important to evaluate both the structural integrity of the tank subjected to internal pressure, and the absence of leakage from the walls and closing domes. The thesis is divided into 5 parts: the introduction contains a general description of sounding rockets, hybrid rocket systems and the use of composites in this field; the following chapter describes the sounding rocket developed in the project and the fluidic subsystem; the third chapter delineates the structural pre-dimensioning made by a *Matlab* code; in the fourth chapter are contained requirements and design of the oxidizer tank; the conclusion summarizes the results of the thesis.

Sommario

Nel 2019 l'Università di Padova, appoggiandosi alla sua compagnia spin-off *T4i - "Technology for Propulsion and Innovation"*, ha iniziato lo sviluppo di un razzo sonda spinto da un sistema ibrido il quale utilizza un grano di paraffina come combustibile solido e perossido di idrogeno liquido come ossidante. L'obiettivo del progetto è quello di progettare e costruire il razzo affinché, con l'inizio del 2020, si possa dare inizio ad una campagna di volo. Il primo lancio si pone come target un'altitudine di circa 10 km allo scopo di validare la tecnologia ibrida messa a punto, in seguito si punterà ad altitudini maggiori ad alto interesse scientifico. L'autore di questa tesi ha partecipato alla progettazione della linea fluidica ed, in dettaglio, all'ideazione del serbatoio che contiene l'ossidante liquido. L'intero iter di sviluppo di questo componente strutturale viene descritto in questa tesi, il cui obiettivo è fornire requisiti, design e dimensionamenti che hanno portato alla realizzazione del primo prototipo pronto per essere testato. L'innovazione introdotta in questo tipo di componente rispetto allo stato dell'arte è l'utilizzo dei materiali compositi in fibra di carbonio senza la presenza di un liner metallico o plastico all'interno del serbatoio stesso. In fase di test, quindi, sarà importante valutare sia l'integrità strutturale del serbatoio sottoposto a pressione interna, sia la tenuta delle pareti e dei fondelli di chiusura. La tesi è divisa in 5 parti:l'introduzione contiene una descrizione generale dei razzi-sonda, dei sistemi a razzo ibridi e dell'utilizzo dei compositi in questo campo; il capitolo successivo descrive il razzo-sonda e il sottosistema della fluidica; nel terzo capitolo si spiega il primo pre-dimensionamento strutturale tramite codice *Matlab*; nel quarto capitolo sono contenuti requisiti e dimensionamento del serbatoio; infine, la conclusione riassume i risultati della tesi.

List of Figures

List of Tables

Contents

Chapter 1

Introduction

1.1 Sounding Rockets

A sounding rocket (also known as research rocket) is a sub-orbital rocket used for scientific measures and experiments [6]. Being sub-orbital carriers, sounding rockets follow a parabolic trajectory and don't end up orbiting around the earth. Due to this characteristics since the late 1950s they have been used mainly for meteorological and upper atmosphere studies. These rockets take their name from the nautical name "to sound", which means "to take measurements".

They are generally made up of 3 major parts: the propulsion system (generally solid or, recently, hybrid), the service system (rate control, telemetry module, recovery system), and the scientific payload (carrying the instruments to conduct measurements or experiments).

In the last decades sounding rockets have become increasingly popular for the following reasons:

- *They provide unique conditions for scientific research*: the parabolic motion at high altitude is useful for peculiar scientific experiments and measurements (as in geophysical and meteorological research). The propulsion system can separete from the payload once the propellant is depleted. The latter continues to fly in space in a low microgravity environment (generally lasting between 5 and 20 minutes) allowing experiments and measurements to take place. Generally the payload lands safely on Earth by means of a parachute and is therefore recovered.

- *They provide a relatively easy, quick and cheap access to space*: not going into orbit, a sounding rocket doent't need a particularly complex propulsion system and telemetry. Payload recovery is possible, meaning that experimentation and payload development costs can be spread over multiple missions.

- *They are useful for devices validation and new technologies development*: sounding rockets provide an efficient way to test new systems and devices. Relatively low costs also promote innovation: non-sufficiently developed instruments and technologies are generally too risky to be tested in an expensive, full-blown satellite-program, so they are previously tested on a sounding rocket.

- *Learning*: sounding rockets are excellent learning opportunities for students and novice engineers to follow a research project in all its phases, building precious experience for a future career.

1.2 Hybrid Propulsion

Three main types of chemical rocket exist: liquid, solid and hybrids. The subdivision is related to the phase which the propellant is stored. In a liquid rocket the liquid oxidizer and the fuel are stored in the respective tanks and injected in the combustion chamber. In a solid rocket the fuel and oxidizer are mixed together in a solid matrix that is stored directly in the combustion chamber. However in a more general term is possible to consider like a liquid rocket also system were the propellant is stored in a gaseous or gelled form and is injected in the combustion chamber afterward.[2]

In an hybrid rocket one component is stored as a liquid (or a gas or a gel) in a tank and the other is a solid placed inside the combustion chamber. Usually the liquid is the oxidizer and the solid is the fuel, the so called classical configuration. However also reverse hybrid could exist were the liquid is the fuel and the solid is the oxidizer. The most part of the work up to now (and almost surely in the future) regards the classical scheme mainly because liquid oxidizers have higher energetic content than solid ones. Exceptions are cryogenic solids oxidizers like solid oxygen, the solidified version of liquid oxygen. However solid cryogenic storage is even more complex than its liquid counterpart. Moreover an almost infinite combination of solid fuels exists for hybrid propulsion while generally the choice of oxidizer is much limited (both in solid and liquid phase) and in this case the manufacturing of the grain requires a binder. No particular advantages seem to come from the reverse approach.

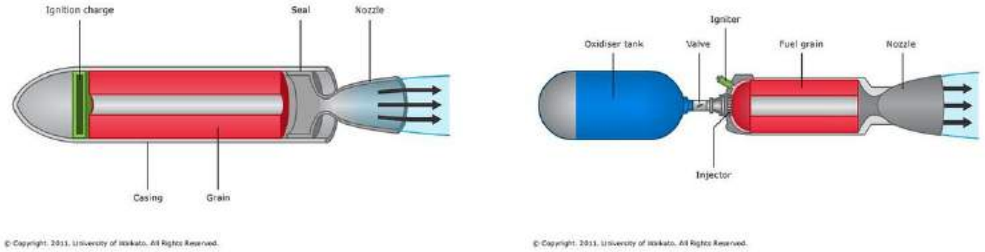

(a) Solid (b) Hybrid

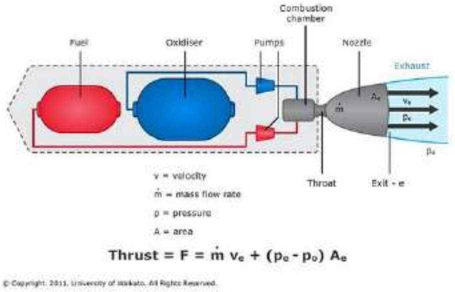

(c) Liquid

Figure 1.1: Solid, hybrid and liquid rocket schematic.

Solid and liquid engine have monopolized the military and commercial market up to know leaving hybrids only a limited room in research program (and more recently in amateur/academic activities). The reason for that is related to the peculiar characteristics of the three propulsion systems coupled with the requirements of the cold war era. Solid rocket are very simple, ready to launch and could reach the highest value of impulse density making them ideal for volume constrained applications such as military weapons, sounding rockets and boosters. Liquids can reach the highest specific impulse; they can be stopped and started multiple times in flight making them ideal for launchers and spacecraft. Hybrids have long been considered an intermediate case between the two, so not showing a clear advantage respect to both extremes in a performances oriented environment. Moreover the greatest advancement of rocket propulsion have been done in the 50-60. In that period almost everything has been designed and tested. After an initial assessment only the most promising technology have been chosen for extensive further work. Some hybrid issues were still not solved at that time (and partially today). Hybrids maturity, as other propulsion technologies still suffer nowadays for being excluded from that choice. In fact after the golden age of space investments have been decreased and this prevents today hybrids to make a considerable step toward maturity. Anyway the space business has been slowly changing in the last decades (and it is expected to change even more in the future, hopefully). Today more attention is paid toward safety,reliability, cost, and environmental friendliness. This in turn has paved the way for a renewed interest for hybrid propulsion favored by its inherent characteristics. First of all is necessary to highlight that hybrid rocket combustion is much different from solid or liquid rocket combustion. In a solid rocket the fuel and the oxidizer are intimately pre-mixed in the grain at a specific O/F ratio. The propellant burns with a thin flame next to the surface (few µm). The amount of propellant depends on the linear regression of the grain surface that generally in turns depends on chamber pressure. In a liquid rocket the oxidizer and the fuel are injected in the combustion chamber. The average O/F ratio is dependent simply on the ratio between the two mass flows. In a hybrid rocket the oxidizer is usually injected at the head end of the combustion chamber mixing later with the pyrolized fuels in a macroscopic turbulent diffusion flame. The regression of the fuel is dependent of the convective heat exchange from the flame to the surface. In a liquid rocket the total mass flow and O/F ratio can be perfectly (at least nominally) controlled. In a solid rocket the O/F ratio is fixed by the grain composition and the propellant mass flow being dependent only on chamber pressure can be defined with a proper design of the fuel grain. For both propulsion systems the motor O/F ratio and propellant mass flow are independent variables. On the contrary only the oxidizer mass flow can be directly controlled in a hybrid rocket, while the fuel mass flow is dependent on the complex physic of its coupled fluid dynamic/combustion. The regression rate in a hybrid has a time and space variability. The motor O/F ratio and total mass flow are not independent variables. This complex coupling between motor parameters, the difficult prediction/scaling and the space variability of hybrid regression makes hybrid physics and design more complex/difficult to deal with. This added complexity has always hampered the realization of a competitive hybrid rocket unit. Moreover in a liquid rocket motor the oxidizer and fuel are intimately mixed in the vicinity of the injector to form a combustible mixture. As already said in a solid rocket the two components are already mixed in a single solid phase. In both case, therefore a uniform mixture is achieved in the combustion chamber. In a hybrid motor the oxidizer and the fuel enter the chamber from different sides, mixing slowly in the diffusion flame. This characteristic is also responsible for the usually lower performances of hybrid rockets. However due to its peculiar characteristics hybrid propulsion presents several advantages compared to solids and liquids. Here's a general list:

- *Safety*: the fuel is inert and can be manufactured, transported, and handled safely as standard commercial products. The system is non-explosive because an intimate mixture of oxidizer and fuel is not possible. NASA classifies hybrid LOX-HTPB (liquid oxygen/hydroxyl-terminated polybutadiene combination as 0 TNT equivalent. In case of an abort procedure the motor can be stopped turning off the liquid flow. Unlike solid rockets, fuel grain cracks are not catastrophic because burning occurs only when the fuel encounters the oxidizer flow. Hybrid combustion is diffusion controlled so it's usually not pressure-sensitive as in liquid and solid systems. This in turn makes hybrid propulsion less prone to catastrophic failures due to thermoacoustic instabilities or other parameters shifting outside nominal conditions. Hybrid failures are usually benign in nature.

- *Reliability*: a hybrid rocket requires roughly only half of the components of a liquid motor. Compared to solid motors, the grain is much more insensitive to defects. Being diffusion-controlled, hybrid combustion is more tolerant than in both solid and liquid rockets.

- *Mass flow control*: the engine can be throttled by modulating only the liquid flow rate. This is simpler than in liquid propulsion where two liquids have to be modulated simultaneously. This doesn't require only double plumbing but also synchronization between the two flows. The engine can be started and stopped several times if a suitable ignition system is used.

- *Propellant versatility*: the selection of propellants is (nominally) much greater than with either solid or liquid systems. However, the focus has been directed to a narrower band of combinations. Liquid oxidizers are more energetic than solid oxidizers used in solid propulsion. Metals particles can be added easily in a solid matrix to improve performances liquid systems, where the formation of slurries implies several drawbacks, such as sedimentation and issues in feeding-pressurization and atomization.

- *Temperature sensitivity*: because the temperature effect on the burning rate is small (as in liquid systems), ambient launch temperature variations have little effect on operating chamber pressure. Thus, the concern (typical for solid rockets) in designing for a maximum expected operating pressure (MEOP) is greatly reduced (this claim is partially negated in case of self-pressurized oxidizer).

- *Propellant specific impulse and density*: hybrid rockets have a theoretical specific impulse higher than solid ones and comparable to liquid ones, except for those using cryogenic fuels. With the addition of metals in the fuel grain the specific impulse of hybrid systems can be even higher than the one of liquid rockets of the same class. Indeed, the highest possible experimental has been achieved with a tribrid configuration. The density impulse is lower compared to solid systems, but nominally higher compared to liquid ones, particularly for metal loaded fuels.

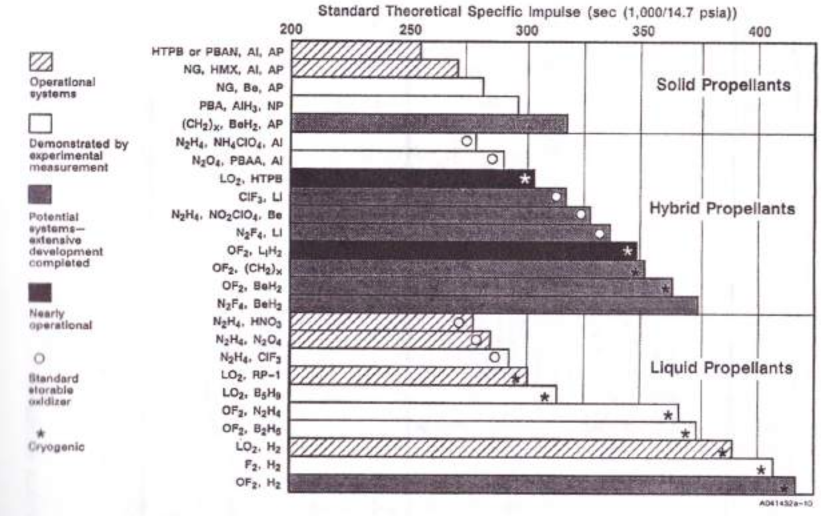

Figure 1.2: Theoretical I_{sp} for solid, liquid and hybrid rocket propellants.

- *Low cost*: considering the components composing the inert mass fraction of a rocket propulsion system the cost of a hybrid should stay between the more complex and expensive liquid systems and the simpler and cheaper solid ones. However, the total operational costs of a hybrid should take advantage of its safety characteristics and inert propellant. Manufacture of the fuel can be done in a commercial facility that does not require the large areas and many solid-propellant manufacturing facilities. Furthermore, the system can tolerate large design margins, resulting in lower fabrication costs. Transport and handling costs are greatly reduced.

- *Low environmental impact*: several low-polluting propellant combinations are possible for hybrid propulsion; many of them have been commonly used.

Unfortunately, hybrid rockets have also some distinct disadvantages, such as:

- *Low regression rate*: hybrid systems are generally characterized by low regression rates. This in turn requires a large burning area to achieve the required thrust. This large area could be obtained with a very long combustion chamber resulting in a too long motor. Moreover, the resulting web thickness is small concurring to a very poor volume loading (fuel volume/total volume). The problem is increased with scale-up for several reasons. First, the port area is proportional to the thrust while the web thickness is proportional to the product of the burning time with the average regression rate. Usually, burning time increases with scale-up much more slowly than thrust, resulting in a much higher ratio between internal diameter and web thickness. Moreover, hybrid regression rate decreases with scaling, exacerbating the issue. A better alternative is the use of a multiport grain. However, multiport design implies several other problems, like high residuals, deviations of regression rate for different ports, change of the port shape with time, structural issues (e.g. need for web support), generally higher O/F shift than single port design (even stronger if merging of ports is allowed), increased complexity and manufacturing costs. Several ways to increase the regression rate have been proposed and tested; almost no one has reached operational status, but some of them present an interesting potential for the future, particularly for up to medium scales.

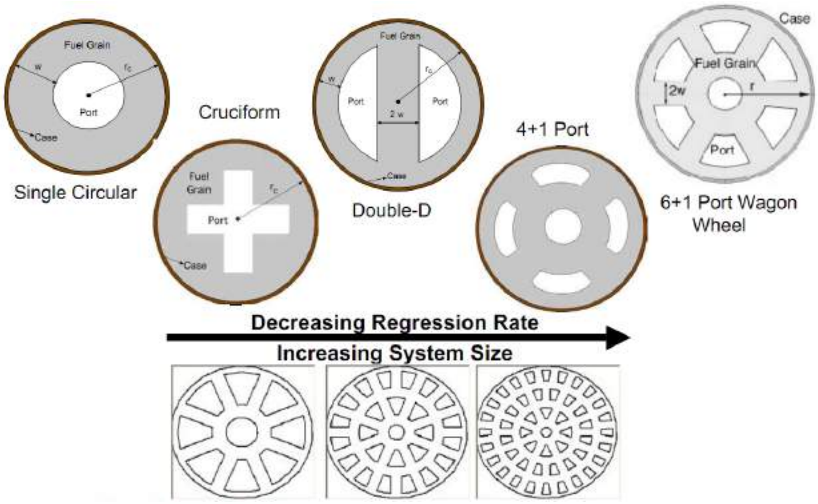

Figure 1.3: Example of multiport grain configurations

- *Packaging issues*: in a liquid rocket the large part of the system is composed by the storage propellant tanks. This is increased particularly for low thrust to total impulse ratios (e.g. spacecrafts). Tanks can be easily packaged choosing different configurations in terms of tanks number, shape and positions. Solid rockets are composed mainly by the combustion chamber that encloses the solid grain (plus the nozzle). Several geometrical solutions are available for solid motors allowing to fulfill multiple different mission constraints (e.g. different L/D ratios), moreover the propulsion engineer can tailor the regression rate and the grain shape for the specific needs. In a hybrid rocket the liquid oxidizer can be easily packaged as in a liquid rocket. The hybrid combustion chamber geometry is dictated by the solid fuel envelope. Due to the complex dependency of the hybrid regression rate on several parameters (like oxidizer flux), it is not possible to easily alter geometries as in solid propulsion where the mass flow is readily related with the burning area. On the contrary in a hybrid motor the fuel mass flow changes even with a constant burning area. That s why a constant burning area (e.g. star shaped) grain produces a neutral burning in a solid while it s strongly regressive in a hybrid configuration [60] (inducing also a significant O/F shift for a constant oxidizer flow). For this reason, for hybrid rockets a star shaped grain is not an attractive option to increase the burning area and the volume loading as it is for solid ones. Usually hybrid combustion chambers tend to be slender. Often it is stated that this is related to the low regression rate and should not be a problem for low-thrust/longduration applications. However, this is not completely correct. Considering a classical design (single or multiport), even with a complete freedom on the regression rate it is difficult to design a performing system exceeding a certain ratio between the initial and final oxidizer flux (amount of O/F shift, max flux limited by flooding or exit Mach number, lower flux limited by chuffing etc.). This in turn fixes the ratio between the internal and external port diameter and consequently the required regression rate and L/D ratio (for a given motor O/F). Very fat hybrid motors are not likely possible for low-thrust/long burning time systems. An exception could be other alternative configurations like the vortex pancake which however bring its own problematics. Another important aspect compared to liquid rockets is that it is not possible to design a propulsion unit that can be used on different spacecrafts with different total impulse requirements because, again, the combustion chamber contains the solid fuel. On the contrary a liquid motor can be combined with different tanks to deliver different total impulses.

- *Combustion efficiency*: as previously said, a hybrid system tends to produce a rougher and less complete combustion compared to solid and liquid ones, causing a larger penalty compared to theoretical values.
- *O/F shift*: the impossibility to maintain the motor O/F ratio fixed at the optimal value leads to a decrease of the average specific impulse. Careful design can reduce these losses to less than 1%.
- *Slower transients*: ignition transients are generally slower for hybrid systems. The response to throttling is slower too. The combustion chamber of a hybrid is much bigger than an equivalent liquid because it must contain the solid fuels, moreover the chamber volume changes with time reaching its maximum value at the end of burning when the grain is consumed. Also, the thermal lag in the solid fuel changes with time and reaches its maximum towards the end. This prevents hybrid systems to be used when very accurate, repeatable, fast response is necessary (in which case hypergolic liquid monobipropellant operating in multi-pulse mode is preferred), but in general it should be no major issue.

The fact that, generally, theoretical hybrid figures (I_{sp} , ρI_{sp}) systems are intermediate between solid and liquid ones makes them less attractive when only few performance parameters must be maximized for a specific task. This was one of the reasons for the previously outlined discard of hybrid motors as main propulsion choice. The other fundamental aspect was the performance penalty caused mainly by the low regression rate and related negative attributes. Finally, as already mentioned, the complex coupling of motor parameters makes hybrid rockets less attractive from an ideal design point of view. Other hybrid concepts have been conceived and (to a less extent) developed/tested to overcome conventional hybrid issues, but usually the added complexity or drawbacks of these solutions make them not sufficiently (or even less) attractive.

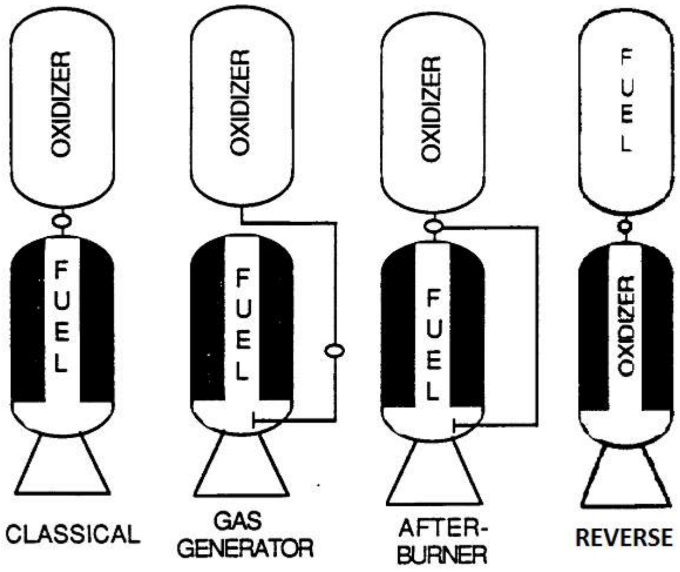

Figure 1.4: Some alternative hybrid schematics.

One aspect to underline is that all the claimed advantages of hybrid propulsion are often not achievable for the same propulsion unit due to propellant choice or system configuration (this can be also partially attributed to the other two propulsion types to a less extent). Typical examples are the LEX sounding rocket or the Firebolt presented later. Moreover, some of the solutions proposed to solve specific hybrid issues negate other hybrid advantages. A typical example is the use of small amount of oxidizer in the fuel grain to increase the regression rate. Even if this solution is safer than a conventional solid propellant grain it loses the fundamental attribute of complete grain inertness.

It is also important to remark that the comparison between hybrid and liquid systems is often ill posed; for example, the ablative cooling of hybrid rockets is claimed simpler than regenerative cooling for liquid rockets. This comparison is a bit unfair because ablative-cooled liquid rockets exist, and a hybrid rocket could be also regenerative-cooled (even if it is less attractive for hybrid systems than liquid ones). Similar examples can be done for other aspects like the pressurization system.

However, it is worth noting that some hybrid characteristics like safety and simplicity could lead indirectly to a performance advantage. For example, a safe and simple propulsion system has more chances to exploit the advantages of air launch. Moreover, a simpler, safer, cheaper system can be tested much more times in a smaller timeframe. This in turn allows the possibility to continuously upgrade, optimize and improve the system with new state of art technology, for example in materials science. This fact is especially significant during a period of low investments like the current one.

An analysis of the technology used nowadays on launchers and spacecrafts shows that the state of the art for space systems is often far from being the real state of the art of the same technology. The reason for that is the following: the tremendously high costs of space (and the impossibility of repairing the failures) impose the need for a very high reliability. High reliability drives up costs that in turn increase the demand for high reliability. This phenomenon is called the space spiral. The required high reliability in a period of limited budgets induces a very conservative approach; a typical example is the fact that a common PC has more capability than the computers used in the ISS. Any improvement is introduced to operational level very slowly. This behavior has prevented the real birth of a large private autonomous space business limiting the great part of the activities to a relatively small number of governmental funded projects.

Figure 1.5: The Space Spiral, how it is now (left) and how it should be (right).

Without the actual governmental support the space business would collapse (unlike the aviation segment for example). A dramatic reduction of the cost of space is deemed necessary to reverse the space spiral. A decrease of space costs coupled with less fragile and more flexible systems permits a lower demand of reliability that in turn requires less cost allowing an increased number of missions. More missions could guarantee a real sustainable business. It is hoped that hybrid propulsion could be one element (but for sure not the only one) that could help to reverse the space spiral. This could be possible only if hybrid systems could afford a significant cost reduction, not being simply on the level of current liquid and solid ones. At the same time the exponential form of Tsiolkovsky equation allows only limited losses of performances. A larger penalty translates indirectly on high costs because of large size increase (these aspects have been highlighted by Grosse). To achieve this ambitious object classical hybrid issues must be fixed preserving its inherent advantages like safety and simplicity, guarantying high reliability and very low costs.

1.3 Hybrid Propulsion History

The early history of hybrid rocket development dates back to the '30s, the decade when the bases of modern experimental rocketry have been set. The first often claimed hybrid rocket (however sometimes referred as a liquid) is the GIRD 09 developed by a Soviet group of scientists (such as Korolev, the father of Soyuz family) and launched (only partially successfully) in 1933. It used liquid oxygen fed by its own pressure with gelled gasoline supported on a metal mesh.[2]

Afterwards other experiments were made by a few researchers using carbon as a fuel. They found a very low regression rate caused by the very high heat of ablation of carbon (in fact carbon-based material are often used as ablative protections). Further work was done during the '40-'50 at the Pacific Rocket Society, General Electric and Jet Propulsion Laboratory. These preliminary activities demonstrated the basic characteristics of hybrid rockets like low regression rate, insensitivity to crack, regression rate dependency on oxidizer flow and consequently the possibility to modulate the thrust varying the oxidizer flow.

In the '60s huge investments deriving from the Sputnik launch first and the race to the moon later, brought great improvements in rocket propulsion. A great boost in hybrid rocket activity occurred as well, even if on a smaller scale compared to solid and liquid systems. A wide variety of fuels and htb

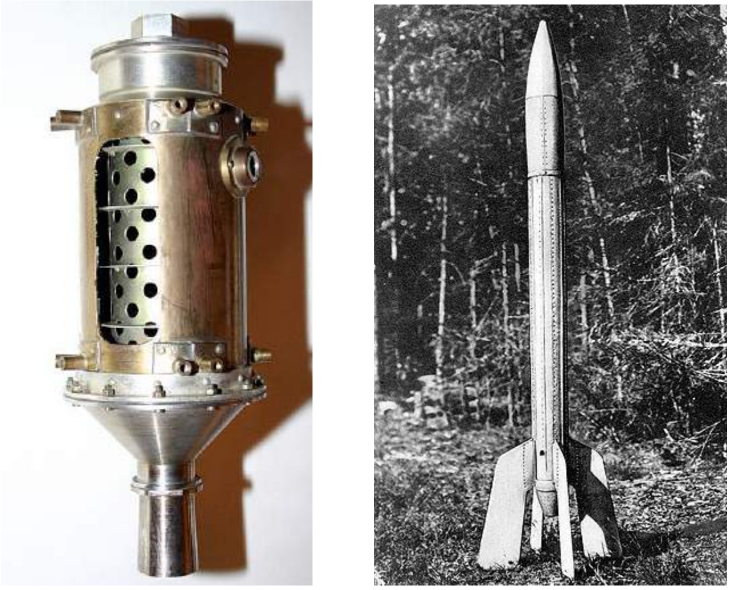

(a) Combustion chamber (b) Complete rocket

Figure 1.6: GRID 09 combustion chamber and rocket.

oxidizers were tested in different conditions defining the basis of hybrid rocket motor behavior.

The main finding was that hybrid regression rate data correlates well with the expression:

$$\dot{r} = aG_0^n L^m \tag{1.1}$$

Where G_0 is the oxidizer flux, L is the length, a , n and m are coefficient determined empirically. Using the previous equation, motor design studies were conducted and equations were developed to determine stoichiometric length and to predict thrust and O/F shift with time.

In 1967 there was the first attempt to scale up hybrid technology with the test of a large motor (180 kN) using the multiport configuration. This solution was conceived to compensate for the low regression rate. The wagon-wheel grain design paved the way to the larger works made two decades later.

In the mid-1960s NASA sponsored a series of study about high-energy combination for space engines. A large eleven port motor (1.07 m diameter) was tested using 70% FLOX (70% fluorine, 30% oxygen) as oxidizer and a mixture of lithium and lithium hydride incorporated on a HTPB binder.

The ignition was hypergolic and the combustion was smooth. Probably the high reactivity of the propellants helped the vaporization and burning of the incoming oxidizer. Another approach called tribrid was conceived. The motor should have burned liquid hydrogen, liquid oxygen and beryllium powder placed in a solid matrix (HTPB). The principle was to burn the beryllium with the oxygen to produce a large amount of heat used to accelerate a low molecular weight fluid (the hydrogen). oth programs were cancelled because of the very dangerous characteristics of the propellants used.

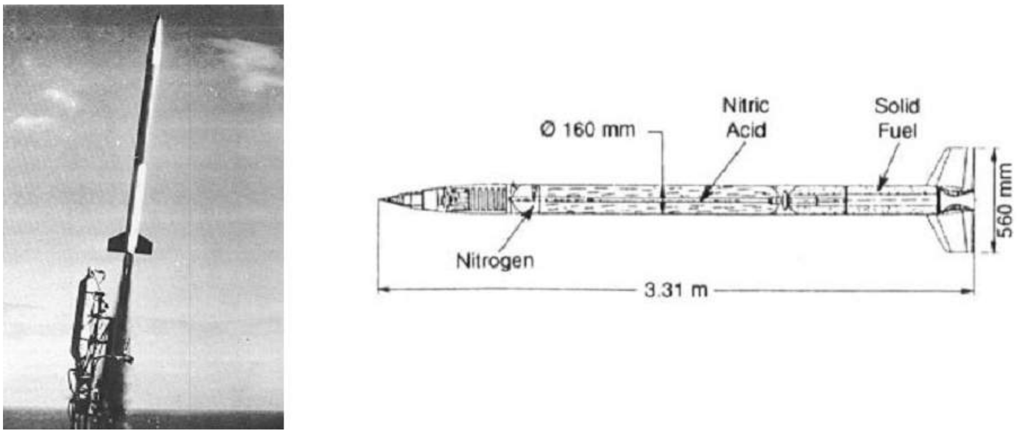

Figure 1.7: LEX sounding rocket

In Europe two important activities were performed, culminating with successful ground and flight tests of hybrid sounding rockets. One was done in France by ONERA, that developed the Lithergol Experimental (LEX).The second was in Sweden by Flygmotor, which developed fuels called Tagaform and Sagaform and planned, but never launched two large sounding rocket. Both programs were abandoned in the '70.

It is worth to remark that the LEX sounding rocket was one of the highest performing hybrid rockets ever developed, achieving very high combustion efficiency and propellant mass.

A peculiar series of programs about hybrid target drones covered three decades from the '60s to the '80s. In the mid-1960s UTC and Beech Aircraft began to work on the Sandpiper and later another program called High Altitude Supersonic Target (HAST) followed. This work later became the Firebolt target missile system produced by Teledyne Ryan Aircraft (with

CSD as the motor manufacturer). It is worth noting (and an ironic paradox) that both LEX and Firebolt were discarded not for their (excellent) performances but for reasons of cost and complexity. This is in contrast with the common view that hybrid rocket motors are cheap, but poorly performing.

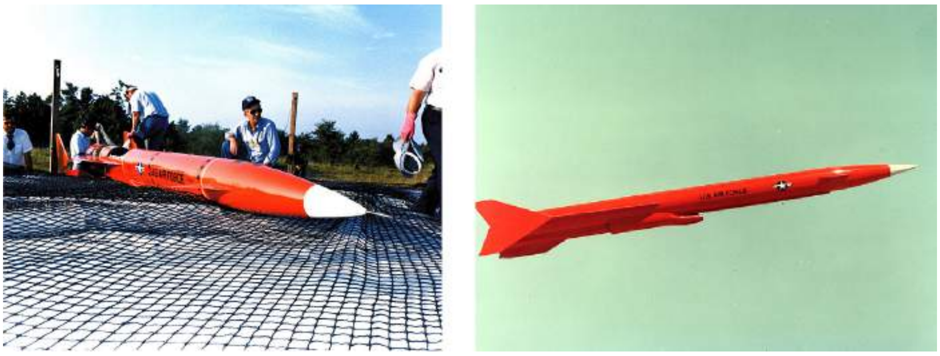

Figure 1.8: Teledyne Ryan AQM-81 Firebolt Drone

After a decade of stagnation there was a revival of the interest in hybrid propulsion in the '80s. The growth of the commercial satellite market and the increased international competition prompted the search for a low-cost access to space. The company STARSTUCK was created to develop a large sounding rocket, but after an unsuccessful launch the company was reorganized and renamed AMROC (American Rocket Company) which began developing a low-cost launcher called AQUILA.The basic philosophy was to use high design margins to reduce development and production costs and to increase the reliability of the system. The inert characteristics of hybrid propellants were perfectly suited for this kind of approach.

AMROC fired the largest hybrid motors ever tested up to that time. They relied on a multiport configuration to achieve the necessary burning area and had to face several stability issues. That work laid the foundation of our modern know-how on large hybrid systems. Another attempted launch failed, but it showed an important hybrid feature: the damage made by the two accidents was very limited, proving the safety and nonexplosive characteristics of hybrid systems also at large scales. Hybrid systems were seen has an interesting option because of their larger grain manufacturing tolerances, their benign failure modes and their possibility to stop the motor in flight. Several design studies were made to assess the use of hybrid motors for large

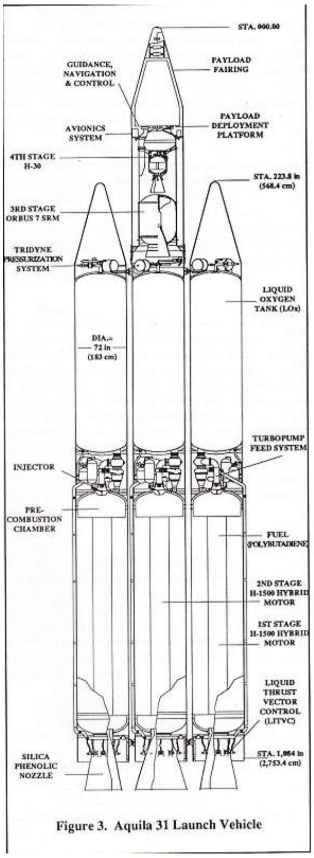

Figure 1.9: Aquila Launch Vehicle

boosters.

During the '90s hybrid research began to gain more attention also in the academic world and between small companies following the shifting from the performance dominated cold war era to a new period of increased attention for safety, cost and environmental friendliness. New (or sometimes forgotten) ideas were conceived and tested in order to improve the low regression rate of hybrid systems because it was seen (properly) as a major show-stopper for hybrid propulsion.

One of the most successful solutions proposed was the swirl or vortex injection. In this configuration the oxidizer is injected tangentially to the chamber walls in order to create a rotating flow field. This strong swirling flow inside the combustion chamber has numerous consequences which if correctly used led to an improved efficiency ad a noticeable improvement of

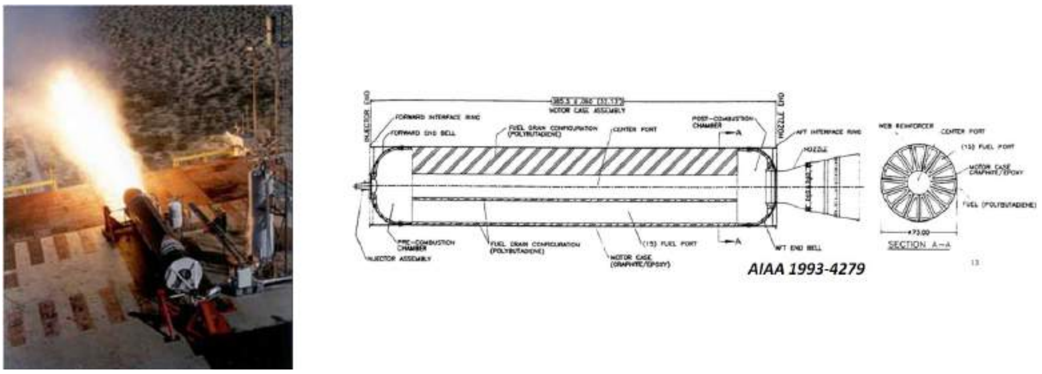

Figure 1.10: Large scale test firing of AMROC Motors.

the regression rate.

Yuasa experimented swirl injection wherein the oxidizer entered the combustion chamber at the head end as in a conventional hybrid. In the US, at Orbital Technologies Corporation (ORBITEC), Knuth experimented the double vortex hybrid wherein the swirl oxidizer was located at the aft end (opposite to Yuasa) of the fuel grain. The latter arrangement generated a pair of coaxial, corotating, bidirectional vortices achieving a very high combustion efficiency and an impressive regression rate (even 7 times the classical values).

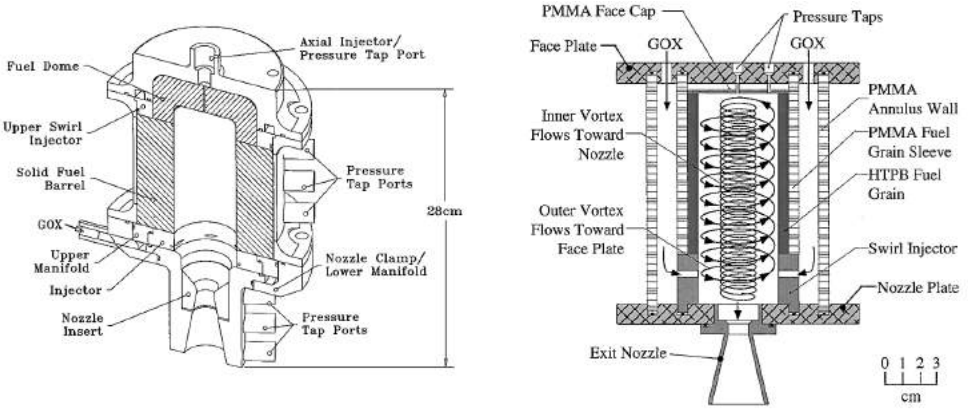

Figure 1.11: ORBITEC Vortex Rocket Engine

At the end of the decade the vortex flow pancake (VFP) concept was developed at Surrey. In this case the swirling oxidizer flow is generated between two fuel disks that end burn in opposite directions during combustion.

A very smooth combustion and high efficiency were obtained.

More recently NAMMO Raufoss applied the head end vortex injection on a H_2O_2-HTPB hybrid motor. The great advantage of this solution consists in the possibility of catalytic decomposition of prior to chamber injection. Indeed, most of the work with vortex injection has been done with the oxidizer in the gaseous phase (mainly GOX). However, in a real motor the oxidizer needs to be stored as liquid phase for performance reasons. Liquid vortex injection has received less attention and the few works are not as impressive as for gaseous injection. Alternatively, the oxidizer can be gasified prior to chamber injection, but this usually adds complexity. H_2O_2 is an exception because it can be decomposed easily using a catalyst pack. In this way the full potential of gaseous vortex injection can be exploited on an operational motor. NAMMO configuration resulted in a motor that is stable, throttleable, achieving a good efficiency and with a regression rate several times higher than a classical hybrid. Moreover, the hot products of H_2O_2 decomposition are able to ignite the solid fuel. In this way the motor can be started and stopped several times without a separate ignition device.

In 1999 Lockheed Martin started a new program called HYSR. The object of this work was the development and flight test of a large hybrid sounding rocket, advancing readiness level of this kind propulsion and showing its positive attributes. The three-year technology demonstration program was a collaborative effort between NASA and Lockheed Martin and had a total budget under 6 million dollars. In the frame of this project Lockheed Martin developed and patented two hybrid-based subsystems. The first consists in the use of small hybrid rockets fed by gaseous oxygen (GOX) to ignite the main motor and to maintain combustion stability for the entire burn. The second relates to the pressurization technique. For simplicity a pressure-fed solution was selected in order to meet the budget and time constraints. However, a special upgrade was conceived to limit volume and weight of the pressurization system.

The HYSR was finally launched from Wallops on December 2002 reaching an altitude of 42 km.

Based on the previous experience Lockheed Martin participated to the DARPA Falcon Small Launch Vehicle (SLV) program aimed to develop and

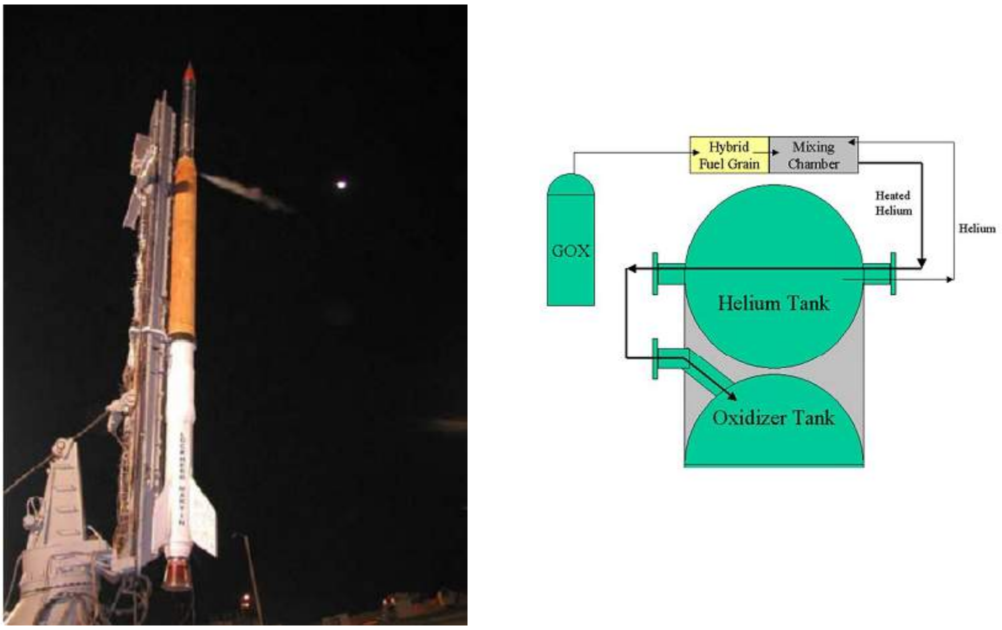

(a) HYSR Sounding Rocket

(b) LM patented heated helium pressurization system

Figure 1.12: HYSR Sounding Rocket.

demonstrate an affordable and responsive space lift capability. LM tested successfully a 3 rows/43 ports upper stage motor in 2005.

Doubtless the most famous hybrid success has been the victory of the Ansari X prize obtained by Burt Rutan's company Scaled Composites with its SpaceShipOne (SS1). The Ansari X Prize was a contest for the first commercial company to fly twice above 100 km. Scaled Composites built a two-stage airplane to win the prize. The first stage was an air-breathing plane called White Knight and was used as a carrier for the second stage plane, the already cited SS1 powered by an N_2O_2-HTPB hybrid rocket motor. Scaled Composites developed multiple unique and innovative solutions for its hybrid system. SS1 was completely built around the hybrid motor and the oxidizer tank, the latter bonded to the inside of the airframe. The tank was made with a composite fibers overwrap with an internal liner. [12]

SS1 flew successfully in 2004 reaching more than 100 km and winning the X prize. Thanks to this accomplishment hybrid propulsion began to be known outside a restricted niche of propulsion engineers. The choice of hybrid

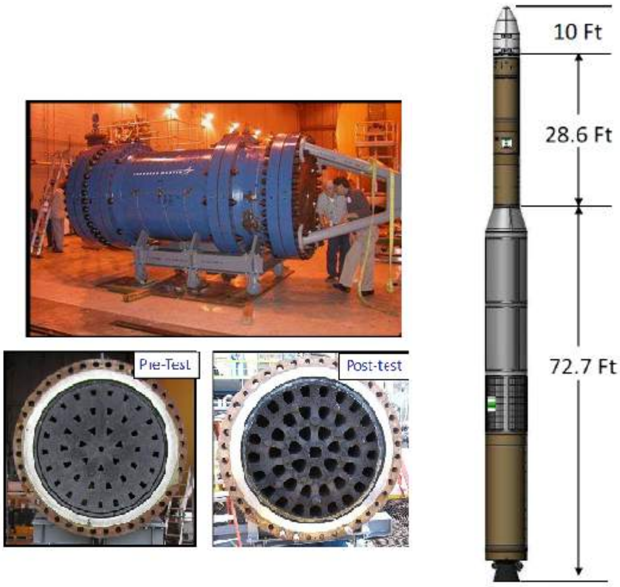

Figure 1.13: Lockeheed Martin DARPA Falcon hybrid rocket.

propulsion by Scaled Composites confirmed its positive attributes like safety, good performance, system cost, quick turnaround and thrust termination. SS1 experience could indicate a path for the successful implementation of hybrid propulsion, mainly in the extensive use of composite materials, self-pressurization and integrated design.

Today Scaled Composites together with Sierra Nevada Corporation (SNC, which acquired SpaceDev) is developing the hybrid motor for the successor of SS1, the SpaceShipTwo. This larger vehicle is able to accommodate six passengers and two pilots and would be used by Virgin Galactic for suborbital space tourism.

Another event worthy to be cited is the launch of Atea-1 sounding rocket developed by the New-Zealand company RocketLab in 2009. The rocket was composed by a first hybrid booster and a second inert dart. The rocket had an empty weight of nearly 20 kg with a lift-off weight of 60 and was designed to reach more than 100 km of altitude. Unfortunately, the second stage was not recovered so actual performances have been not verified. However, it represents a demonstration that with a proper use of composite material a hybrid rocket could reach very good values of propellant mass fraction.

On September 2018 Nammo launched the hybrid sounding rocket Nucleus

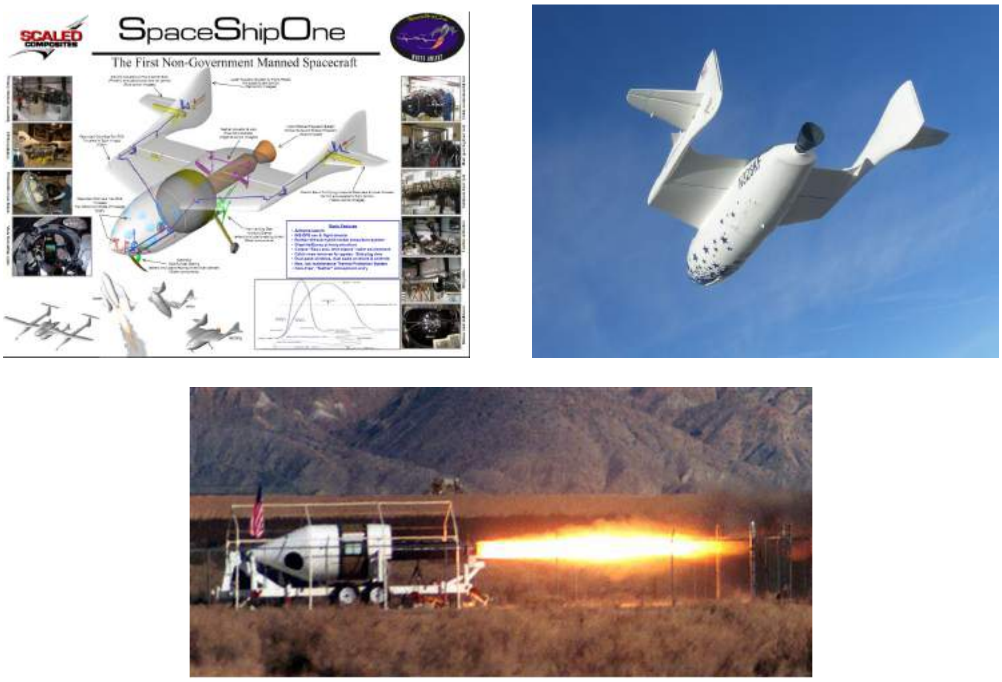

Figure 1.14: SpaceShipOne.

from Andøya Space Center in Norway. Reaching an altitude of 107,4 km, it was the first rocket powered by a Norwegian motor design to reach space and the first European hybrid rocket to do so in more than 50 years. Nucleus was powered by a 30 kN motor using as oxidizer and a solid rubber-like substance as fuel .

Figure 1.15: Nammo Nucleus hybrid rocket

1.4 Aerospace Materials

The requirements for the launch vehicles to deliver scientific or commercial payloads into a stable orbit around the Earth are complex and often greatly differ from common engineering applications.
For example, the structural materials need to sustain high forces during the phase of maximum aerodynamic pressure at the ascent, low temperatures in the liquid fuel systems, high temperatures in the combustion chamber and in the nozzle. If all of that wasn't enough, all components used need to be extremely lightweight. The reason for massive parts being unacceptable for launch vehicles is rooted in the very foundation of rocket science, the rocket equation.[3]

In 1903, Konstantin Tsiolkovsky applied the conservation of momentum, as shows in figure 1.16, to rockets and came up with his rocket equation:

$$\Delta_v = v_f - v_i = v_e \ln\left(\frac{m_i}{m_f}\right) \tag{1.2}$$

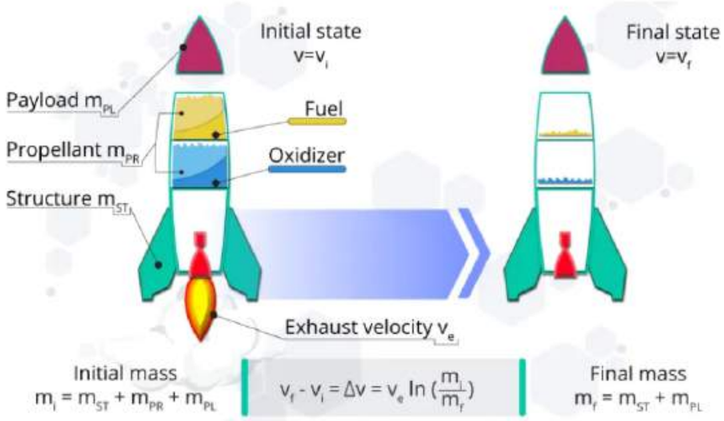

Figure 1.16: Schematic visualization of the rocket equation.

From this equation, it can be seen that the structural mass of the rocket plays a critical role. What we can achieve up to the sky, atmosphere or in the space it is strictly dependent from the Δ_v attainable. For example, the Δ_v needed to reach low earth orbit is about 8 km/s. The remaining part of the mass (m_f) is shared by the structure of the rocket and the payload, that is merely who paids for the launch. Hence, the lower the structural mass of the rocket, the higher the mass for the payload can be for a given amount of fuel.

The materials used in space are, more often than not, the most advanced materials that humans have created and we are constantly researching and creating new and improved materials. These materials need to possess a number of unique properties to be effective in space.[20]

Historically, aluminium and titanium alloy, steels and nickel superalloy were the landmark for space structures materials. The 2000 series of aluminium alloys has been deployed for structural tanks. A favourable characteristic of aluminium alloys was their increase in tensile strength at cryogenic temperatures, which makes them especially attractive for this application. In general aluminum alloys are often strong and lightweight enough to be functional in space structures and satellites. For example, aluminium is used for the shutters on the windows of the International Space Station in order to protect the windows from impacts. Besides a high strength-to-weight ratio and good formability, aluminum also has its own anticorrosion mechanism. When exposed to air, aluminum forms a hard, microscopic oxide coating which seals the metal from the environment. Aluminum matrix composites, that belong to hte metal matrix composites (MMCs) family consist of metal alloys reinforced with fibers, whiskers, particulates, or wires. Alloys of numerous metals (aluminum, titanium, magnesium and copper) have been used as matrices to date. In the NASA Space Shuttle, for example, 240 struts are made of aluminum reinforced with boron fibers. To feed the fuel from the tanks to the engine and to connect other auxiliary pressurized systems, feed lines and pipes are used. Metals for these components need to have a high ductility in order to allow for the necessary curvatures. Also, maintaining strength and ductility at cryogenic temperatures and the chemical compatibility with the conducted fluid are important. The corrosion resistant 321 stainless steel is a prominently used material for rocket pipes. Other suitable materials are the nickel base super alloy Inconel 718 and the stainless steel A-218, which are both deployed in the space shuttle main engine (SSME). A titanium-based alloy has proven to be the ideal material for the turbopump blades and casing.

Currently, standard aerospace aluminum – 6061, 7050, and 7075 – and traditional aerospace metals – nickel 718, titanium 6Al4V, and stainless 15-5PH – still have applications in aerospace. These metals, however, are currently ceding territory to new alloys designed to improve cost and performance. To be clear, these new metals aren't always new, some having been available for decades. Rather, they are new to practical production application, as machine tools, tooling technology, and insert coatings have sufficiently advanced to tackle difficult-to-machine alloys.[17] Titanium aluminide (TiAl) and aluminum lithium (Al-Li), for example, which have been around since the 1970s, have only been gaining traction in aerospace since the turn of the century, figure 1.17. Titanium 5553 (Ti-5553) is another metal that is reasonably new to aerospace, exhibiting high strength, light weight, and good corrosion resistance. Major structural components that need to be stronger and lighter than the previously used stainless steel alloys are perfect application points for this titanium alloy.

Figure 1.17: The use of aluminum-lithium Al 2195 in manufacturing major External Tank components allowed NASA to reduce the overall weight of the External Tank by 3402 kg

In addition to these new metal alloys, in the last 40 years, composite materials have seen their use increase, like Kevlar and Carbon fibers reinforced plastic (CFRP). In the early days of composites, glass fibers were used

to strengthen a matrix of epoxy resin. This glass reinforced plastic (GRP) found limited use in aerospace applications because of its low stiffness. In the 1960s, new fiber reinforcements were introduced, including Kevlar, an aramid with the strength of glass fibers but stiffer. In the NASA Space Shuttle program, one of the largest aerospace composite applications at the time took place.[4] All five Orbiter vehicles used graphite/epoxy doors, figure 1.18, and performance was excellent throughout all flights. Not only was the expected weight saving achieved and thermal-structural stability was acceptable, NASA later discovered that the graphite/epoxy material showed an advantage in ease of repair.
Today, carbon fibers are the reinforcement of choice for aerospace composites.

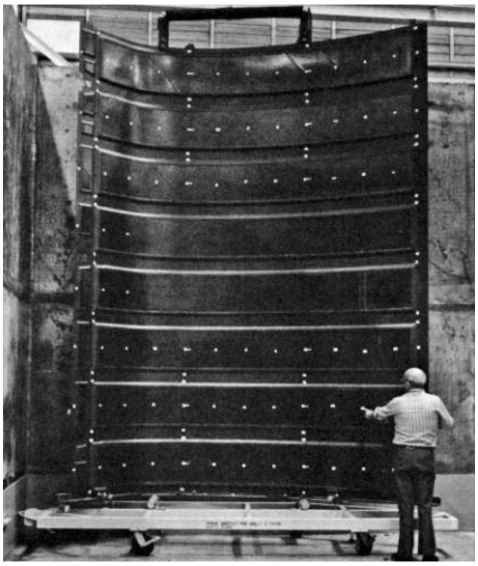

Figure 1.18: Orbiter payload bay door made using graphite-epoxy frame-stiffened thin sandwich. In place of the baselined aluminum structure it provided significant weight savings of about 408 kg

The important design properties of carbon composites are their high strength-to-weight and stiffness-to-weight ratios. With proper selection and orientation of fibers, composites can be stronger and stiffer than steel parts with similar thicknesses but 40 to 70% less weight. Fatigue resistance and chemical resistance of continuous-fiber composites are excellent. Like most rigid materials, however, carbon composites are relatively brittle. They have no yield behavior and resistance to impact is low.[5]

Also important, composite fibers are easy to be formed into complex shapes that, for metallic parts, would require machining and create joints. So composite components aren't just lightweight and stiff, they reduce the number of heavy fasteners and joints, which are also potential failure points. In doing so, composite materials are helping to drive an industry-wide trend of fewer components in overall assemblies, using one-piece designs wherever possible.

Figure 1.19: Space Shuttle, a state-of-art of the engine technology, SSME are the successful liquid propellant rocket engine to date.

1.4.1 Composite Materials

> "As the term indicates, 'composite material' reveals a material that is different from common heterogeneous materials. Currently 'composite materials' refers to materials having strong fibers – continuous or noncontinuous – surrounded by a weaker matrix material."[D. Gay, S. V. Hoa, S. W. Tsai]

As said in the latter paragraph, a composite material consisting, for example, of epoxy resin and carbon fibers, represent the union of the lightness of the matrix with the high characteristics of strength and stiffness of the reinforcement, this allows reaching very high specific mechanical properties.

The composite materials are, therefore, made up of several different materials in solid form which, together, perform multiple structural functions.[7]

The constituent phases of these materials can be divided into two categories: the continuous phase is called 'matrix' while the dispersed phase is called 'reinforcement'. Generally, for structural uses, the dispersed phase varies on average around 50-70% of the total volume. The most used reinforcement for structural components, due to higher performance, is in fibrous form, but there are also particulate reinforcements.

This multi-phase feature brings two great advantages:

1. the union of the phases allows obtaining physical and chemical properties superior to those of the single constituents. This allows to exploit and improve the qualities of the materials used and, at the same time, to mitigate the defects.

2. the properties of composite materials can be designed simultaneously with the structural aspects. Starting from the functional requirements of the piece to be designed, the material is defined by choosing the matrix, the reinforcement and its layout according to the loads and the production technologies.

The orientation of the reinforcement, for example, allows the optimization of the mechanical properties along one or more specific directions.

Each of the phases performs a specific task: the matrix keeps the fibers separate, protects them from external attacks and transfers the loads applied to the reinforcement and the reinforcement, in turn, supports the load providing adequate strength and stiffness.

Consequently, the characteristics of these materials depend considerably on the type of reinforcement-matrix coupling chosen during the design, and in particular on:

- Volume fraction of the single phases
- Phases material type
- Reinforcement's form and type

- Production technologies

The materials to be used for the fibers are chosen based on the applications, as said, for aerospace ones, carbon, boron, alumina and silicon carbide fibers are used.

Even the structure of the material itself can vary according to needs. Laminates are materials formed by multiple layers of composite plies that can be oriented differently from one another in order to optimize the mechanical behavior in one or more defined directions. Sandwich panels, on the other hand, allow for good stiffness (due to greater thickness) with low weight (between the two layers of composite material, honeycombs are interposed, for example).

Given the multiple possibilities of composition and architecture of these materials, they are anisotropic and locally also inhomogeneous, so their mechanical behavior is quite complex.

1.4.2 CFRP

CFRPs are composite materials consisting of a polymeric matrix and a carbon fiber reinforcement. This type of material is spreading very rapidly in all applications thanks thanks to its high specific mechanical properties.[7]

These fibers are obtained from a polymeric precursor (the most widespread is PAN - Polyacrylonitrile, but there are also rayon and pitch) subjected to controlled oxidation, carbonization or graphitization processes, based on the desired mechanical characteristics. The fibers obtained by carbonization, in fact, have high mechanical strength but lower modules than those obtained by graphitization. Hence the difference between high strength and high modulus carbon fibers.

As an example the following table is shown, which shows the mechanical and physical properties of different types of carbon fiber:

A possible classification based on the value of the elastic modulus longitudinal is the following:

- Standard modulus, < 250 GPa
- Intermediate modulus, $250 - 350$ GPa

		T300	T1000GB	M55J	M30SC
Tensile strength	Mpa	3530	6370	4020	5490
Young's modulus E	Gpa	230	294	540	294
Maximum elongation	%	1,5	2,2	0,8	1,9
Density ρ	$\frac{g}{cm^3}$	1,76	1,8	1,91	1,73

Table 1.1: Example of properties of different types of carbon fiber Toray Industries Inc.

- High modulus, $350 - 500$ GPa
- Ultra high modulus, > 500 GPa

The polymeric matrix is generally of the thermosetting type, that facilitate the production (the low viscosity of the constituents in the curing phase allows a good wettability of the fibers).

The thermosetting resins have an elastic-fragile behavior practically independent of the temperature, until the degradation threshold is reached. Therefore they don't melt and can no longer be modified once the curing has taken place. However, they have low density, so high resistance values and specific modules. Among the thermosetting resins, the most used matrix for structural purposes are epoxy resins, thanks to better mechanical properties, good adhesion to fibers and low contraction during the reticulation process.

The production technology of composite materials is chosen keeping in mind the shape and dimensions of the final component and the required mechanical properties, in order to minimize the presence of defects in the material (fibers not perfectly aligned, residual internal tensions, porosity, adhesion ...).

1.4.3 Laminate

Laminate is defined as a material constituted by the overlapping of several layers, or plies, of composite material. These layers can be unidirectional (if the fibers are all arranged in the same direction inside the lamina) or fabrics.[7]

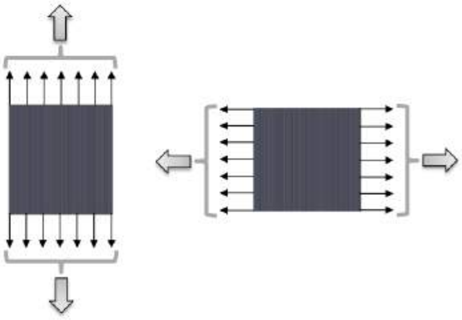

Figure 1.20: Lamina loaded respectively in the axial direction and in a direction perpendicular to the reinforcement.

The orientation of the fibers allows the optimization of the mechanical behavior along one or more specific directions.

With reference to the following figures 1.20, it is possible to identify the different behavior of a unidirectional ply subjected to a longitudinal load, ie in the direction of the fibers and transversal, perpendicular to the fibers.

From the comparison of the two figures it is clear how, in the first case, the fibers react to the load guaranteeing high resistance, in the second case instead it is the resin that sustains the load, thus providing a much lower resistance. For this reason it is of fundamental importance to know how the orientation of the stacked plies determines the resistance of the laminate, with reference to the direction of application of the load.

As an example, the graph in figure 1.21 provides the trend of the longitudinal elastic modulus of the laminate when the orientation angle varies for four different types of composite materials.

In a laminate is important to identify the sequence of the plies stacked with different orientations.

The stacking sequence is identified starting from the bottom ply. The orientation of each layer is indicated, separated from the next one by a slash'/'. If more adjacent plies have the same orientation, it is reported only once, but followed by a numeric subscript indicating the number of identical plies.

Then, if the laminate is symmetrical with respect to its middle plane (identified with the plane at half thickness of the laminate), only half of the stacking sequence is indicated in brackets, using the subscript $_s$ at the end.

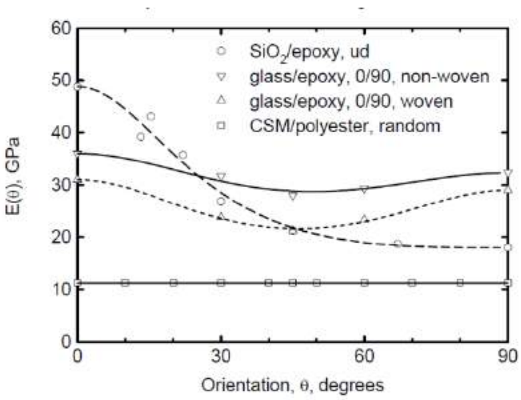

Figure 1.21: Young module vs fibers orientation for four types of GFRP.

Ply number	Orientation	Notation
1	90°	
2	0°	
3	0°	
4	90°	$[90/0_2/\overline{90}]_s$
5	0°	
6	0°	
7	90°	

Table 1.2: Example of symmetrical lay-up

Finally, if the number of layers of the laminate is odd, the orientation of the sheet lying in the middle plane is marked with an overline.

The following table shows an example of a stacking sequence that summarizes what has been described so far. It is a symmetrical laminate, composed of seven plies with orientation at 0° and 90°.

Chapter 2

Sounding Rocket overview

The sounding rocket has been designed by a team of students and employees of *T4i - Technology for Propulsion and Innovation*, a spin-off company of the University of Padua. It is propelled by a hybrid system using hydrogen peroxide as oxidizer and a solid grain of paraffin as fuel. T4i, during his activity, has already designed, built and tested similar motors; the goal of the project is to validate the hybrid technology developed within the first launch and then improve the whole system to reach higher performance and altitudes. To do so, the rocket is expected to be launched in the first months of 2020 and reach an altitude of about 10 km. It is worth to make known that many figures and of this chapter refer to older revisions of the project. They are only for explanatory purposes and do not necessarily represent the final design. Moreover, the project is still in development, therefore some configurations here described could be susceptible to change in future revisions.

2.1 General Requirements

The general functional requirements of the rocket are:

- Thrust of 5 kN;
- Burning time of 20-30 s;

- H_2O_2 decomposed in a catalytic reactor and then injected into a single port, cylindrical grain of paraffin. Hot, decomposed gas must start the ignition, no igniter is required;
- Pressure-fed pressurization system using N_2 as pressurizer;
- External body, nosecone and fins made of carbon fiber reinforced epoxy composite;
- Oxidizer tank integrated with the external cylindrical body and without liner;
- Length not exceeding 6 m and diameter of about 180-200 mm;
- Recovery system with parachutes and inflatable float to retrieve the rocket after the mission.

The design process of the rocket has been divided into 5 main subsystems. Design efforts have been focused onto structures, motor, recovery and fluidic line subsystems. The subsystems and their respective branches of competence are listed below:

- Structures
  - Cylindrical cases
  - Nosecone
  - Fins
  - Junctions
  - Components assembly
- Propulsive system, which has been divided into two subsystems:
  - ⋆ Motor
    - Catalytic reactor
    - Grain
    - Nozzle
    - Thermal protections

    - ⋆ Fulidic line
        - Pressurizer tank
        - Oxidizer tank
        - Feeding pipes and valves

- Recovery system
    - Parachutes
    - Float
    - Controls and actuators
- Payload
    - Avionics and Telemetry
    - Diagnostics
    - Control

2.2 Structures

The structures are the first subsystem to be described because they comprised the external shape and dimensions of the rocket, giving an idea of the general layout of the rocket as a whole.

Aerodynamic and trajectory studies are the basis for shape design choices, especially for nosecone and fins. The rocket has a total length of 5.450 m and an estimated dry mass of about 75 kg. When the pressurizer and oxidizer tanks are filled, it should reach a mass of about 135 kg. The main body is a cylinder with an external diameter of 195.82 mm and a total length of approximately 4.5 m. It is made up of 4 cylinders of carbon fiber reinforced epoxy composite, with Ergal-made junctions. The composite is a 11 layers laminate with a total thickness of 2.91 mm. The layers are a mix of woven (using T300 fibers), unidirectional and biaxial (both using T700 fibers) plies. Each cylinder covers a different section of the rocket (see Figure 2.1); starting from the nosecone junction, the 4 sections are:

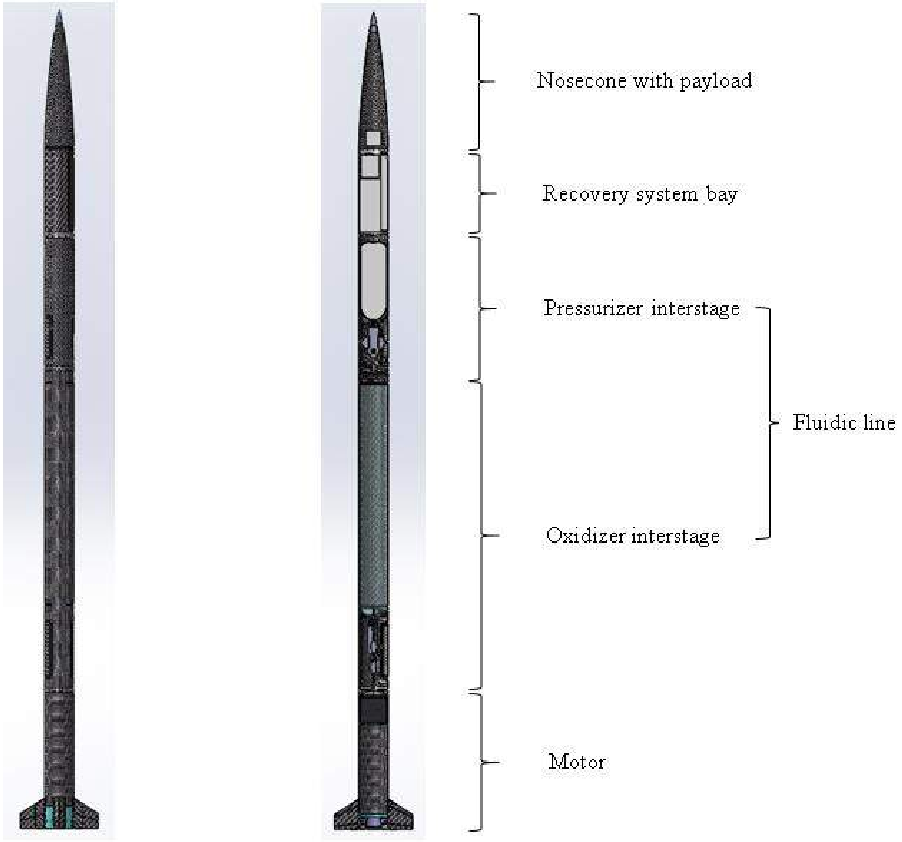

Figure 2.1: CAD of the Sounding Rocket with subsystems.

- Recovery system: 565 mm long. It has a 150×528 mm door to allow parachutes and float to operate (for more details see section 2.5).

Figure 2.2: Recovery System

- Gas line interstage (pressurizing tank and fluidic line down to H_2O_2 tank): 910 mm long. It has 2 openings (90° wide and 285 mm long) in order to allow access to the fluidic line.

Figure 2.3: Gas line Interstage

- Liquid line interstage (H_2O_2 tank and fluidic line down to catalytic reactor): 2100 mm long. The external cylindrical case functions as wall of the oxidizer tank. There are 2 openings (90° wide and 380 mm long) in the lower part to allow access to the fluidic line.

Figure 2.4: Liquid line Interstage

- Motor (catalytic reactor, combustion chamber with paraffin grain, post-chamber and nozzle): 920 mm long. The lower end is made up by a 148.7 mm long Ergal insert in order to fix the nozzle case without using fasteners on the composite.

Figure 2.5: Motor

The nosecone has a Von Karman profile and is almost 917 mm long. It is made of carbon fiber reinforced epoxy, with a tip insert of aluminum in order to withstand a maximum temperature of 300 °C. The insert is 134.3 mm long, of which 84.5 mm are exposed while 50.2 mm are inside the composite structure and serve for the bonding. The whole nosecone is designed to be easily removed or mounted in order to allow access to the recovery system before launch.

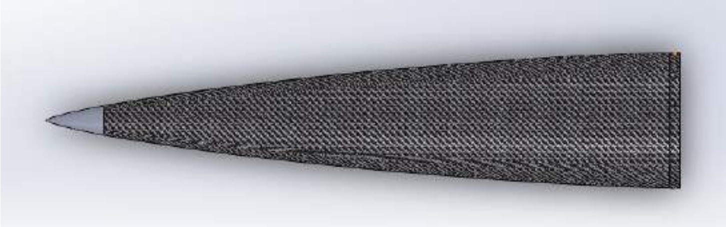

Figure 2.6: Nosecone

The fins have a symmetrical diamond profile. Each fin has a 160 mm span from tip to root. Root chord is 200 mm long, while tip chord is 100 mm long. Sweep back angle of the trailing edge is 0°, therefore the sweepback angle of the leading edge must be 57.99°. Maximum thickness, which is obviously at the mean chord, is 6 mm. The fins are made of composite material constituted by various laminas of T700 unidirectional carbon fiber and T300 woven carbon fiber, with a core made of Rohacell foam to increase the flexural modulus without significant weight increase. The 4 fins are bonded symmetrically around the nozzle-end of the rocket by means of epoxy adhesive.

Figure 2.7: Fin and attachment to rocket

2.3 Motor

The motor is the subsystem producing the thrust to propel the rocket. This subsystem is divided into:

- Catalytic reactor: it is a metal case containing disks of catalytic material which decompose H_2O_2 into gaseous O_2 and water vapor. The hydrogen peroxide is decomposed by the catalytic material contained in the case;
- Combustion chamber: it contains the paraffin grain, which burns reacting with the O_2 coming from the reactor. After that a post-chamber allows a more complete combustion of the products before the expulsion through the nozzle;
- Nozzle: it has a convergent-divergent layout in order to accelerate the exhaust gas to supersonic speed.

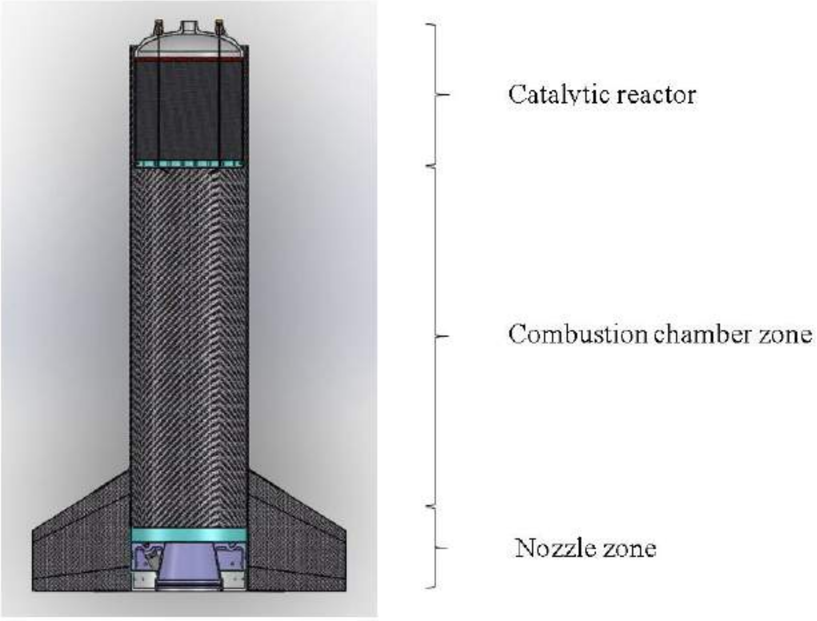

Figure 2.8: Schematic cross section of the motor with its subsystems.

The combustion chamber contains a cylindrical paraffin grain with a single port. Additional HDPE (high-density polyethylene) thermal protections are placed at both ends of the grain. A cylindrical HDPE jacket encloses most of the motor, from the catalytic reactor to the nozzle, to protect the composite case from heat. The pressure in the chamber reaches about 25 bar. The post-chamber is divided into two sections by a mixer made of cotton-phenolic. It ensures a better mixing of the exhaust gasses.

The nozzle zone is made up of a titanium alloy (Ti-6Al-4V) case, cotton-phenolic protections and a graphite insert at the throat to reduce erosion. Pressure in the post chamber is measured by two pressure sensors ifm PT5401 fastened into the titanium case.

2.4 Recovery System

The recovery system allows the rocket to be retrieved after the mission. It consists in a main parachute, a drogue parachute and a floating system kept inside a bay right below the nosecone. A door keeps the system closed and opens at the appropriate moment to allow the aforementioned devices to operate.

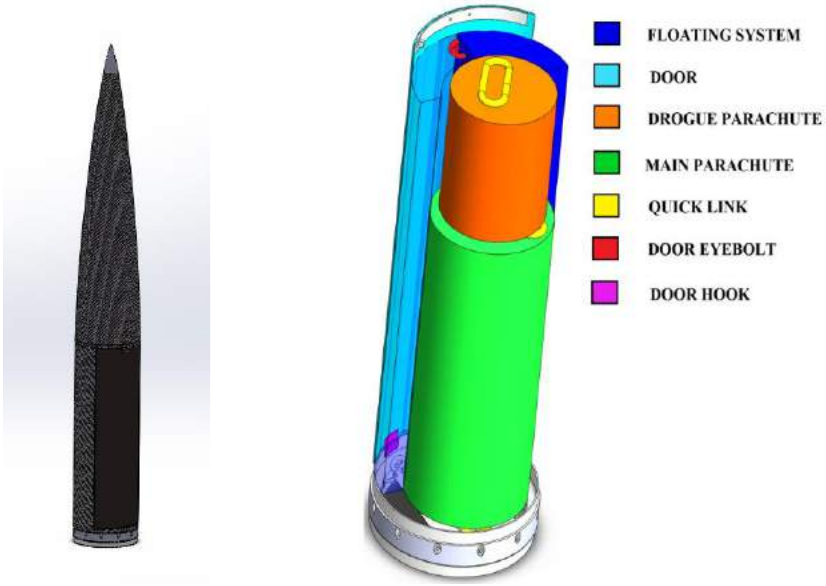

(a) Outside (b) Inside

Figure 2.9: Views of recovery bay and nosecone.

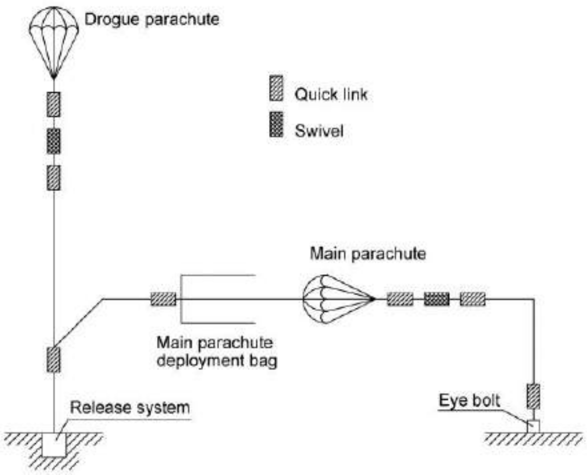

Figure 2.10: Deployment recovery system schematic.

The system activates when the rockets reaches the apogee. The rocket is supposed to land on water. The modes of operation of the system are explained schematically as follows:

- The recovery bay is closed.
- The cutter-spring system allows the opening of the door which is directly linked to the drogue parachute with a shock cord.
- Once the door is removed, the floats, directly linked to the bay with a shock cord, are the first components to come out. At the same time the door pulls out the drogue parachute, which is also linked to the main parachute and the bay with a 3 loops shock cord. The opening of the secondary parachute allows the first deceleration during the free fall of the rocket.
- At about 1 km or 2 from the ground the drogue parachute breaks away from the bay pulling out the main parachute. During the last stage of the descent the main parachute is supposed to support the whole structure and slow the rocket down until the water landing. The floats, extracted at the apogee, inflate once in contact with the water, ensuring the buoyancy.

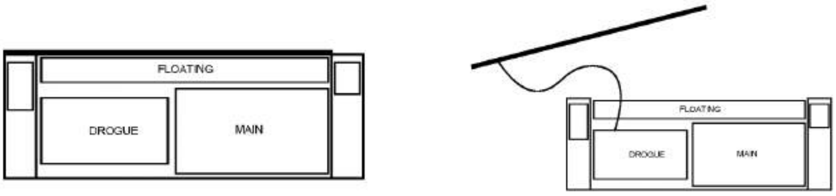

(a) Closed recovery bay

(b) Opening of the door

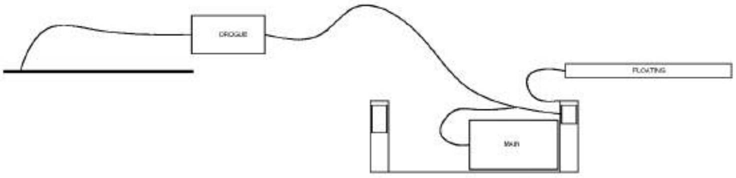

(c) Extraction of the components

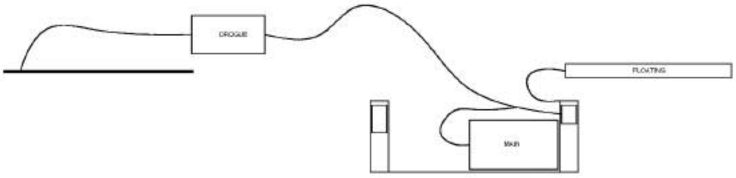

(d) Complete extraction of the components

Figure 2.11: Schematic cross section of the recovery system deployment.

2.5 Fluidic System

This report covers the whole design process developed to reach in a global configuration, that can satisfy all the requirements set at the beginning. We can divide them into two groups, the performance, and the safety ones. The requirements needed to carry out the mission, with the desired rocket trajectory, are listed in the following table.

Parallel to them, there are safety requirements. During the pre-launch phase, the take-off and the final operating phase it's important to avoid any failure of the system, alias, the reliability is essential. Moreover, the last but the most central aspect: all the processes, starting from the rocket's assembly to the day launch, involve human interventions. That means is mandatory to ensure security every time these operations happen. For these reasons, the designed fluidic line includes:

Oxidizer mass flow	$\dot{m}[\frac{kg}{s}]$	2
Oxidizer mass flow variation	$\frac{\Delta\dot{m}}{\dot{m}}$	10%
Burning time	$T_b[s]$	20-30
Minimum combustion chamber pressure	p_{cc} [bar]	20
Ullage of oxidizer tank	V_{ull}	$5-10\%$
Internal diameter	Φ_{in} [mm]	190
Oxidizer type	90% H_2O_2	
Pressurization system type	Pressure-feed	

Table 2.1: Fluidic subsystem requirements.

- By-pass line, to avoid a failure caused by the water hammer phenomenon;
- A non-reclosing passive pressure relief safety device, in case of unexpected H_2O_2 dissociation, to let the tank pressure drop off without any human intervention or detection;
- A pressure relief valve, to discharge the pressurization gas with no human intervention.
- A redundant manual valve, after each main actuated valve, to permit to operate on the rocket in safety conditions during the pre-launch phase.

All these considerations led to the baseline configuration.

2.5.1 Baseline configuration

In this section, the Visio diagram is shown. It is designed to meet all the requirements, beginning from the pressure-feed system. As we can see in figure 2.12 the first part of the line is a small gas tank, it will keep the required pressure in the oxidizer tank for the whole rocket firing phase. The line cane be divided in two main groups: the gas pressurization line, from the gas tank to the oxidizer tank, and the liquid line, from the oxidizer tank to the main engine.

Then the gas pressurization line it consists in a:

- Fill and drain valve, to charge and discharge the gas tank;

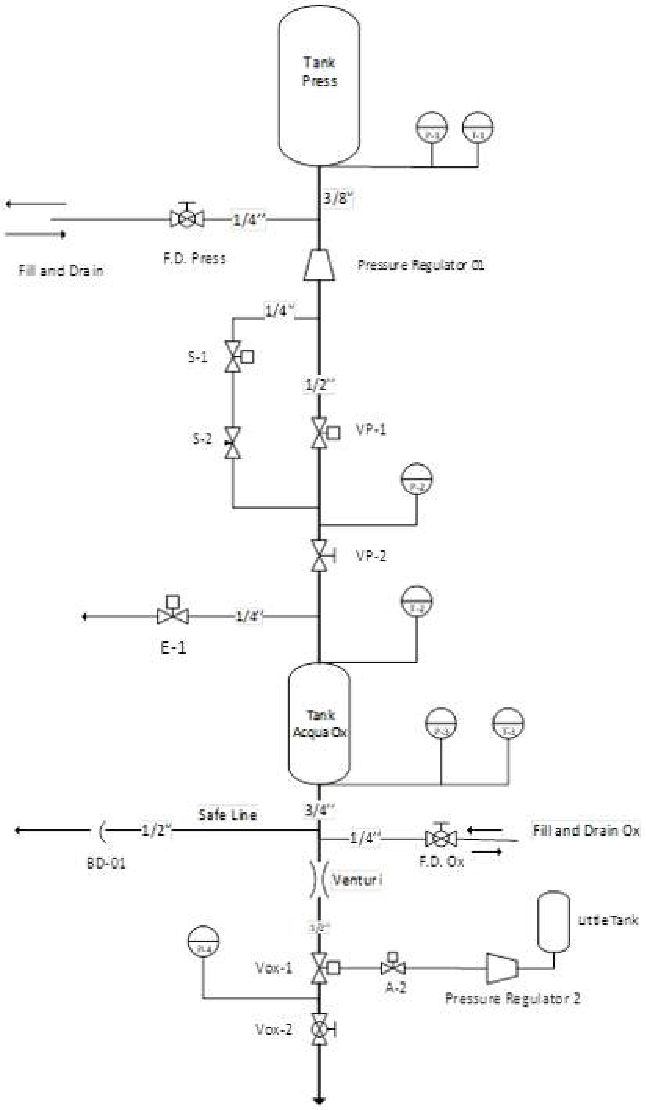

Figure 2.12: Process flow diagram of the entire fluidic line.

- The main line with the double valves, one electo actuated and the other one manual.
- The by-pass line that will initially pressurize the oxidizer tank;
- A solenoid valve on the top of the oxidizer tank as a venting device.

Then, the oxidizer tank takes place where, at the outlet, the liquid line starts, consisting in:

- Fill and drain valve, to charge and discharge the H_2O_2;
- A burst disc as a safety passive device, that will brake in case of a high pressure due to a fast unexpected oxidizer dissociation;
- The main line with double valves, one actuated wih a pneumatic actuators and the second one manual;
- The Venturi channel to uncouple the pressure in the flows.

Along the whole line some temperature and pressure sensors are positioned to keep the evolution of the system under control.

2.5.2 Main Procedures and Emergency Procedures

In figure 2.14 are listed all the main procedures that will be necessary at the launch day, to carry out a safe pre-launch phase up to takeoff. Moreover, in case of failures, it refers to which emergency procedure must be done. The emergency procedures are listed in figure 2.13

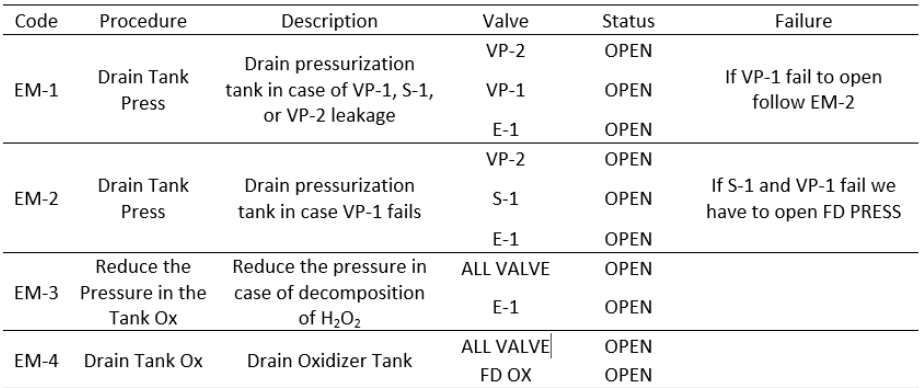

Code	Procedure	Description	Valve	Status	Failure
EM-1	Drain Tank Press	Drain pressurization tank in case of VP-1, S-1, or VP-2 leakage	VP-2	OPEN	If VP-1 fail to open follow EM-2
			VP-1	OPEN	
			E-1	OPEN	
EM-2	Drain Tank Press	Drain pressurization tank in case VP-1 fails	VP-2	OPEN	If S-1 and VP-1 fail we have to open FD PRESS
			S-1	OPEN	
			E-1	OPEN	
EM-3	Reduce the Pressure in the Tank Ox	Reduce the pressure in case of decomposition of H_2O_2	ALL VALVE	OPEN	
			E-1	OPEN	
EM-4	Drain Tank Ox	Drain Oxidizer Tank	ALL VALVE	OPEN	
			FD OX	OPEN	

Figure 2.13: Emergency procedure in case of detected failure.

2.5.3 Fluidic Line Components

The pressurizer line consists in a small tank filled with pressurizer gas (N_2) followed by a fluidic line, as represented in figure 2.15.

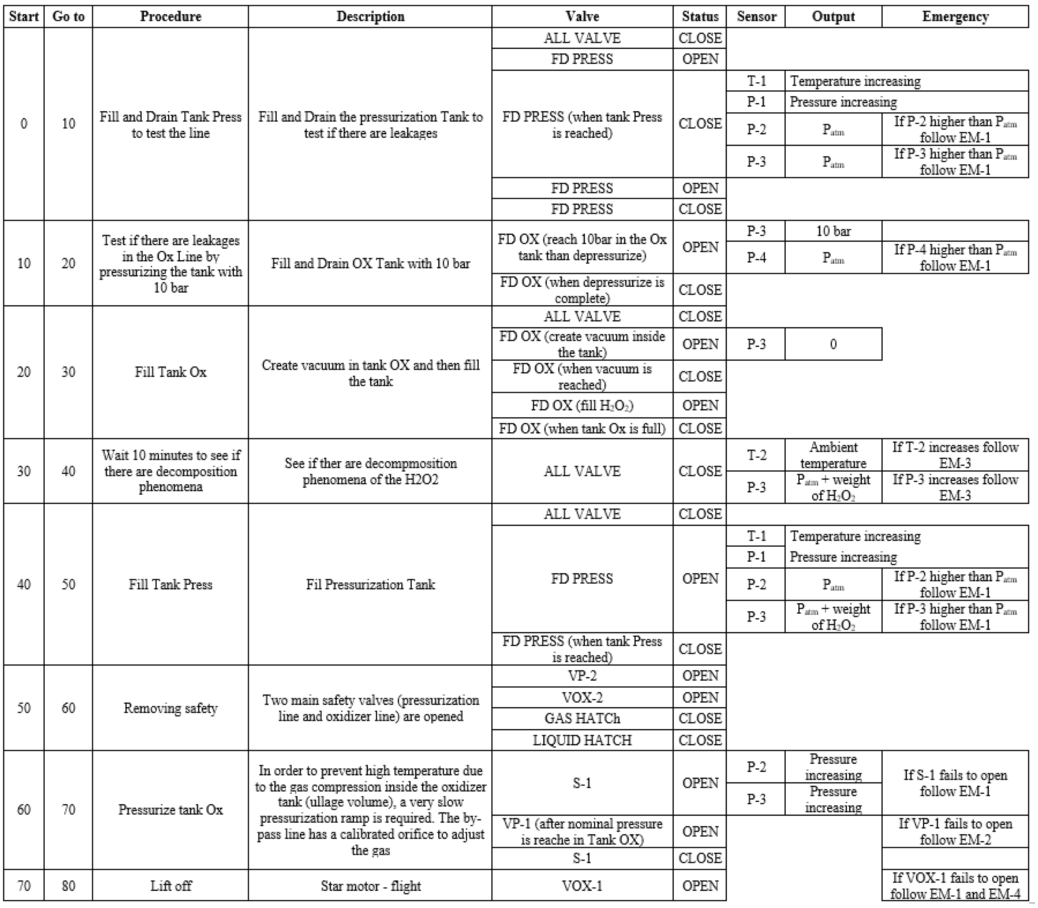

Start	Go to	Procedure	Description	Valve	Status	Sensor	Output	Emergency
0	10	Fill and Drain Tank Press to test the line	Fill and Drain the pressurization Tank to test if there are leakages	ALL VALVE	CLOSE			
				FD PRESS	OPEN			
				FD PRESS (when tank Press is reached)	CLOSE	T-1	Temperature increasing	
						P-1	Pressure increasing	
						P-2	P_{atm}	If P-2 higher than P_{atm} follow EM-1
						P-3	P_{atm}	If P-3 higher than P_{atm} follow EM-1
				FD PRESS	OPEN			
				FD PRESS	CLOSE			
10	20	Test if there are leakages in the Ox Line by pressurizing the tank with 10 bar	Fill and Drain OX Tank with 10 bar	FD OX (reach 10bar in the Ox tank than depressurize)	OPEN	P-3	10 bar	
						P-4	P_{atm}	If P-4 higher than P_{atm} follow EM-1
				FD OX (when depressurize is complete)	CLOSE			
20	30	Fill Tank Ox	Create vacuum in tank OX and then fill the tank	ALL VALVE	CLOSE			
				FD OX (create vacuum inside the tank)	OPEN	P-3	0	
				FD OX (when vacuum is reached)	CLOSE			
				FD OX (fill H_2O_2)	OPEN			
				FD OX (when tank Ox is full)	CLOSE			
30	40	Wait 10 minutes to see if there are decomposition phenomena	See if ther are decompmosition phenomena of the H2O2	ALL VALVE	CLOSE	T-2	Ambient temperature	If T-2 increases follow EM-3
						P-3	P_{atm} + weight of H_2O_2	If P-3 increases follow EM-3
40	50	Fill Tank Press	Fil Pressurization Tank	ALL VALVE	CLOSE			
				FD PRESS	OPEN	T-1	Temperature increasing	
						P-1	Pressure increasing	
						P-2	P_{atm}	If P-2 higher than P_{atm} follow EM-1
						P-3	P_{atm} + weight of H_2O_2	If P-3 higher than P_{atm} follow EM-1
				FD PRESS (when tank Press is reached)	CLOSE			
50	60	Removing safety	Two main safety valves (pressurization line and oxidizer line) are opened	VP-2	OPEN			
				VOX-2	OPEN			
				GAS HATCh	CLOSE			
				LIQUID HATCH	CLOSE			
60	70	Pressurize tank Ox	In order to prevent high temperature due to the gas compression inside the oxidizer tank (ullage volume), a very slow pressurization ramp is required. The by-pass line has a calibrated orifice to adjust the gas	S-1	OPEN	P-2	Pressure increasing	If S-1 fails to open follow EM-1
						P-3	Pressure increasing	
				VP-1 (after nominal pressure is reache in Tank OX)	OPEN			If VP-1 fails to open follow EM-2
				S-1	CLOSE			
70	80	Lift off	Star motor - flight	VOX-1	OPEN			If VOX-1 fails to open follow EM-1 and EM-4

Figure 2.14: Main Procedures during pre-launch operations.

The pressurizer tank is a CTS Ultralight, has a capacity of 9 L and can withstand pressures of up to 300 bar.

The main components of the fluidic line are:

- Manual ball valve 1/4" Ham-Let H6800 ('F.D. Press'): a mechanical ball valve that allows the passage or the total blocking of the flow. It is used to fill and drain the pressurizing line.
- Pressure regulator Tescom 44-1300 ('PR-1') : a control valve that reduces the input pressure of a fluid to a desired output value.
- Manual ball valve 1/2" Ham-Let H6800 with external actuator ('VP-1'): an electric ball valve used to open the main line and pressurize the hydrogen peroxide tank.

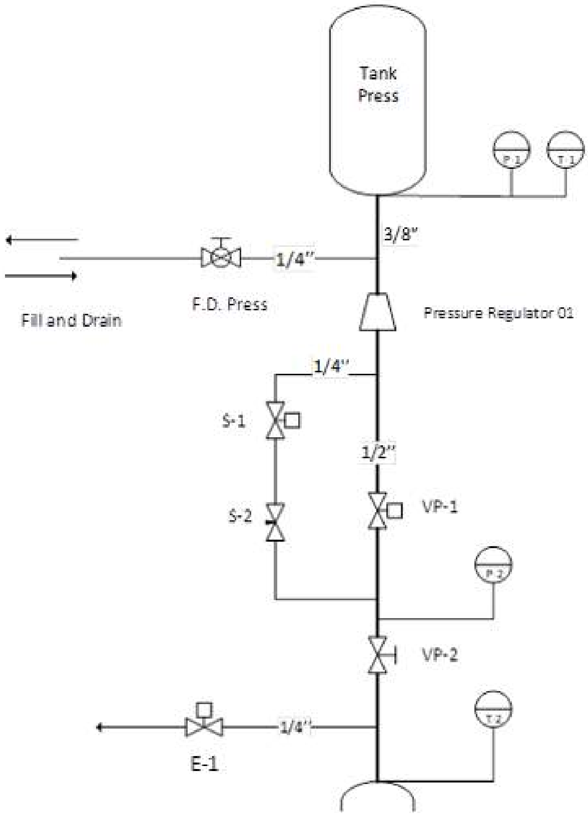

(a) Process flow diagram

(b) CAD visualization

Figure 2.15: Pressurizing line

- Solenoid valve Tameson 75 Bar ('S-1'): a solenoid valve used to open the bypass line in order to prevent high temperature due to the gas compression inside the oxidizer tank (ullage volume).

- Calibrated orifice ('S-2'): a calibrated orifice used to adjust the gas filling time to about 60 s.

- Manual ball valve 1/2" Ham-Let H6800 ('VP-2'): a mechanical ball valve that allows the passage or the total blocking of the flow. It is used as safety valve: it is opened before the pressurization and if VP-1 or S-1 fail it can stop the flow before reaching the H_2O_2 tank.
- Solenoid valve Tameson 75 bar ('E-1') : a solenoid valve that can be controlled remotely. It is used to drain the pressurizing in case of emergency.

(a) Manual ball valve Ham-Let H6800

(b) Pressure regulator Tescom 44-1300

(c) Manual ball valve Ham-Let H6800 with external actuator

(d) Solenoid valve Tameson 75 bar

Figure 2.16: Components of the gas line.[9]

The oxidizer line consists in a tank filled with 60 kg of 90% H_2O_2 followed by a fluidic line.

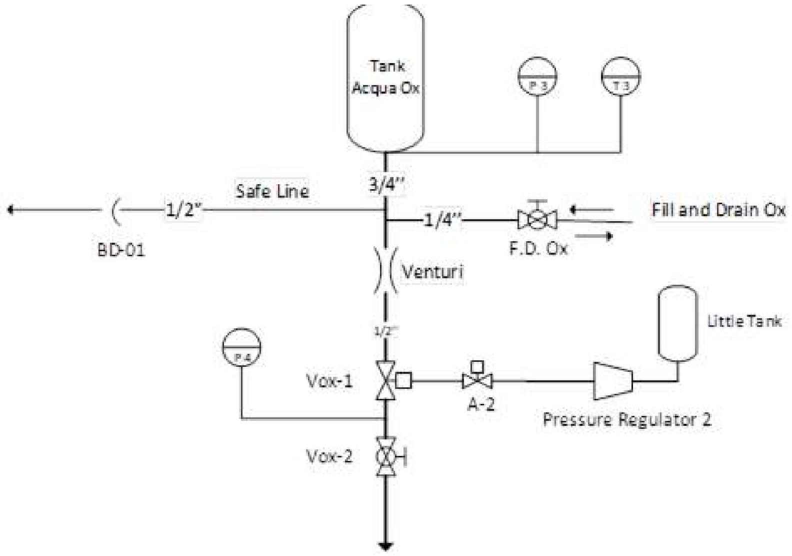

(a) CAD visualisation

(b) Process flow diagram

Figure 2.17: Liquid line

The oxidizer tank has a capacity of about 45 L, is 1636 mm long and its perimetral wall is the external composite cylinder (see section 2.1.1). The end-closures consist in carbon fiber composite domes, each with a steel insert at the center with a 3/4 G internal threaded hole.

The components of the fluidic line are the following:

- Burst disk ('BD-1'): a burst disk which serves as safety in case of a high pressure inside the hydrogen peroxide tank.
- Manual ball valve 1/4" Ham-Let H800 ('FD-Ox'): a mechanical ball valve used to fill, drain and create vacuum inside the hydrogen peroxide tank[9].

Figure 2.18: Burst Disk

Figure 2.19: Manual ball valve Ham-Let H800.

- Cavitating Venturi ('Venturi') : a nozzle used to fix or lock the flowrate of a liquid, making it not dependent on downstream conditions or fluctuations. This is similar to what a sonic nozzle does to a gas flow: the flowrate follows the inlet pressure and is not sensitive to downstream conditions. The cavitating Venturi, however, uses the liquid vapor pressure point to limit or lock the flow. The throat of a cavitating Venturi is sized so that the differential pressure generated from the inlet section to the throat reduces the liquid absolute pressure to its vapor pressure: in these conditions the liquid starts to vaporize or boil. Vapor bubbles begin then to physically block the throat passageway: this prevents any additional increase in flowrate. If the inlet pressure is increased, this also raises the throat pressure, taking the liquid at the throat out of its vapor pressure point. Additional flow may now pass through the Venturi which in-turn generates a higher differential pressure. This decreases the throat pressure to the vapor pressure again and a new higher fixed flowrate is found.

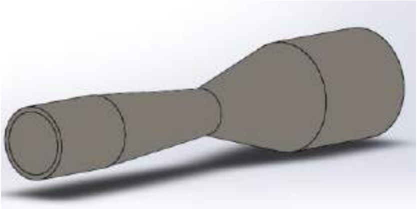

Figure 2.20: Cavitating Venturi.

- Manual ball valve Ham-Let H6800 with cylinder actuator ('Vox-1'): a ball valve actuated with a pneumatic cylinder. It is used to start the sounding rocket[9].

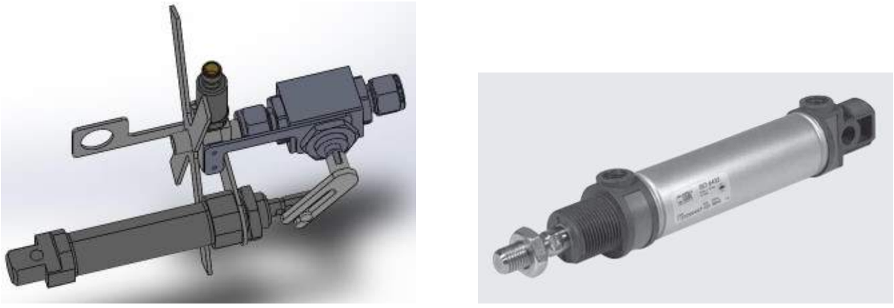

Figure 2.21: Manual ball valve Ham-Let H6800 connected to cylinder actuator.

- Solenoid valve Ham-Let Z-SVD ('A-2'): a solenoid valve attached to the actuator to create an electro-pneumatically actuated ball valve.
- Miniature Pressure Regulator Tescom BB-1 ('PR-2') : a control valve that reduces the input pressure of a fluid to a desired output value (in our case 5-8 bar).
- CO_2 tank Ham-Let HSSC153BH: tank filled with compressed CO_2 used for Vox-1 actuation[9].
- Manual ball valve Ham-Let H6800 ('Vox-2'): a mechanical ball valve which serves as safety valve. It is opened before the pressurization and if Vox-1 fails it can stop the flow before reaching the catalytic reactor.

Figure 2.22: Solenoid valve Ham-Let Z-SVD.

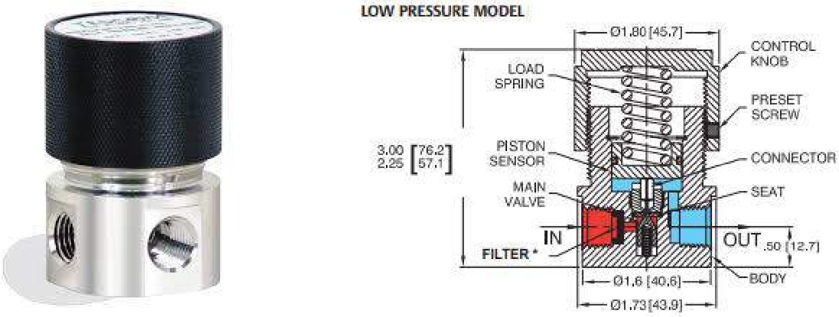

Figure 2.23: Miniature Pressure Regulator Tescom BB-1.

Figure 2.24: CO_2 tank Ham-Let HSSC153BH.

Chapter 3

Rocket Preliminary Design

The objective of the third chapter is the introduction and description of the project's firsts steps, that concern the general dimensioning of the rocket, executed in *MatLab*.

The external structure of a rocket is crucial to the rockets overall weight, strength, and stiffness. The goal is always to maximize strength and stiffness while minimizing weight and cost.

The aim of the preliminary design using a *MatLab* script was to detect how an entirely carbon composite external structure would behave and which would be the impact over the weight and the overall performance of the sounding rocket.

Furthermore, stated that one of the structural requirements is the use of carbon fiber as the main element, initially the chapter focuses on theories developed to design and analyze composite structures, then the code will be taken up and its most important points will be shown.

3.1 Composite characteristics analysis

As mentioned in 1.4.1, composite materials are anisotropic and non-homogeneous materials, with properties strongly dependent on the direction of the applied load.[7]

It can be defined three levels of study of properties:

1. Micro-mechanical level which describes how the interaction between

the constituent phases of the material reflects on the overall properties

2. Macro-mechanical level that examines the average properties thanks to the homogenization hypothesis (the composite material is considered continuous, homogeneous, strongly anisotropic)

3. Laminate level, of a higher order than the other two, which allows evaluating how the orientation of different plies overlapped affects the mechanical properties of the laminate.

Along this paragraph only the last two levels will be covered, they lead to the classical lamination theory (CLT). In addition, will be described also the netting analysis.

3.1.1 Netting Theory

In the early 60's, the netting theory was widely used in the pressure vessels design for aerospace and defense applications. Since that time, sophisticated composite analysis software has been developed than can give valuables results about composite structures behavior and performance.[19] Anyway, netting analysis can be used effectively as a standalone tool and as a means of double-checking product designs developed using composite design software.

The assumption underlying the netting theory are:

- the tube wall acts as a membrane, carrying no out-of plane bending or shear loads;

- all loads are assumed to be carried by the fiber with no contribute from the matrix resin;

- there is no interaction between fiber layers stacked at different orientation.

For any location along a cylinder, the composite wall is subjected to membrane loads N_θ and N_ϕ in the hoop and meridian directions, respectively, as is shown in figure 3.1. Figure 3.2 shows a single layer of a tubular structure. Because the fibers carry all applied loads, the unit element shown in Fig. 3.2 satisfies equilibrium only if:

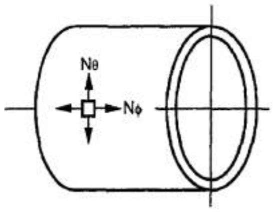

Figure 3.1: Orientation of membrane loads N_θ and N_ϕ for composite cylinder

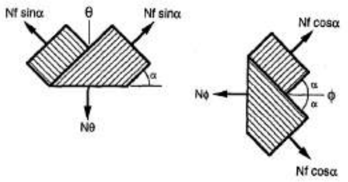

Figure 3.2: Orientation of membrane loads N_θ and N_ϕ for composite cylinder

$$N_\theta = 2N_f \sin^2 \alpha \tag{3.1}$$

and

$$N_\phi = 2N_f \cos^2 \alpha \tag{3.2}$$

where N_f is the load carried by the fiber of a single ply. Clearly a single layer is composed by two plies, because usually composite cylinder structures are manufactured using the filament winding technique.[8]

The total load carried by a collection of plies is obtained by:

$$N_\theta = \sum_{j=1}^{n} 2n_j N_{f_j} \sin^2 \alpha_j \tag{3.3}$$

and

$$N_\phi = \sum_{j=1}^{n} 2n_j N_{f_j} \cos^2 \alpha_j \tag{3.4}$$

where $n_1, n_2, \ldots, n_n$ are the plies stacked at angles $\alpha_1, \alpha_2, \ldots, \alpha_n$.

For a closed ends pressure vessel with radius R, subjected to internal pressure P, the membrane loads are:

$$N_\theta = PR \qquad \left[\frac{\text{N}}{\text{mm}}\right] \tag{3.5}$$

$$N_\phi = \frac{PR}{2} \qquad \left[\frac{\text{N}}{\text{mm}}\right] \tag{3.6}$$

Generally, tubular composite structures are made using relatively low-angle helical layers and 90-deg hoop layers. The helical layers carry meridian loads, N_ϕ, and the hoop layers, with a small contribution by the helical ones, carry the circumferential loads N_θ. Then, the allowable design stress σ_{ut} is defined by:

$$\sigma_{ut} = \frac{X_t}{FS} \quad [\text{MPa}] \tag{3.7}$$

where X_t is the ultimate strength of unidirectional composite and FS the safety factor chosen.

The netting equations applicable to this combination that gives us the total thickness necessary to carry all the loads are:

$$t_{\alpha,f} = \frac{N_\theta}{\sigma_{ut}\cos^2\alpha} \quad [\text{mm}] \tag{3.8}$$

for the helical part with winding angle of α, and

$$t_{90,f} = \frac{N_\theta - N_\phi \tan^2\alpha}{\sigma_{ut}} \quad [\text{mm}] \tag{3.9}$$

for the hoop fibers.

To calculate the total thickness is necessary to use the fiber volume fraction V_f, that includes the presence of the matrix in the composite structure. The equation is:

$$t = \frac{t_{\alpha,f} + t_{90,f}}{V_f} \quad [\text{mm}] \tag{3.10}$$

3.1.2 Macro mechanic level

First, the lamina (or ply) is assumed as an anisotropic elastic material. The assumption of elastic behavior is reasonable because the composite materials have an almost linear relationship between tension and deformation practically up to the breaking load (brittle fracture,no possibility of plastic deformation).[7]

Since the anisotropic law generally provides a complete coupling between the stress vector and the deformation vector (both with 6 components in the Cartesian reference system $x; y; z$) the stiffness matrix $[K]$, or rather the 'responsible' matrix of these couplings, is complete and therefore composed of 36 components. Thanks to the hypothesis of elastic behavior, however, it is possible to demonstrate that this matrix is symmetrical so that the independent constants that constitute it are reduced to 21. The obtained relationship is the following:

$$\begin{Bmatrix} \sigma_{xx} \\ \sigma_{yy} \\ \sigma_{zz} \\ \tau_{yz} \\ \tau_{zx} \\ \tau_{xy} \end{Bmatrix} = \begin{bmatrix} K_{11} & K_{12} & K_{13} & K_{14} & K_{15} & K_{16} \\ Sym & K_{22} & K_{23} & K_{24} & K_{25} & K_{26} \\ Sym & Sym & K_{33} & K_{34} & K_{35} & K_{36} \\ Sym & Sym & Sym & K_{44} & K_{45} & K_{46} \\ Sym & Sym & Sym & Sym & K_{55} & K_{56} \\ Sym & Sym & Sym & Sym & Sym & K_{66} \end{bmatrix} \begin{Bmatrix} \varepsilon_{xx} \\ \varepsilon_{yy} \\ \varepsilon_{zz} \\ \gamma_{yz} \\ \gamma_{zx} \\ \gamma_{xy} \end{Bmatrix} \tag{3.11}$$

A further simplification could be made thanks to the symmetry properties of CFRP materials. One or more planes of symmetry can be identified in the material. In particular, for composite materials with unidirectional fibers, the symmetry planes are three, orthogonal to each other, as shown in the figure 3.3.

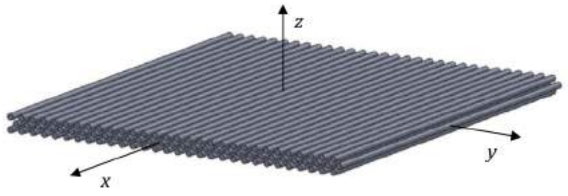

Figure 3.3: Lamina/Ply coordinate reference system

These planes of symmetry allow us to identify a reference axis system $x; y; z$ inside the material. In general we consider the origin of this system lying in the middle plane of the ply, the x axis coinciding with the fibers direction, the z axis in the thickness direction and the y axis perpendicular to the x-z plane.

The materials with these characteristics are called orthotropic and have a stiffness matrix composed of 9 independent constants:

$$\begin{Bmatrix} \sigma_{xx} \\ \sigma_{yy} \\ \sigma_{zz} \\ \tau_{yz} \\ \tau_{zx} \\ \tau_{xy} \end{Bmatrix} = \begin{bmatrix} K_{11} & K_{12} & K_{13} & 0 & 0 & 0 \\ Sym & K_{22} & K_{23} & 0 & 0 & 0 \\ Sym & Sym & K_{33} & 0 & 0 & 0 \\ 0 & 0 & 0 & K_{44} & 0 & 0 \\ 0 & 0 & 0 & 0 & K_{55} & 0 \\ 0 & 0 & 0 & 0 & 0 & K_{66} \end{bmatrix} \begin{Bmatrix} \varepsilon_{xx} \\ \varepsilon_{yy} \\ \varepsilon_{zz} \\ \gamma_{yz} \\ \gamma_{zx} \\ \gamma_{xy} \end{Bmatrix} \tag{3.12}$$

Thus, the orthotropy only keeps out of the main diagonal the couplings between axial deformations and transverse stresses.

Introducing now the engineering properties characterizing these equations we obtain:

$$\begin{Bmatrix} \varepsilon_{xx} \\ \varepsilon_{yy} \\ \varepsilon_{zz} \\ \gamma_{yz} \\ \gamma_{zx} \\ \gamma_{xy} \end{Bmatrix} = \begin{bmatrix} \frac{1}{E_x} & \frac{-\nu_{yx}}{E_y} & \frac{-\nu_{zx}}{E_z} & 0 & 0 & 0 \\ \frac{-\nu_{xy}}{E_x} & \frac{1}{E_y} & \frac{-\nu_{zy}}{E_z} & 0 & 0 & 0 \\ \frac{-\nu_{xz}}{E_x} & \frac{-\nu_{yz}}{E_y} & \frac{1}{E_z} & 0 & 0 & 0 \\ 0 & 0 & 0 & \frac{1}{G_{yz}} & 0 & 0 \\ 0 & 0 & 0 & 0 & \frac{1}{G_{zx}} & 0 \\ 0 & 0 & 0 & 0 & 0 & \frac{1}{G_{xy}} \end{bmatrix} \begin{Bmatrix} \sigma_{xx} \\ \sigma_{yy} \\ \sigma_{zz} \\ \tau_{yz} \\ \tau_{zx} \\ \tau_{xy} \end{Bmatrix} \tag{3.13}$$

in which, E_i are the elastic modules, proportionality constants in the three directions, longitudinal and transversal, ν_{ij} are the Poisson coefficients (with i the axis relative to the solicitation and j the one relative to the shrinkage), responsible for the coupling between axial deformations and transverse stresses and G_{ij} are the shear stiffness modules.

The matrix characterizing the last relation is called matrix of compliance, $[S]$ and is the inverse of the initially exposed stiffness matrix.

Finally, it could be observed that a composite material constituted by unidirectional plies presents a transverse isotropy. This characteristic does not change the number of non-null components of the compliance matrix, but rather imposes the equivalence of the properties in the two lamina directions y e z.

So we can reduce the notations used so far, indicating the direction of the fiber with the number 1 (axial) and the generic direction perpendicular to it with 2 (transverse).

$$\left\{\begin{matrix} \varepsilon_{xx} \\ \varepsilon_{yy} \\ \varepsilon_{zz} \\ \gamma_{yz} \\ \gamma_{zx} \\ \gamma_{xy} \end{matrix}\right\} = \begin{bmatrix} \frac{1}{E_1} & \frac{-\nu_{21}}{E_2} & \frac{-\nu_{21}}{E_2} & 0 & 0 & 0 \\ \frac{-\nu_{12}}{E_1} & \frac{1}{E_2} & \frac{-\nu_{22}}{E_2} & 0 & 0 & 0 \\ \frac{-\nu_{12}}{E_1} & \frac{-\nu_{22}}{E_2} & \frac{1}{E_2} & 0 & 0 & 0 \\ 0 & 0 & 0 & \frac{2(1+\nu_{22})}{E_2} & 0 & 0 \\ 0 & 0 & 0 & 0 & \frac{1}{G_{21}} & 0 \\ 0 & 0 & 0 & 0 & 0 & \frac{1}{G_{21}} \end{bmatrix} \left\{\begin{matrix} \sigma_{xx} \\ \sigma_{yy} \\ \sigma_{zz} \\ \tau_{yz} \\ \tau_{zx} \\ \tau_{xy} \end{matrix}\right\} \tag{3.14}$$

The equations introduced until now are needed to describe a generic three-dimensional state stress. Under properly conditions, however, it is useful to approximate the load acting on a thin laminate by a state of plane stress.

The constitutive equation is simplified:

$$\left\{\begin{matrix} \varepsilon_1 \\ \varepsilon_2 \\ \gamma_{12} \end{matrix}\right\} = \begin{bmatrix} \frac{1}{E_1} & \frac{-\nu_{21}}{E_2} & 0 \\ \frac{-\nu_{12}}{E_1} & \frac{1}{E_2} & 0 \\ 0 & 0 & \frac{1}{G_{12}} \end{bmatrix} \left\{\begin{matrix} \sigma_1 \\ \sigma_2 \\ \tau_{12} \end{matrix}\right\} \tag{3.15}$$

Thus, four independent constants remain: E_1, E_2, ν_{12} (ν_{21} is determined thanks to symmetry) and G_{12}.

The stress-strain relation is obtained by inversion of the compliance matrix:

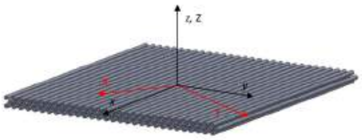

Figure 3.4: Rotation of the axis reference system in the middle plane.

$$\begin{Bmatrix} \sigma_1 \\ \sigma_2 \\ \tau_{12} \end{Bmatrix} = \frac{1}{1-\nu_{12}\nu_{21}} \begin{bmatrix} E_1 & \nu_{12}E_2 & 0 \\ \nu_{12}E_2 & E_2 & 0 \\ 0 & 0 & G_{12}(1-\nu_{12}\nu_{21}) \end{bmatrix} \begin{Bmatrix} \varepsilon_1 \\ \varepsilon_2 \\ \gamma_{12} \end{Bmatrix} = \begin{bmatrix} Q_{11} & Q_{12} & 0 \\ Q_{12} & Q_{22} & 0 \\ 0 & 0 & Q_{66} \end{bmatrix} \begin{Bmatrix} \varepsilon_1 \\ \varepsilon_2 \\ \gamma_{12} \end{Bmatrix} \tag{3.16}$$

where $[Q]$ is the reduced stiffness matrix of the ply in plane stress. Generally, a composite laminate is composed of several plies of different orientation.

Considering a rotated reference system by an angle θ, it is possible to calculate the relation stress-strain in the new coordinate system.

The rotation matrix $[T]$ allows to rotate the components of the deformation and stress tensors from the new reference system to the previous one; the inverse of this matrix instead allows the opposite operation.

$$[T] = \begin{bmatrix} \cos^2\theta & \sin^2\theta & 2\sin\theta\cos\theta \\ \sin^2\theta & \cos^2\theta & -2\sin\theta\cos\theta \\ -\sin\theta\cos\theta & \sin\theta\cos\theta & \cos^2\theta-\sin^2\theta \end{bmatrix} \tag{3.17}$$

It is necessary, however, to keep in mind that the components of the deformation tensor do not depend directly from the term γ_{xy}, but rather from its half, thus the matrix $[R]$ is introducing:

$$[R] = \begin{bmatrix} 1 & 0 & 0 \\ 0 & 1 & 0 \\ 0 & 0 & 2 \end{bmatrix}$$

We can now define the stress-strain relation in the new rotated reference system as:

$$\begin{Bmatrix} \sigma_1 \\ \sigma_2 \\ \tau_{12} \end{Bmatrix} = [T]^{-1}[Q][R][T][R]^{-1} \begin{Bmatrix} \varepsilon_1 \\ \varepsilon_2 \\ \gamma_{12} \end{Bmatrix} = [\overline{Q}] \begin{Bmatrix} \varepsilon_1 \\ \varepsilon_2 \\ \gamma_{12} \end{Bmatrix} \tag{3.18}$$

The matrix $[\overline{Q}]$ is called the transformed reduced stiffness matrix for the ply.

3.1.3 Laminate level: Classical Lamination Theory

CLT is a commonly used predictive tool to, which evolved after the 60s, which makes it possible to analyze complex coupling effects that may occur in composite laminates. With CLT is possible to predict strains, displacements and curvatures of a laminate that is mechanically and thermally loaded. The method is based on classical plate theory, with the main difference appearing in the lamina stress-strain relationships.[15]

The assumptions made in order to make the problem solvable are:

1. The composite shell consists of orthotropic plies bonded together, with the principal material axes of the orthotropic lamina orientated along arbitrary directions with respect to the x-y axes.
2. the thickness of the plate, t, is much smaller than any characteristic dimension.
3. The displacements over the 3 directions, respectively u, v, and w are small compared with t.
4. The in-plane strains ε_x, ε_y, and γ_{xy} are small compared with unity.
5. Transverse shear is negligible, $\gamma_{xz} = \gamma_{yz} = 0$.
6. Displacements u and v are assumed to be linear functions of the thickness coordinate z (no warping).
7. Transverse normal strain ε_z is negligible.
8. Each ply obeys Hooke's Law.

9. The plate thickness is constant throughout the laminate.

10. Transverse shear stresse τ_{xz} and τ_{yz} are equal to zero on the laminate surfaces $z = t/2$.

As we said, starting from the classical plate theory, which describes the behavior structural of the thin bodies, the state of deformation in a generic point of the plate is defined as a function of the deformation vectors in the middle plane $\{\varepsilon_0\}$ and of the vector of the curvature rays $\{\kappa\}$:

$$\{\varepsilon\} = \{\varepsilon_0\} + z\{\kappa\} \tag{3.19}$$

with z the distance of the generic point from the middle plane.

This equation, called Kirchhoff assumption, can, with good approximation, be used to describe the deformation of a thin laminate in its axis reference system. However, a laminate is composed of N overlapped plies, each one with its lamina axis reference system which may not be aligned with the laminate axis.

The axis reference system of the laminate has the z axis in the direction of the thickness, with the origin in the middle plane.

Indicating the thickness of the laminate with t, the one of the singles plies with t_k and the height starting from the middle plane to the nearest edge of the k-th lamina with z_k, it is possible to write:

$$t_k = z_k - z_{k-1} \tag{3.20}$$

$$t = \sum_{k=1}^{n} t_k \tag{3.21}$$

$$\overline{z}_k = \frac{z_k - z_{k-1}}{2} \tag{3.22}$$

where $\overline{z}_k$ is the distance between the middle plane of the laminate and the middle plane of the k-th ply.

Thanks to the rotation matrix introduced in the previous paragraph it is possible to write the relation between the deformation of the laminate and the stress of each single ply.

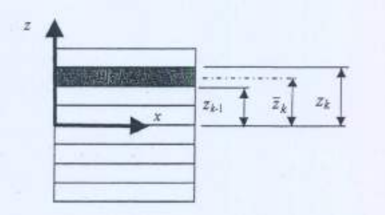

Figure 3.5: Thickness coordinates of a ply

$$\begin{Bmatrix} \sigma_1 \\ \sigma_2 \\ \tau_{12} \end{Bmatrix} = [\overline{Q}]_k \begin{Bmatrix} \varepsilon_1 \\ \varepsilon_2 \\ \gamma_{12} \end{Bmatrix} \tag{3.23}$$

And integrating the plies stresses over the laminate thickness we can obtain the forces and the moments acting on the composite plate, it results:

$$N_x = \int_{-t/2}^{t/2} \sigma_1 dz \quad N_y = \int_{-t/2}^{t/2} \sigma_2 dz \quad N_{xy} = \int_{-t/2}^{t/2} \tau_{12} dz$$

$$M_x = \int_{-t/2}^{t/2} \sigma_1 z dz \quad M_y = \int_{-t/2}^{t/2} \sigma_2 z dz \quad M_{xy} = \int_{-t/2}^{t/2} \tau_{12} z dz$$

Using these relation in equation 3.23 we get the expression:

$$\int_{-t/2}^{t/2} \begin{Bmatrix} \sigma_1 \\ \sigma_2 \\ \tau_{12} \end{Bmatrix} dz = \sum_{k=1}^{n} \int_{z_{k-1}}^{z_k} \begin{bmatrix} \overline{Q_{11}} & \overline{Q_{12}} & 0 \\ \overline{Q_{12}} & \overline{Q_{22}} & 0 \\ 0 & 0 & \overline{Q_{66}} \end{bmatrix} (\{\varepsilon_0\} + z\{\kappa\}) dz \tag{3.24}$$

so, the forces acting on the laminate are:

$$\begin{Bmatrix} N_x \\ N_y \\ N_{xy} \end{Bmatrix} = \begin{bmatrix} A_{11} & A_{12} & A_{16} \\ A_{21} & A_{22} & A_{26} \\ A_{61} & A_{62} & A_{66} \end{bmatrix} \{\varepsilon_0\} + \begin{bmatrix} B_{11} & B_{12} & B_{16} \\ B_{21} & B_{22} & B_{26} \\ B_{61} & B_{62} & B_{66} \end{bmatrix} \{\kappa\} \tag{3.25}$$

Then, it can be seen how the forces flow in a laminate composed of several orthotropic plies are due to two different contributions: membrane deformation, linked to the deformation of the middle plane, and of membrane-flexural coupling, caused by the curvature of the laminate itself.

Similarly, multiplying equation 3.23 by the term z and writing an expression like 3.24 we obtain the moment flows:

$$\begin{Bmatrix} M_x \\ M_y \\ M_{xy} \end{Bmatrix} = \begin{bmatrix} B_{11} & B_{12} & B_{16} \\ B_{21} & B_{22} & B_{26} \\ B_{61} & B_{62} & B_{66} \end{bmatrix} \{\varepsilon_0\} + \begin{bmatrix} D_{11} & D_{12} & D_{16} \\ D_{21} & D_{22} & D_{26} \\ D_{61} & D_{62} & D_{66} \end{bmatrix} \{\kappa\} \qquad (3.26)$$

In the latter case it can be noted that the moments are related to the deformation of the laminate by the matrix $[B]$ that couples membranous-flexural deformations, and to the curvature by the matrix $[D]$, representing the bending stiffness.

Some terms of the matrices $[A]$, $[B]$ and $[D]$ can cause undesirable coupling effects, like between curvature and in-plane loading, or between membrane deformation and bending loads. In figure 3.6 all these coupling phenomena are illustrated.

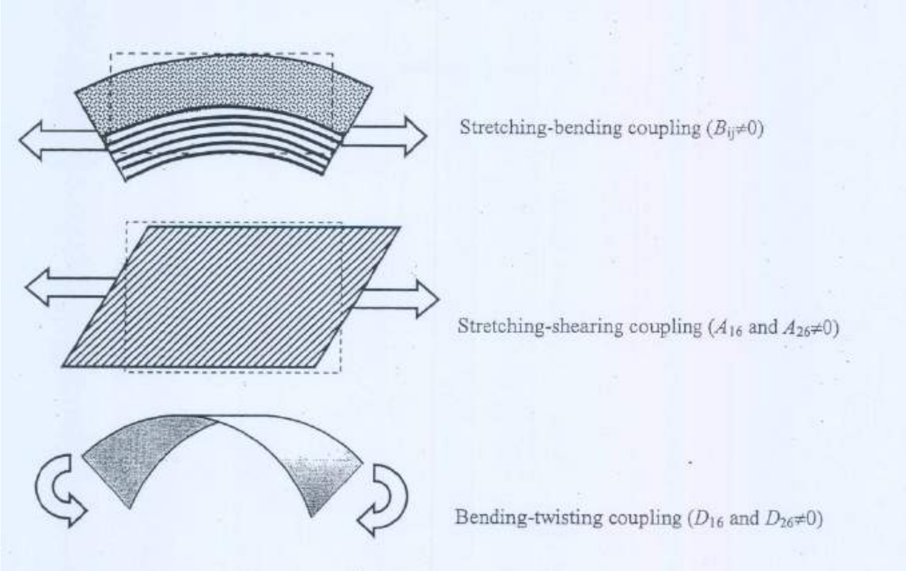

Figure 3.6: Examples of coupling of deformations.

It is possible to set some lay-up rules in order to avoid these coupling effects. A symmetrical laminate does not present the membrane-flexural coupling as the contributions to the matrix $[B]$ of the two symmetrical plies compensate. Furthermore, in the case of balanced laminate, the terms of coupling between stretching and shearing $A_{16} = A_{61}$ and $A_{26} = A_{62}$ disappear because the contributions provided by two identical plies but with orientation respectively of $+\theta$ and ˘θ are equal and opposite. Finally, if the laminate is anti-symmetrical the terms $D_{16} = D_{61}$ and $D_{26} = D_{62}$ are also eliminated, removing the bending/twisting coupling.

3.2 Composite Failure Analysis

Conventional materials, such as metals, are generally isotropic, so the strength are quite independent of direction. Moreover, metals, due to them failure mode, have a similar strength in tension and compression. Also, in most applications, these materials are independent of strain rate and temperature.

Composite, instead, are usually highly anisotropic, and as a result the strength is dependent on direction. They are characterized by different failure modes, so there are significant difference between tensile and compressive strength. The rate and temperature sensitivity of fibres and matrix are also reflected in the failure of composite.

Failure criteria for conventional isotropic materials have traditionally been based on stress calculations, so to implement the failure analysis of composite in FE-software was convenient the use of the same stress criteria. However, due to the different orientation of the plies, the stress plot along the thickness fluctuate violently. On the contrary, strains are continuous through the thickness for laminates without cracks. It means that failure strains are less dependent on fibre direction than failure stresses. For these reasons strain based failure criteria are more suitable for composite materials. Over the last three decades, there have been continuous efforts in developing failure criteria for unidirectional fiber composites and their laminates. Currently, there exist a large number of lamina failure criteria and laminate failure analysis methods. [15]

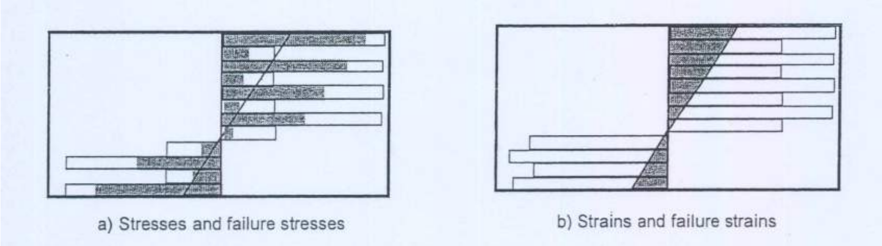

Figure 3.7: Stress and strain variation through the thickness of a laminate.

3.2.1 First Ply Failure vs Progressive Ply Failure

First Ply Failure (FPF) is a method commonly used to predict the strength of a laminate. Once the stress in each ply is known, calculated from CLT when the loads are defined, a failure criterion is used to determine the load at which any one of the plies in the layup fails. With FPF, the laminate is assumed to have failed with the first ply fails.[16]

One of the advantages of first ply failure is that it is numerically straight forward and easy to use. It permits to determine directly the Pass/Fail for a given condition.

A drawback with this approach is that, although the composite is orthotropic, homogenized lamina properties are used to evaluate failure. The properties of the matrix and fiber are smeared to produce a single set of properties. As such, the constituent properties are not fully utilized and their response is not differentiated. This can result in inaccurate estimates of strength and the masking of key failure modes in some applications.

The Progressive Ply Failure (PPF) allows to see what happens beyond first ply failure. As with first ply failure, CLT is utilized to evaluate each ply against a specified failure criterion without stopping at the first failure. At each integration point in a finite element model, after a failure criterion is satisfied (a ply has failed), the material stiffness is reduced to a fraction of the original stiffness. When the stiffness at an integration point is reduced, the amount of load that element can carry is reduced and loads are rerouted around the failed element into the surrounding unfailed elements.

As this process is carried out in a large composite structure that has multiple integration points, the result is a progressive weakening of the entire structure; as individual elements fail, loads are rerouted into surrounding elements which in turn fail. This process continues until the load carrying capability of the composite structure is reduced to the point where the structure can no longer continue to carry more load, indicating ultimate failure. The process is inherently nonlinear as it degrades laminate stiffness and extends beyond the initiation of failure (linear elasticity ends).

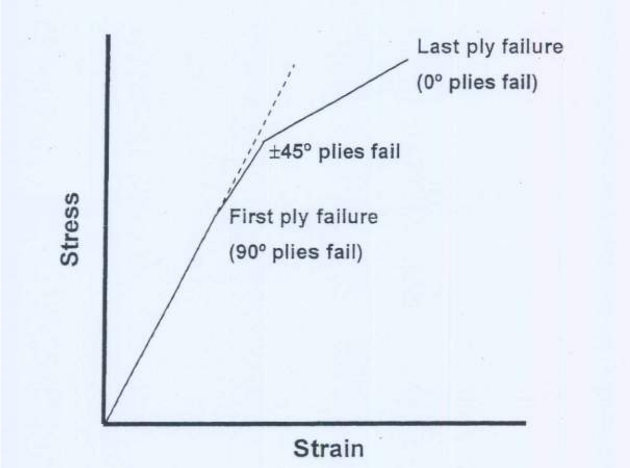

Figure 3.8: Example of failure sequence on a [90/+45/-45/0] lay-up.[15]

3.2.2 Failure Criteria

The majority of the lamina failure criteria were developed for two-dimensional stress states in orthotropic materials and they can be categorized into three groups:

- *Limit criteria*, they predict failure load and mode by comparing lamina stresses or strains with the corresponding strengths separately, they not consider interaction among the stresses (or strains) exert on the two plane axis;

- *Interactive criteria*, they predict the failure load by using a single quadratic or higher order polynomial equation involving all stress (or strain) components. Failure is assumed when the equation is satisfied;

- *Separate mode criteria*, they separate the matrix failure criterion from the fiber failure criterion. The equations can be dependent on either one or more stress components.

Ply failure criteria are normally evaluated in the local coordinate system of the ply, where the axes coincide with the principal material axes of the ply.

The simplest and commonly used failure criteria for composites, that belong to the first group, are the maximum strain and maximum stress criteria. They state that failure occurs when the ply reaches any of the failure strains or stresses obtained from uniaxial tests. For the maximum strain and stress criteria failure occur, respectively, when:

$$\begin{cases} \varepsilon_1 < \varepsilon_{1uc} \; or \; \varepsilon_1 > \varepsilon_{1ut} \\ \varepsilon_2 < \varepsilon_{2uc} \; or \; \varepsilon_2 > \varepsilon_{2ut} \\ |\gamma_{12}| > \gamma_{12u} \end{cases} \qquad \begin{cases} \sigma_1 < \sigma_{1uc} \; or \; \sigma_1 > \sigma_{1ut} \\ \sigma_2 < \sigma_{2uc} \; or \; \sigma_2 > \sigma_{2ut} \\ |\tau_{12}| > \tau_{12u} \end{cases} \tag{3.27}$$

Plots of the these criteria in the local strain and stress coordinate of the ply are shown in figure 3.9.

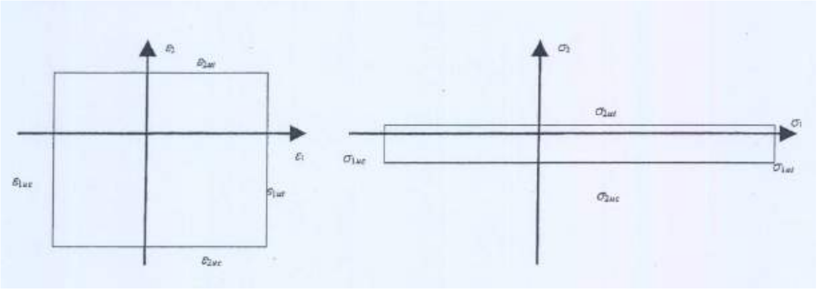

Figure 3.9: Maximum strain and maximum stress criteria.

As said, the major drawback of the maximum strain and maximum stress criteria is that they do not consider interaction between different stresses, which results in a discontinuous failure envelope.

The most common interactive criterion for isotropic materials is the Von Mise's criterion. A generalisation of this criterion to orthotropic materials was suggested by Hill (1950). Azzi and Tsai (1965) proposed to use this expression for composite materials and they suggested that tensile and compressive loads may be considered in the criterion by using the corresponding strengths. The equation of the called "Tsai-Hill criterion" is,[15]:

$$\frac{\sigma_1^2}{X^2} + \frac{\sigma_2^2}{Y^2} - \frac{\sigma_1 \sigma_2}{W^2} + \frac{\tau_{12}^2}{S^2} = 1 \tag{3.28}$$

where:

$$X = \begin{cases} X_t \ , \ \sigma_1 \geq 0 \\ X_c \ , \ \sigma_1 < 0 \end{cases} \qquad Y = \begin{cases} Y_t \ , \ \sigma_2 \geq 0 \\ Y_c \ , \ \sigma_2 < 0 \end{cases} \qquad W = \begin{cases} X_t \ , \ \sigma_1 \sigma_2 \geq 0 \\ X_c \ , \ \sigma_1 \sigma_2 < 0 \end{cases}$$

Figure 3.10 plot an example of the criterion evaluated with equal and different strength values in tension and compression.

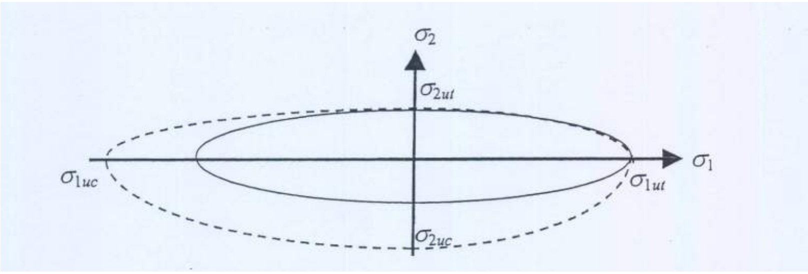

Figure 3.10: Tsai-Hill's criterion in ply stress coordinates.

Another general interactive criterion is the Tsai-Wu tensorial criterion, which for an orthotropic ply under plane stress simplifies to:

$$F_1 \sigma_1 + F_2 \sigma_2 + F_{11} \sigma_1^2 + F_{22} \sigma_2^2 + F_{12} \sigma_1 \sigma_2 + F_{66} \tau_{12}^2 = 1 \tag{3.29}$$

with:

$$F_1 = \tfrac{1}{X_t} - \tfrac{1}{X_c}, \quad F_{11} = \tfrac{1}{X_t X_c}, \quad F_2 = \tfrac{1}{Y_t} - \tfrac{1}{Y_c}, \quad F_{22} = \tfrac{1}{Y_t Y_c}$$

$$F_{66} = \tfrac{1}{S^2}, \quad F_{12} = F_{12}^* \sqrt{F_{11} F_{22}}$$

The term F_{12}^* is a user-defined interaction coefficient, usually setted after a biaxial test to experimentally determine it. Otherwise can be use $F_{12}^* = 1/2X_tX_c$ which reduces Tsai-Wu down to the Hoffman criterion.

Two failure criteria belonging to the third group are the Hashin failure criterion and the Puck failure criterion. As said, these criteria separate the matrix and the fiber failures using a different equation for each phase.

In Hashin failure criterion criticality of tensile loads in the fiber direction is predicted with the expression,[1]:

$$f_f = \left(\frac{\sigma_1}{X_t}\right)^2 + \left(\frac{\tau_{12}}{S}\right)^2, \quad \sigma_1 \geq 0 \tag{3.30}$$

Under compression loads in the fiber direction, failure is predicted with an independent stress condition:

$$f_f = \frac{\sigma_1}{X_c}, \quad \sigma_1 < 0 \tag{3.31}$$

In the case of tensile transverse stress, the expression for predicting matrix failure is:

$$f_m = \left(\frac{\sigma_2}{Y_t}\right)^2 + \left(\frac{\tau_{12}}{S}\right)^2, \quad \sigma_2 \geq 0 \tag{3.32}$$

A more complex expression is used when the transverse stress is compressive:

$$f_m = \left(\frac{\sigma_2}{2S}\right)^2 + \left(\frac{\tau_{12}}{S}\right)^2 + \left[\left(\frac{Y_c}{2S}\right)^2 - 1\right]\frac{\sigma_2}{Y_t}, \quad \sigma_2 < 0 \tag{3.33}$$

Then, the most critical of the failure modes, for each grid point, is selected:

$$f = max(f_f, f_m) \tag{3.34}$$

failure occurs when f reaches the value of one.

In a similar way, the Puck criterion calculate the fiber failure with,[14]:

$$f_f = \frac{\sigma_1}{X}, \qquad X = \begin{cases} X_t \ , \ \sigma_1 \geq 0 \\ X_c \ , \ \sigma_1 < 0 \end{cases} \tag{3.35}$$

and the matrix failure with the expression:

$$f_m = \frac{\sigma_2^2}{Y_t Y_c} + \left(\frac{\tau_{12}}{S}\right)^2 + \left(\frac{1}{Y_t} + \frac{1}{Y_c}\right)\sigma_2 \tag{3.36}$$

As in Hashin criterion, the failure occurs for either f_f or f_m reaching the value one and the failure function criterion is the same.

3.2.3 Comparison with Experimental Data

The ability of the lamina failure criteria to correctly predict failure strength can be evaluated by comparing with experimental results. Except for longitudinal and transverse tensile strengths X and Y, good measurements of the compressive and shear strengths are not easy to obtain, which makes an objective assessment of the lamina failure criteria all the more difficult. Assuming that reliable uniaxial strength properties are available, to evaluate the failure criteria, failure loads of a lamina must be determined for a combined state of stress. Off-axis tension test offer a simply way to create a combined state of stress.[18]

Tests of a boron-epoxy system was conducted by Pipes and Cole, only angles of 15°, 30°, 45°, and 60° were experimented. The results are compared to failure criteria in figure 3.11. The Tsai-criterion criterion correlates with the data, in this case, nearly perfectly.

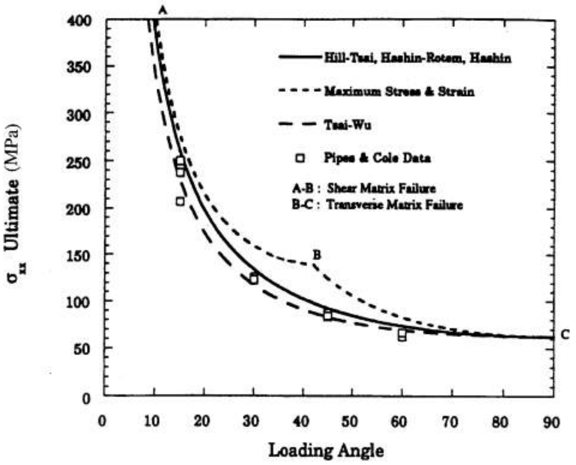

Figure 3.11: Comparison of lamina failure criteria to off-axis data

Another experiment set using T800 carbon fiber with an epoxy resin tested by Swanson and Qian, focusing on $\sigma_{22} - \tau_{12}$ biaxial data are shown in figure 3.12.

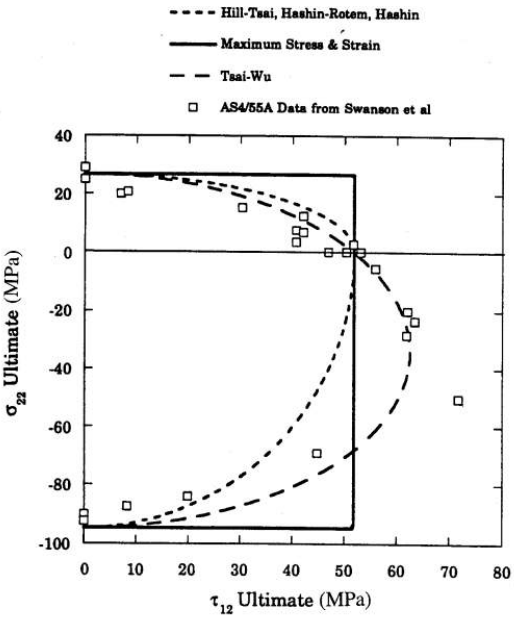

Figure 3.12: Comparison of lamina failure criteria to $\sigma_{22} - \tau_{12}$ data from Swanson et al.

Here is clear how difficult is the exactly prediction of the failure point. The Tsai-Wu criterion show a discrete correlation, but in some area Tsai-Hill and Hashin criteria perform better.

3.3 Aerodynamics and Forces acting on the Rocket

The structural design of a rocket is influenced by the interaction of all the applied loads and the response of the structure.

Launch loads are principally a function of motor chamber pressure, rocket acceleration level, and the interaction of the rocket and launcher during initial guidance.[11] During flight, the rocket is subjected to loads from motor thrust, aerodynamic lift, aerodynamic drag, inertia of rocket components, gravity and internal pressures. These loads are reacted by the rocket structure as axial load, shear load and bending moment, as is shown in figure 3.13, where the free body diagram illustrates these forces acting on the rocket.

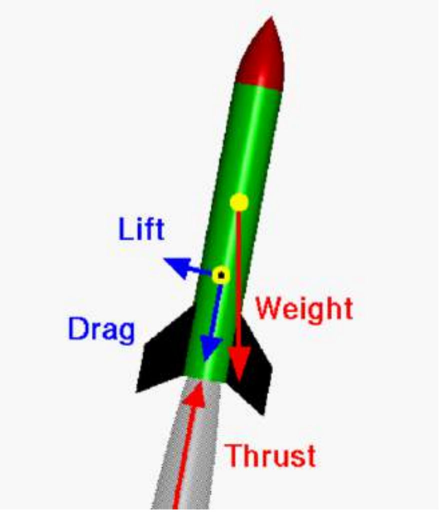

Figure 3.13: Forces on rocket during flight.

The point where the aerodynamic forces are applied is called 'Center of Pressure' (CP), while the other important point where the weight acts is the commonly known 'Center of Gravity' (CG).[13]

It is important to know where the CG and CP are in absolute measures and relative to each other. The rocket will always rotate around the center of gravity during flight, and gravity act on that singular point. However, the drag and lift forces do act on the center of pressure, and this decide how stable the rocket is.

The center of pressure must be behind the center of gravity in order for the rocket to remain stable. Imagine that a rocket is launched straight upwards, and a short burst of wind forces the wind to tilt slightly. After the wind burst relaxes, and given that the rocket is stable, the air pushing on the center of pressure will force it back into the wind again.

Considering now a free-body diagram of the axial forces acting on a rocket in powered flight, shown in figure 3.14, the equilibrium requires that:

$$am - T + F_A + mg\cos\theta = 0, \text{ N} \tag{3.37}$$

where

a = rocket acceleration along longitudinal axis, $\mathrm{m/s^2}$
T = rocket motor thrust, N

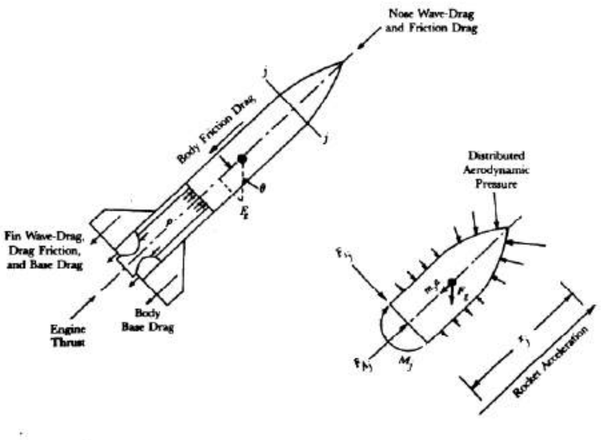

(A) Axial Loads (B) Principal Forces on Rocket Section

Figure 3.14: Axial loads on free flight rocket.

F_A = sum of axial components of aerodynamic forces, N
g = acceleration due to gravity, m/s^2
θ = angle between rocket longitudinal axis and local vertical, rad

And at any plane x-x the axial load F_{xx} is found by,[11]:

$$F_{A_{xx}} = am_x + F_{A_x} + m_x g \cos\theta - pA_{xx}, \text{ N} \tag{3.38}$$

where

$F_{A_{xx}}$ = axial load on rocket at plane x-x, N
m_x = rocket mass forward of plane x-x, kg
F_{A_x} = axial force on rocket forward of plane x-x, N
p = internal gage pressure, Pa
A_{xx} = area of the plane perpendicular to the longitudinal axis on which the internal pressure acts, m^2

The axial force terms on the rocket sections can be evaluated projecting the aerodinamics forces acting on the surface section on the longitudinal axis.

The projection of that forces on the perpendicular axis gives the normal forces F_N acting on each section. From this trend it is possible to calculate the bending moment M distribution on the rocket.

For preliminary design purposes, the rocket can be considered divided in sections, so the mass of the entire system can be distributed on the CG of the sections. The aerodynamics forces can be considered, for each part, to be concentrated at the CP of the sections.

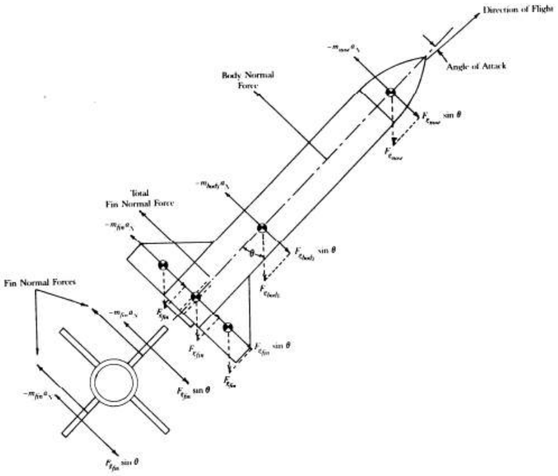

Figure 3.15: Concentrated loads on free flight rocket.

The normals loads acting on the rocket's section during flight are shown in figure 3.15. The total inertial load is equal to the mass of the section, multiplied by the acceleration acting in the direction perpendicular to the longitudinal axis. The expression to calculate the total bending moment are:

$$M_j = \sum_{i=1}^{n} F_{N_i}(x_j - x_i) + \sum_{i=1}^{n} M_i, \text{ Nm} \tag{3.39}$$

where

M_j = total bending moment acting at station j, Nm
F_{N_j} = normal force at station i, N
n = number of segments
M_i = local bending moment at station j, Nm

3.4 MatLab Script

As pointed in the previous paragraph, for preliminary design purposes, the rocket is divided in 6 cylindrical sections:

- nosecone;
- pressurizer tank;
- oxidizer tank;
- combustion chamber;
- nozzle;
- fins.

An `input_data.m` file contains the initial data to initialize some parts of the rocket structure and the design requirements data about the propulsion system.

Actually, each input in the relative initial *.m* file of the developed script can be change by the user, in order to analyze different combination or rocket systems. But, thanks to a know-how already present within the working group about the hybrid rocket motor, some parameters about the engine and the nozzle were kept fixed.

An excerpt from this file is visible here:

```
%% Input Data
%% Nosecone
D_rocket = 0.18;        % Diameter [m]
fineness_ratio = 4;     % Nose length/diameter

%% Payload
payload.mass = 50; [kg]
payload.cg_abs = [0.7 0 0]; [m]

%% Gas tank
gas_type = 'nitrogen'; % Helios or nitrogen
T_gas_tank = 293.15; % K

%% Engine
p_gas_tank = 300; % [bar]
tb = 25; % burning time [s]
m_dot = 2.2; % mass flow [kg/s]
pcc = 40; % combustion chamber pressure [bar]
p_tank = 40*1.5; % ox tank pressure [bar]
rho_prop = 1440;
rho_fuel = 920;

%% Nozzle
m_nozzle = 7; % kg
```

```
L_nozzle = 0.7; % m
cg_nozzle = [L_nozzle/3 0 0]; % m
Ixx_rho_nozzle = 1*10^-3;
Iyy_rho_nozzle = 1;
Izz_rho_nozzle = 1;
```

The geometric properties of interest for almost each part are:

- thickness, m
- structure volume, m^3
- moment of inertia for unit density, m^5
- CG relative position, m
- CG absolute position, m
- mass, kg
- internal volume, m^3

To save, manage and have an easy access to these properties is used the MatLab 'structure array'
A structure array is a data type that groups related data using data containers called fields. Each field can contain any type of data. Access data in a structure using dot notation of the form `structName(i).fieldName`.

A definition of this array structure is shown in the following code for the nozzle section (where the data are present in the input file):

```
%% Nozzle
module = 'nozzle';
nozzle = index_assign(module);
rocket_struct(nozzle).name = module;
rocket_struct(nozzle).mass = m_nozzle;
rocket_struct(nozzle).length = L_nozzle;
rocket_struct(nozzle).cg = cg_nozzle;
rocket_struct(nozzle).inertia_rho = [Ixx_rho_nozzle 0 0; 0...
                        Iyy_rho_nozzle 0; 0 0 Izz_rho_nozzle];
rocket_struct(nozzle).volume = 1;
```

For other parts like nosecone or oxidizer tank, a dedicated functions are implemented to calculate these properties and save them in the array structure. Figure 3.16 shows the results of these calculations.

The main code is based on two principal functions:

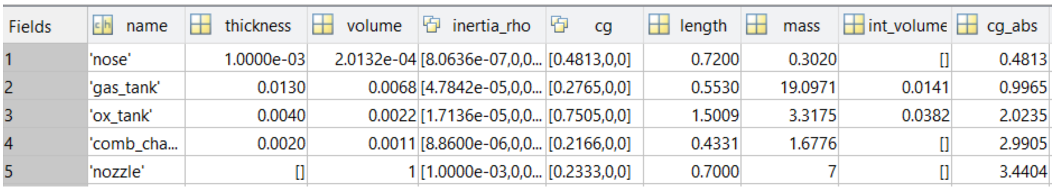

Fields	name	thickness	volume	inertia_rho	cg	length	mass	int_volume	cg_abs
1	'nose'	1.0000e-03	2.0132e-04	[8.0636e-07,0,0...	[0.4813,0,0]	0.7200	0.3020	[]	0.4813
2	'gas_tank'	0.0130	0.0068	[4.7842e-05,0,0...	[0.2765,0,0]	0.5530	19.0971	0.0141	0.9965
3	'ox_tank'	0.0040	0.0022	[1.7136e-05,0,0...	[0.7505,0,0]	1.5009	3.3175	0.0382	2.0235
4	'comb_cha...	0.0020	0.0011	[8.8600e-06,0,0...	[0.2166,0,0]	0.4331	1.6776	[]	2.9905
5	'nozzle'	[]	1	[1.0000e-03,0,0...	[0.2333,0,0]	0.7000	7	[]	3.4404

Figure 3.16: The rocket structure array.

- `trajectory_3D_fun.m`: describes the trajectory of the rocket integrating the equation of motion using `ode45` function, it gives as output the loads during the flight;
- `laminate_fun.m`: calculates the minimum thickness of a composite shell to support the loads (externals and internals) acting on the structures.

Firstly, after having read the input file, it runs a modified `trajectory_3D_fun.m` function that accepts some assumptions about the total mass, the inert mass, the total length and the CG position, therefore the inertia moment are calculated considering the rocket as a solid cylinder. This is necessary in order to initialize the loads with good approximation to use as boundary conditions for dimensioning the structures.

Then the main code is ready to run and calculate for each module the thickness of the carbon composite structure and, consequently, the geometric properties.

To understand how the process flows here it is displayed the calculus for the oxidizer tank:

```
%% OX tank
module = 'ox_tank';
ox_tank = index_assign(module);
rocket_struct(ox_tank).name = module;
% Geometric properties
rocket_struct(ox_tank).int_volume = m_prop/rho_prop;
rocket_struct(ox_tank).length = rocket_struct(ox_tank).int_volume/Af;
% Loads
loads.ox_tank.xx = loads.nose.xx - (rocket_struct(nose).mass + payload.mass)*
                                *max(a_long)+p_tank*100000*(D_rocket/2)^2*pi;
loads.ox_tank.yy = p_tank*100000*D_rocket/2;
% Laminate inizialization
SRmin = 0;
```

```
ply_add = 0;
% Laminate function
laminate_loads;
while SRmin < 1*FS_tank
    laminate_stacking;
    [SRmin, rocket_struct(ox_tank).thickness] = laminate_fun(module);
    ply_add = ply_add + 2;
end

[rocket_struct(ox_tank).volume, rocket_struct(ox_tank).inertia_rho, ...
    rocket_struct(ox_tank).cg] = ...
    tank_geom_properties(rocket_struct(ox_tank).length,...
                                rocket_struct(ox_tank).thickness, D_rocket);
rocket_struct(ox_tank).mass = rocket_struct(ox_tank).volume*1500;
```

As we can see, the code saves some properties of the module `Ox tank` to the relative array structure.
Another array structure is used to save the loads, in this piece of code it is possible to recognize the loads on the x-direction (parallel to the longitudinal axis of the rocket) evaluated using equation 3.38. In the y-direction we have just the load due the tank internal pressure.
Then the `laminate` function calculates the minimum necessary thickness to withstand the applied loads, multiplied by a safety factor `FS_tank`. Finally, the missing geometric properties are calculated and saved in the array structure.

The `laminate` function is based on the CLT.
The strength ratio (SR) is calculated using the Tsai-Hill failure model with the First Ply Failure criteria.
Basically, in each module, the laminate initialization set the `SR_min = 0` and the number of plies added $= 0$.
Then the laminate function applies the loads to an infinite extended lamina, until the SR reaches the value of 1 (that means the laminate are not failing) the `while` cycle add two plies (0° and 90° directions) at the thickness of the previous step.
The ply type selected are an unidirectional T300 carbon fiber-epoxy resin, the mechanical characteristic are summarized in table 3.1.

During the dimensioning of the modules, the main code creates a structure array also for the time-dependent variables, that are the oxidizer and fuel geometric properties, as seen in figure 3.17.

E_1	181 GPa
E_2	10,3 GPa
G_{12}	7,17 GPa
τ_{12}	0,28

X_t	1500 MPa
X_c	1500 MPa
Y_t	40 MPa
Y_c	246 MPa
S	68 MPa

Table 3.1: Unidirectional T300 carbon fiber ply properties

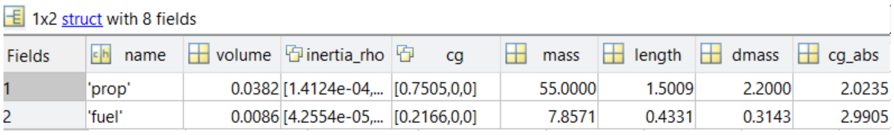

1x2 struct with 8 fields

Fields	name	volume	inertia_rho	cg	mass	length	dmass	cg_abs
1	'prop'	0.0382	[1.4124e-04,...	[0.7505,0,0]	55.0000	1.5009	2.2000	2.0235
2	'fuel'	0.0086	[4.2554e-05,...	[0.2166,0,0]	7.8571	0.4331	0.3143	2.9905

Figure 3.17: Time-dependent variables structure array.

Now, everything is ready to run again in the complete `trajectory_3D_fun.m`. This time no assumption is needed, the function integrate the differential equation using a *ode45* scheme. The time-dependent variables vary along the integration time, of course.

The result is a new trajectory that took in account a more real structure, a good approximation of the movement of the CG rocket and the variation of the moment of the inertia due to the oxidizer/fuel discharge.

Here it is possible to see the vector of the variables that enter in the integration scheme:

```
function dy= trajectory_3D_fun_ODE(~,y,~,m_dot,m_dot_f,r_tank,A_f,Ltot,...
                                m_f, cg_struct, I_struct, rocket_tvar,...
                                D_rocket, D_porta,a,n)
%Y0 = [vx0 vy0 x0 y0 m0 mp0 mf0 Lcg_rocket Lcg_tank L_ox0 I0 w0 Beta0 D_core0]
```

where

v_x = speed in x-direction, m/s;

v_y = speed in y-direction, m/s;

x = position on x-axis, m;

y = position on y-axis, m;

m = total mass, kg;

m_p = oxidizer mass, kg;

m_f = fuel mass, kg;
$Lcg\ rocket$ = CG position of the rocket from the nose, m;
$Lcg\ tank$ = CG position of the oxidizer tank from the nose, m;
$Lcg\ Ox$ = CG position of the oxidizer from the nose, m;
I = rocket's moment of inertia matrix, kgm^2;
w = angular velocity of the rocket rotation, rad/s;
$Beta$ = angular position of the rocket, rad;
$D\ core$ = diameter of the fuel grain, m.

Lastly, a short excerpt from the trajectory function with the lines where the aerodynamics coefficients are found using a model as a function of speed. Then, lift and drag forces are calculated with $L = \frac{1}{2}\rho_a v^2 c_l A$ and $D = \frac{1}{2}\rho_a v^2 c_d A$.
Projecting these forces on the axis perpendicular to the rocket one the normal force is evaluate.
At the end, the external moment is calculated adding the moment of the normal force wiht the one due to Jet Dumping.

```
% Model of atmosphere
[T_a,ro_a] = atmosphere4(y(4)/1000); % altitude input
v=(y(1)^2+y(2)^2)^0.5;
Ma = v/sqrt(gammaAir*R*T_a); % Mach number
if m_dot>0 % motor on or off
    r='on';
else
    r='off';
end
[cl, cd] = aero_coeff3(Ma,r,abs(alfa))   ;  % lift/drag coeff
D = 0.5*ro_a*v^2*cd*A_f;                    % Drag force
L = 0.5*ro_a*v^2*cl*A_f;                    % Lift force
S=(m_dot+m_dot_f)*Isp*g0;                                        % Thrust
Fn = L*cos(alfa)+D*sin(alfa);               % Normal aerodynamic force
JD=(m_dot+m_dot_f)*(Ltot-Lcg)*y(12);        % Jet Damping
Mext= -(Lcp-Lcg)*Fn-JD*(Ltot-Lcg);                       % Resultant moment
```

3.5 Results

Firstly, in this section, the results coming from the *MatLab* function `trajectory_3D_fun.m` are shown.

In the following figures 3.19, the `Altitude`, `Slant range` and `Mach number` resulting from the first trajectory iteration and from the last iteration are compared. The difference is given mainly by the different initial weight of the rocket, that in the first iteration is calculated as 136,4 kg and that after the structural pre-dimensioning it values 149,5 kg. Also the better approximation of the time-dependent variables as the total mass, the rocket inertia and the CG position does its part.

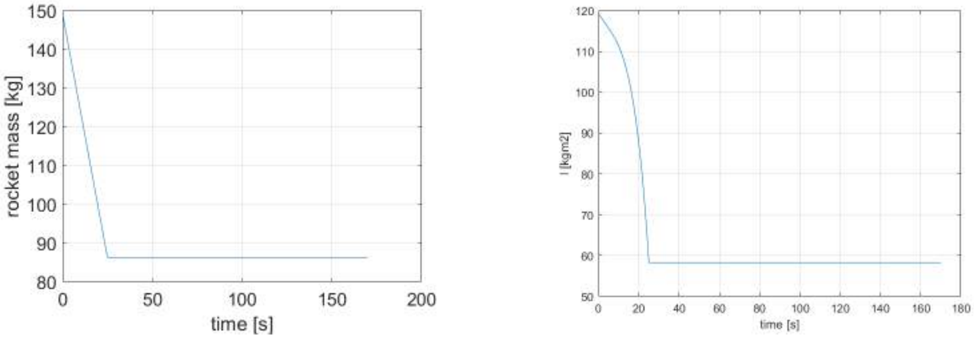

(a) Rocket mass variation (b) Rocket inertia variation

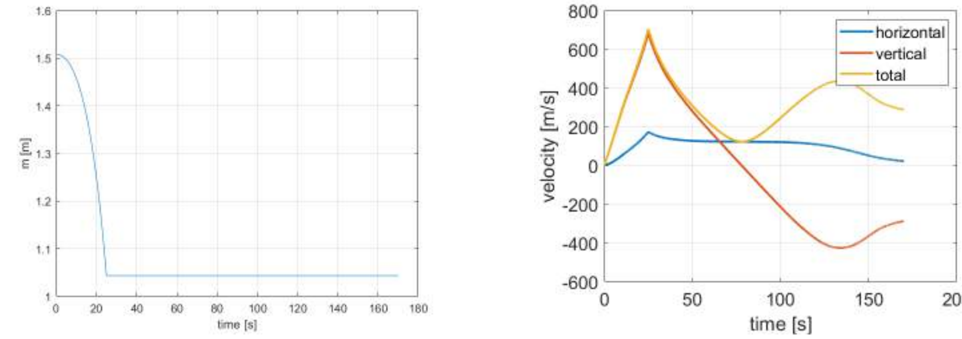

(c) Rocket CG variation from the nose (d) Rocket velocities during flight

Figure 3.18: Results from the last iteration.

The variation of these variables during the flight time is shown in figures 3.18.
As expected, the time interval where these properties change is exactly the burning time.

At the end, let's compare the result of the oxidizer tank structure preliminary desing.
The input data are:

MEOP	45 bar
Burst pressure	2 $MEOP$

The minimum thickness required to carry the loads, calculated using the netting analysis and the matlab script, based on the CLT, are:

Method	Thickness required [mm]	Weight, [kg]
Netting	1.25	4.40
CLT	3.00	1.84

The gap between the two results is significant, but expected. The maior contribution of this difference it is within the theories themselves, because the netting analysis hypothesizes that the load is carried only by the reinforcement fibers, that means that no attention is paid about the matrix failure when, for example, a single ply is stretched in the weakest direction, i.e. perpendicularly to the fibers. The only failure parameter considered by netting theory is the ultimate tensile strength of the reinforcements, while the `laminate` function implemented in *MatLab* calculates for each ply when the failure occurs, considering both directions.

That's why the netting analysis was really helpful in the beginning of the composite era, when the standard technology to manufacture composite pressure vessels were the fillament winding. With the presence of an internal liner the only aim of the carbon fibers was to strengthen the vessel resistance.

In our project, the goal is to use a linerless oxidizer tank, it means that the entire carbon composite vessel has to withstand the applied loads and prevents any possible leakage. For this reason we can not accept any matrix failure, even if this would not mean a failure of the structure.

Eventually, a minor contribution to this thickness difference is that during the netting analysis just the internal pressure load was considered.
In the *MatLab* script also the external loads due to the flight phase are added.

The oxidizer tank, in addition to being innovative because of the linerless characteristic, is also a structural component of the rocket structure.
A more detailed design phase is necessary, with the help of a CAD and FEM software.

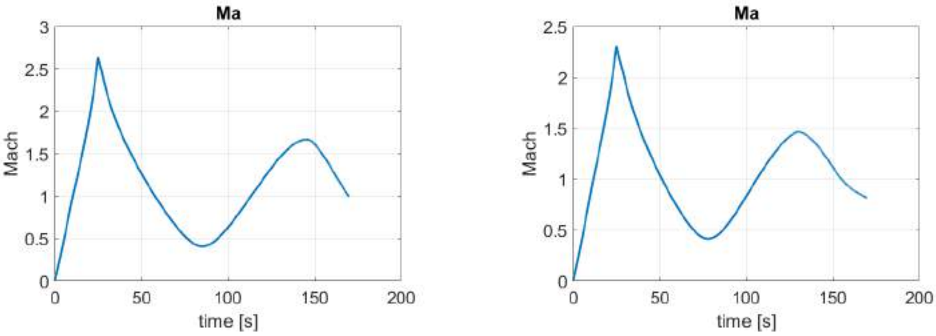

(a) Mach number (b) Mach number

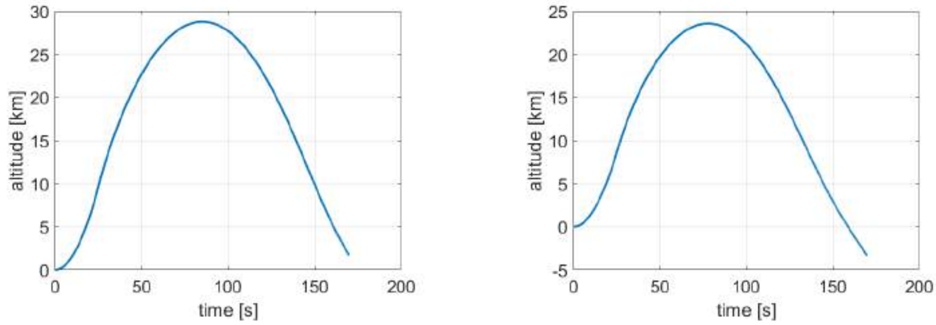

(c) Altitude (d) Altitude

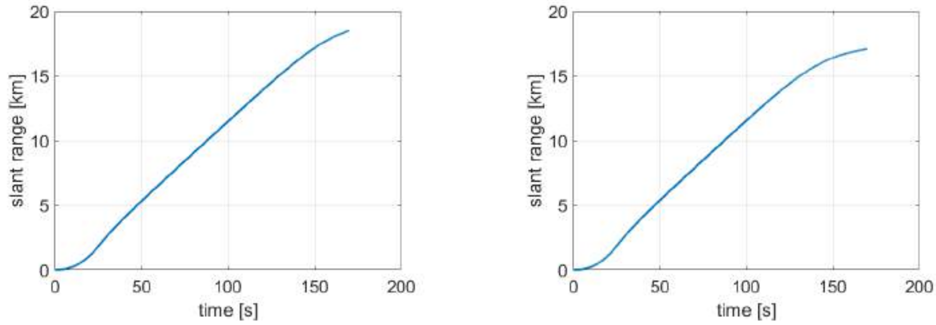

(e) Slant range (f) Slant range

Figure 3.19: Results comparison between the two iterations.

Chapter 4

Oxidizer Tank Design

As we said in previous chapters, in the space industry weight is a key factor, strictly correlated to money and performance. In the last decades, to obtain lighter space systems and parallel to the use of light metallic alloy, the CFRP composite materials have seen great growth. They offer really high strength to weight ratio, and the possibility to choose preferential directions where the mechanical properties will be higher than in other ones. The oxidizer tank of the rocket is a thin cylindrical shell structure where the loads are not equal in the directions, so the use of CFRP materials is ideal. Then, due to the compatibility between the epoxy resin and the oxidizer used, the development of a linerless composite tank has been chosen as a design objective. It represents the first attempt in the literature and a possible innovation for this kind of structure. That means the tank will not be manufactured using the filament winding technology. The process to realize the oxidizer tank are divided into two steps:

- First, the cylindrical thin shell is produced with the tubing wrap technique,
- Second, two end closures are manufactured using a dedicated mold.

After having cured the pieces in autoclave the two end closures will be bonded to the cylinder by an epoxy adhesive that will need a cure cycle in the oven.

To design these parts CAD and FE softwares were utilized. Due to the license agreements with the University of Padua the software used are:

- *SolidWorks Student Edition*, a parametric 3D CAD;
- *Rhinoceros*, a 3D CAD modeler;
- *ANSYS Workbench*, to perform FE analysis.

4.1 Requirements

The requirements for the oxidizer tank are:

- MEOP, maximum expected operating pressure, of 30 bar;
- Burst pressure is set to be at least 2*MEOP ;
- Structural axial load of 5000 N;
- Structural transversal load of 1000 N;
- Tank volume, it has to contain 60 kg of H_2O_2;
- Ullage volume, $V_{ull} = \frac{5}{100} V_{H_2O_2}$
- Internal diameter of 190 mm;
- Linerless, no failure in the composite admitted;

4.2 Finite Element Analysis

Finite element analysis is a numerical simulation technique used in structural application that allows to resolve complex structures in a simpler way.

The current development of technology has led to the creation of many numerical solvers with different capacities, for various types of analysis that can be performed. These allow the solution of innumerable problems, ranging from simple static to non-linear analysis, in which contact zones are also involved, up to dynamic analysis at high and low speeds. In the structural field, many solvers, in addition to performing accurate analysis on isotropic materials, have developed over time the ability to implement composite materials as well. The increasing use of these materials in the industrial sector required the development of dedicated software.[10]

For the analysis performed in this thesis, the software *ANSYS Workbench* is used, one of the most common commercial solvers on the market. Actually, *ANSYS Workbench* is a software environment for performing structural, thermal, and electromagnetic analyses. In this work the structural part will be used, focusing on ACP module, the one to perform analysis on composite structure.

Generally, the analysis process is divided in three steps:

1. Pre-process
2. Numerical solution
3. Post-process

In the pre-process one of the aims of the software is to calculate the stiffness matrix of the system to be analyzed.
Firstly it is necessary to define a geometry, in our case the geometry of the pieces are created in a CAD software and imported in the FE environment. Then it is possible to set the material, based on the type of analysis, the properties of the material introduced can be linear, non-linear, isotropic or orthotropic, and also dependent or independent of temperature.

An important choice to make is relative to the element type. The element type of our interest are `SHELL63` and `SOLID45`, they are, respectively, a 2-D element and a 3-D element. The first one is used to discretize every geometry where the thickness are really small compared to the other two dimensions. The solid element is used where these assumption is not valid anymore.

Once all the constituent parts of the structure to be simulated have been introduced, these must be discretized in order to to create a series of nodes in which the solutions will be calculated. This discretization is called mesh and can be realized with different conformations and dimensions based on the accuracy of the solution and the simulation times to be obtained. It will be up to the user to find the right compromise between these two parameters.

To complete the pre-process phase the boundary conditions and the loads should be set. The boundary conditions are the known values of the degrees of freedom of the body on his edges. In a structural analysis the degrees of freedom (DOF) consist essentially in displacements (3-DOF) and rotations (3-DOF), for a total of 6 DOF. An example is the fixed condition, where all the 6 DOF assume the value of zero.
The loads can be defined concentrated at some specific nodes or distributed over an edge or a surface, even though the solver will translate this distributed loads applying congruent loads on the involved nodes.

Once this phase is finished, the numerical solution process starts, the algebraic equations are solved through the use of the finite element method.

In the post-process phase the results got from the calculated solution are analyzed. These results are usually displayed and analyzed through a graphic interface, in which the model appears colored: each color contour is assigned a band of numerical values of tension or deformation, that allows to understand which are the most stressed areas and to proceed in the design.

4.2.1 FEM: Finite Element Method

Finite element analysis are based on the theory of displacements for the solution of continuous structures, which derives from the more complex theory of forces.
A real representation, in static conditions, of a body under the action of a load can be obtained by a differential equation. However, since its resolution is extremely complex or impossible to achieve in a closed form, the theory of displacements is used, that allows us to approximate the solution of a differential equation with that of an algebraic equation. This theory involves the discretization of the structure into elements, the forces are exchanged only between the nodes. This implies that each element must ensure balance on the nodes. Although in reality there are no nodal displacements, in the method described they are foreseen, so the necessary condition to reach the solution is to impose equilibrium and congruence on the nodes.[10]

The forces acting on each node are evaluated on the basis of Hooke's law:

$$P = k \cdot u \tag{4.1}$$

where

u = nodal displacement

k = material stiffness

As is known, Hooke's law is valid only in the linearity field of a material. As an example, lets consider a fixed beam, modeled with two mono-dimensional elements, figure 4.1. Each element has two nodes, so the structure obtained is formed by two elements and three nodes: one of the external nodes is constrained and, therefore, with zero displacement. The stiffness of the material is approximated by a spring element: thus Hooke's law applies to every node.

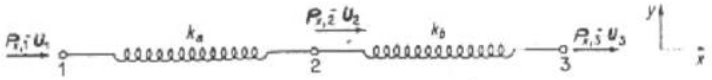

Figure 4.1: Beam discretization with 1-D elements.

By imposing the equilibrium on the nodes, a matrix system will be obtained in which the unknowns will result to be the nodal displacements, and whose solution will require the inversion of the stiffness matrix.

From the equilibrium at the nodes we get:

$$\begin{Bmatrix} P_1 \\ P_2 \\ P_3 \end{Bmatrix} = \begin{bmatrix} k_a & -k_a & 0 \\ -k_a & k_a + k_b & -k_b \\ 0 & -k_b & k_b \end{bmatrix} \begin{Bmatrix} u_1 \\ u_2 \\ u_3 \end{Bmatrix} \tag{4.2}$$

where

u_i = i-node displacement

k_a and k_b = element stiffness

P_i = forces acting on the elements at the i-node

A necessary condition for the inversion of the stiffness matrix, and therefore for obtaining the displacements, consists in the non-singularity of the matrix itself, obtainable with the imposition of a constraint in the structure.

Considering now a more common continuous structure, despite the principle is very similar to the one described, some other effects occur which complicate the calculation process.

First of all, in a continuous system it is necessary to consider the fixed reference system with respect to the local one; to take this into account a rotation matrix for each element is introduced, which identifies the position of the local reference system, with respect to the fixed one. In addition to the tensor state on the nodes, it is also necessary to define the tensions acting on the whole body. To do this, we use the shape functions that allow us to correlate the nodal displacements to the internal ones. These ensure congruence, but not the equilibrium of the tensions of the entire body. So, from the shape functions are derived the deformations for which only congruence is guaranteed.

If we assume that the state of congruent deformation is equivalent to the state of balanced and congruent deformation (ie the real state), and making use of the principle of virtual works, we obtain the approximate stiffness matrix of the whole body. Knowing the stiffness matrix it is possible to derive the approximate tensor state of the whole body. Therefore the determination of the stiffness matrix derives from the shape functions.

The hypothesis introduced is fundamental and is the basis of the displacement method, which allows to obtain results that closely approximate the real case. From the above, it is clear that it is important to define in the best way the dicretization of the body, that is to define the right amount of elements in which to divide the structure. In fact, the more the elements are small, the greater the number of total nodes possessed by the entire body: the numerical solver will have to perform the calculations on each single node and, therefore, the complexity of calculating the problem will increase. It will be the ability of the user to obtain a good compromise between resolution of discretization and computational complexity.

4.3 Carbon Fiber Properties

At this stage, it was possible to improve our analysis by knowing exactly which type of carbon fiber would be available for the production of the parts.

The definition of the mechanical properties of the carbon composite plies always represents a tricky choice, in the literature there are not much data about, because generally they are worth money and know-how. A good way to proceed is to experiment and test a series of specimens made by the material of interests, with a different number of plies and stacking sequence, to create an internal database. That permits to improve the accuracy of the numerical simulation, as having a better material model, as having experimental results to compare with.

For our purpose and resources, the few data founded in the literature were compared firstly with the fiber data given by the producer of the carbon fiber and then with the ones present in *ANSYS* library.
The mechanical properties of the plies used in the numerical simulations are summarized in table 4.1.

	UD T700	Fabric T300
E_1 GPa	132.0	75
E_2 GPa	10.0	75
G_{12} GPa	6.5	6
τ_{12}	0.28	0.1
X_t MPa	1800	550
X_c MPa	1050	425
Y_t MPa	45	550
Y_c MPa	132	425
S MPa	69	60

Table 4.1: Carbon fiber ply properties.

The ply's thickness available are:

Fiber	Area density [g/m^2]	Thickness [mm]
UD T700	200	0.21
	300	0.315
BIAX T700	200	0.22
	300	0.33
Fabric T300	200	0.23
	630	0.68

Table 4.2: Available thickness for the plies.

Bi-axial fibres have two layers orientated at +45/-45 [deg] bound together using polyester stitching yarns. This type of fabrics are useful to overcome possible limitation due to the carbon roll height, or rather if the desired orientation is 45° and the roll is a unidirectional 0° the cut will be inclined, so the maximum ply length will be Roll Height $\dot{c}$os45.

4.4 Cylinder tank design

To design the tube of the oxidizer tank means basically to choose the lay-up of the carbon plies that will be wrapped around an aluminum cylinder in order to obtain the desired piece. Before to perform any FE analysis it is important to define some additional constraints for the lay-up sequence. The laminate lay-up has to be symmetric and balanced, this means that there is no coupling between extension and bending action. Thus, the applied stresses will produce only in-plane and shear strains and it will not produce any curvatures. Then, for the external and internal plies has to be used a T300 woven fabrics, this means having a directionally stable cross-ply as ending ply and an internal ply, where bonding area will be, that can offer a good resistance in axial and tangential directions. After these assumptions, we can start the investigation with the FE analysis, to find out the optimal lay-up of the carbon fiber plies.

The tank length to contain the required amount of oxidizer is:

$$V_{H_2O_2} = \frac{m_{H_2O_2}}{\rho_{H_2O_2}} = \frac{60}{1390} = 0.04317 \text{ m}^3 = 43.2 \text{ L}$$

$$A_{tank} = \pi \frac{0.19^2}{4}, \text{ m}^2$$

$$L_{tank} = \frac{V_{H_2O_2}+V_{ull}}{A_{tank}} = \frac{1.05 V_{H_2O_2}}{A_{tank}} = 1600 \text{ mm}$$

Actually, this is just the length of the tube cylinder that contains a volume equals to $V_{H_2O_2} + V_{ull}$. Lets suppose that the tank has two spherical end closures, that give a 'volume contribution' of $V_{sphere} = \frac{4}{3}\pi r^3 = 3.6\ L$, so the first iteration L_{tank} is equal to 1475 mm.

The cylindrical model with spherical end closures used to perform the first analysis is shown in figure 4.2, from ACP module:

Figure 4.2: First analyzed tank model.

In the same figure it is represented the thickness of the lay-up set in the software in that occasion, that was 2,91 mm for the cylinder tube and 5,4 mm for the spherical dome.

To reach the desired stacking sequence for the tank tube the process has been divided in two steps:

1. The focus of the first step was to find out a range of thicknesses that let our tank to operate at the MEOP without any failure and that will present a Reserve Factor (RF) greater than 1.5 at the defined Burst Pressure;
2. The aim of the second step is to optimize the lay up stacking due to the fact of having received information regarding the carbon plies available by the manufacturer. This lay up optimization had to satisfy the previous conditions with $RF > 1$ and maximize the stiffness in the rocket's axis direction.

In each analysis, the end closure thickness has been kept constant at 5,4 mm.

As said, in the first numerical simulations the mechanical ply's data were not available yet, for this reason the choice to Reserve Factor to be greater than 1.5.

The carbon plies considered wer the T300 wowen fabric and the unidirectional and biaxial T700 fabric.

To set up the numerical simulation were applied these boundary conditions and loads (figure 4.3):

- Symmetry condition at the middle plane of the tank structure, it permits to study the behaviour of the entire structure using half elements number;
- Fix the DOF left free from the symmetric condition to make the model solvable, a node on the top of the spherical dome has been chosen;
- A pressure load of 60 bar over the internal area is applied.

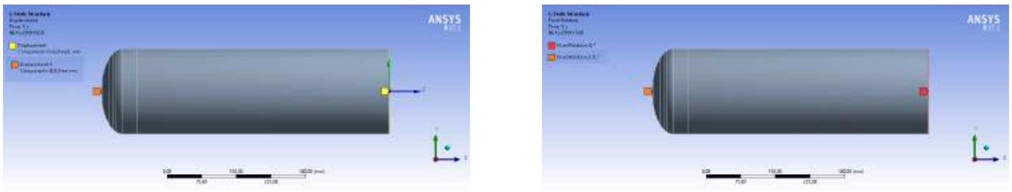

(a) BC on displacements. (b) BC on rotations.

Figure 4.3: Boundary conditions for the FE analysis.

The results of the first investigations are listed in table 4.3.

	Stacking sequence	Thickness, [mm]	Reserve Factor
1	$[W0/UD90_2/Bx45/\ \overline{Bx0}]_S$	2.66	1.35
2	$[W0/UD90_2/Bx45_2/\ \overline{Bx0}]_S$	2.91	1.75
3	$[W0/UD90_2/Bx45/UD0/\ \overline{UD90}]_S$	2.79	1.45
4	$[W0/UD90_2/Bx45/Bx0/\ \overline{Bx45}]_S$	2.91	1.5

Table 4.3: RF and stacking sequence of first analysis.

The stacking sequence number 4 was chosen as first reference, and the RF plot is shown in figure 4.4. The value for the cylinder tank is between [1.5, 1.75], that is acceptable because the simulation was carried out under a pressure load of 60 bar.

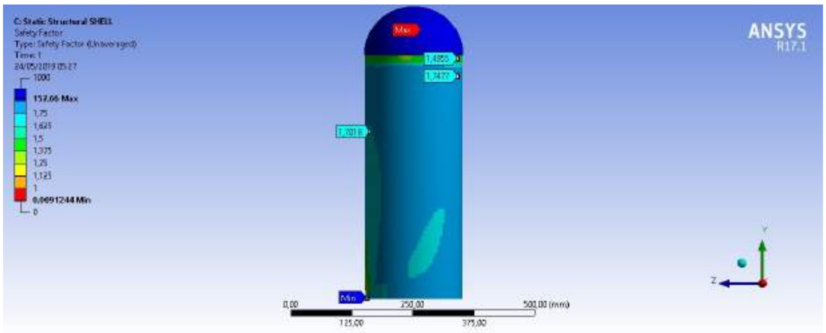

Figure 4.4: RF plot.

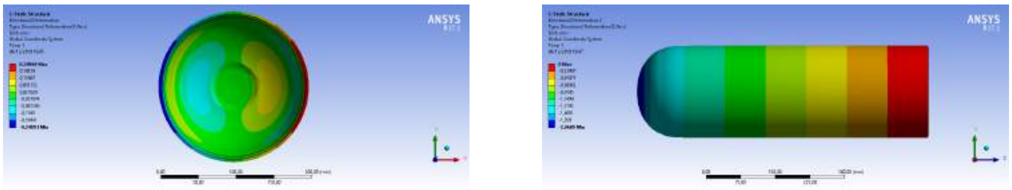

(a) Circumferential deformation.

(b) Longitudinal elongation.

Figure 4.5: Result of the analysis of the lay-up number 4.

Images of the circumferential deformation and longitudinal elongation are shown in figure 4.5.

The second design step began when the information on the weights of the available plies was obtained (exposed in section 4.3). Moreover, at that time, some requests from the structural group were received, that is to stiffen the structure along the rocket axis to improve global structural stability.

In order to achieve the desired results, the stacking sequence number 4 was taking into consideration and from it we have gradually increased the percentage of fibers in 0° direction, i.e. the one parallel to the axis of the rocket. Proceeding in this way, while the fibers in 0° direction gradually increased, the reserve factor decrease, as a consequence of the diminution of the hoop fibers, the direction where the internal pressure load most solicits the tank structure.

Another aspect considered is how the final piece is produced, as already mentioned, the tube wrapping technique will be the technology used. All the plies rolled on the mandrel during the tube wrapping present a discontinuity where the open edges match on the cylindrical surface. For layers with a

different orientation from the one parallel to the axis of axial symmetry of the rocket, this discontinuity causes an interruption of the fibers, and therefore a point of weakness. To not present this gap in the load paths and to allow the transfer of the same through the two sides that match it is necessary to create an overlap. Generally, when possible, an overlap of about 30 mm is sufficient to give continuity and transfer the loads from the fibers of a ply to the adjacent one.
It is clear that an overlap causes a local increase in thickness (equal to the thickness of the overlapped fiber), which must be taken into account in order to avoid incurring unwanted thickening.

To try to keep the thickness close to the starting values (lay-up 4 of the first step) and to make it as uniform as possible along the circumference, proceed as follows:

- a ply from the lay up sequence number 4 is removed, so it compensates for the extra thickness due to the overlaps;
- an overlap length equal to the circumference divided by the number of skins is used.

The laminate sequences analyzed are shown in the table 4.4. For all the lay-ups the first (and the last) ply are the same, `Wowen T300`, as for the middle ply `Biaxial T700`, and the total thickness is 2,68 mm + 0,23 mm (average).
All the sequences are anti-symmetrical. In the table we wanted to highlight the intermediates plies, where we see, gradually, the increase of the fibers in longitudinal direction and the decreases of the hoop fibers.

The results obtained are shown in the table 4.5 and in figures 4.6. The engineering constants and the $\sigma_{ax,u}$ are calculated considering the hypothesis of homogeneous lamina, they can be considered as useful indicators for the comparison. In all the analysis, with the internal pressure as a load, the first ply failure occurs in the 0° fibers, caused by the reaching of the perpendicular strain limit, i.e., the circumferential deformation limit, that is dependant by the hoop fibers quantity.
While, for the calculus of $\sigma_{ax,u}$, the first failure occurs in the hoop fibers.

Ply	Ply's type	Lay-up A		Lay-up B		Lay-up C		Lay-up D	
		t, [mm]	θ	t, [mm]	θ	t, [mm]	θ	t, [mm]	θ
1	Wowen T300	0.23	0°	0.23	0°	0.23	0°	0.23	0°
2	UD T700	0.21	90°	0.21	90°	0.21	90°	0.21	90°
3	UD T700	0.21	90°	0.21	90°	0.315	90°	0.21	90°
4	UD T700	0.315	90°	0.21	90°	0.21	0°	0.315	0°
5	UD T700	0.21	0°	0.315	0°	0.21	0°	0.21	0°
6	Bx T700	0.33	45°	0.33	45°	0.33	45°	0.33	45°

Table 4.4: Stacking sequences of the last numerical investigations.

	E_1, [GPa]	E_2, [GPa]	G_{12}, [GPa]	ν_{12}	$\sigma_{1,u}$, [MPa]	RF
Lay-up A	44,2	91,7	9,84	0,076	141	1,33
Lay-up B	53,7	82,3	9,84	0,085	172	1,27
Lay-up C	63,3	72,8	9,84	0,096	202	1,15
Lay-up D	72,80	63,3	9,84	0,11	232	0,95

Table 4.5: Results from the analysis of the 4 lay-up.

The best compromise between total thickness, RF value, equivalent stiffness and equivalent resistance in the longitudinal direction is the lay up C.

Finally, for the lay up chosen, the rolling pattern is shown (figure 4.7, which shows (in section) the trend of each individual ply and the necessary overlaps.

A final numerical analysis was made to complete the design of the cylinder tube. Each overlap area presents in the chosen lay-up has been modeled in the ACP software. The aim of this last analysis was to investigate how much 'symmetry' we will lose in the tank deformed shape and if it could be a potential problem for structural strength.

In figure 4.8, it is possible to see the circumferential deformation at the middle plane. As expected it is not symmetrical anymore, due to the different overlap area. Anyway, the difference still remains small and acceptable.
The RF factors decreases slightly, remaining however greater than one.

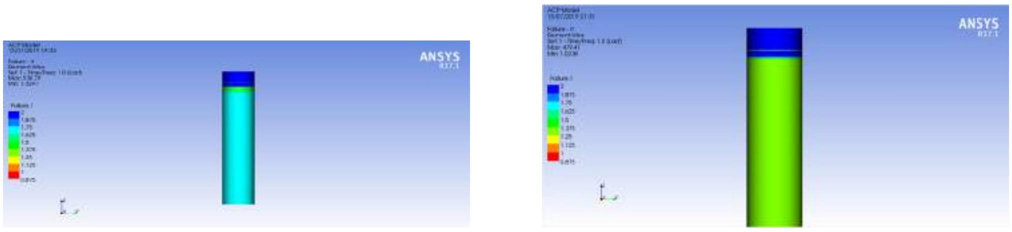

(a) RF of lay-up A (b) RF of lay-up B

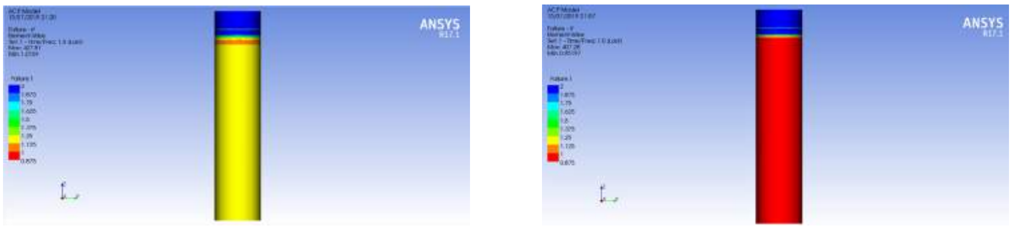

(c) RF of lay-up C (d) RF of lay-up D

Figure 4.6: RF plots for the four lay-ups analyzed.

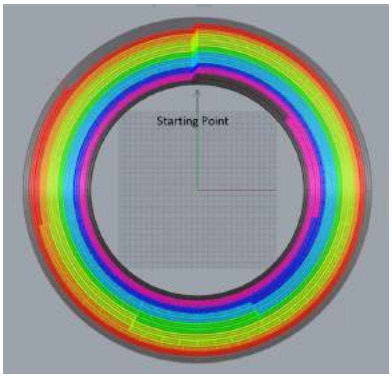

Figure 4.7: Lay-up section of the plies over the mandrel.

4.5 End-closures Design

To close the cylinder tube at its ends two domes have been designed.
The end-closures consist of a carbon fiber dome with a steel insert at the center.

The steel insert has an axisymmetric shape. In the middle has a 1/2 G internal threaded hole. The flower-shape collar is needed to increase the adhesion area with the epoxy resin of the pre-preg carbon fibers and to increase the torsion strength of the insert when it will be handled; the thickness of 2,2 mm is chosen to keep the stress under the steel yielding shear stress. To

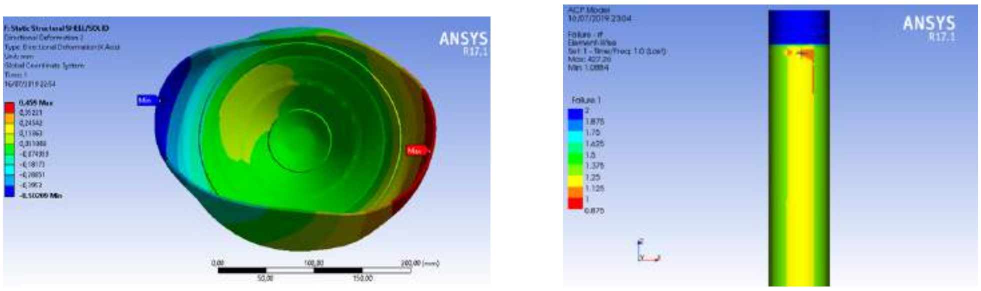

(a) Circumferential deformation.

(b) Reserve Factors

Figure 4.8: Result of the analysis with the overlap area modeled.

let the user to fasten a connector using a wrench tool, two seats are machining on the top of the insert. On the bottom, it presents 4 internal threaded holes, M3 size, to fix the anti-vortex structure, only at the dome where the oxidizer flow out.
The steel material was selected firstly for its compatibility with the oxidizer used, and also for its excellence strength to avoid any wreck of the internal thread.

A 3D view of the steel insert and a technical drawing are shown, respectively, in figures 4.9 and 4.10.

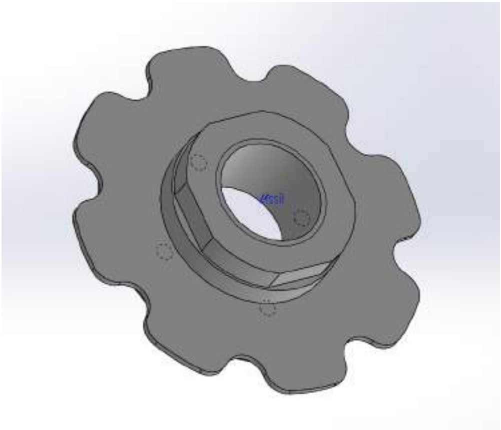

Figure 4.9: 3D view of the steel insert. From the top.

Regarding the domes, due to the curvature surfaces, to the greater thickness in some area and also due to the loads that not have a preferential path, the material considered for the manufacture is the fabric woven T300.

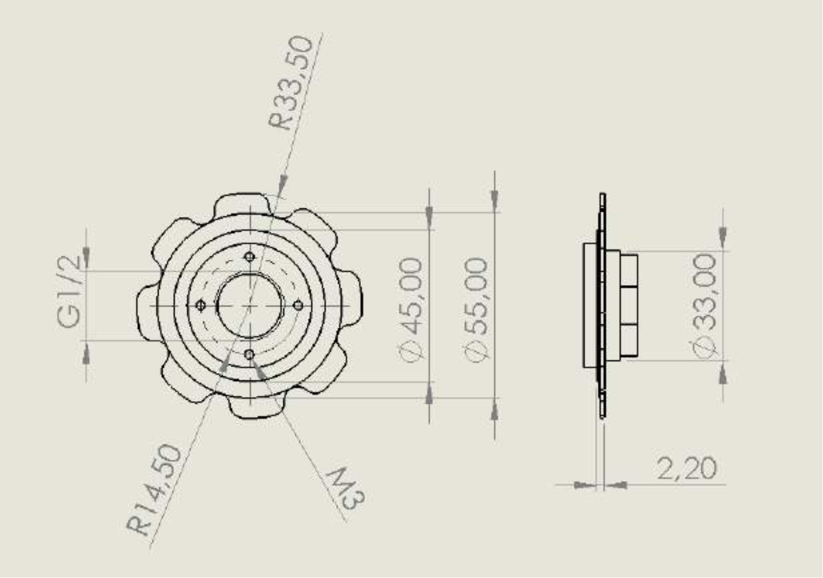

Figure 4.10: Technical drawing of the steel insert.

For this part the orientation does not represent a real design driver for two reason:

1. The higher the number of plies stacked together with different orientation, the less the composite material suffer the coupling terms introduced in section 3.1.3, even without using a special layup type;
2. The difficult to find a preferential loads paths and the difficult to manually stack up a desired orientation during the manufacturing.

A design driver for the end closures design is the thickness variation along the section, due to the curvature geometry and the opening hole (where the steel insert will be positioned).

Another important parameter is the dome shape.
The two constraints are where the curvature develops are:

- externally the junction with the small cylindrical part where the dome will be bonded to the tank tube;
- internally, the curvature doesn't get until the opening hole because around it it is indispensable that the dome surface would be parallel to

the "flower" shape insert collar. This condition is dictated by manufacturing needs, doing in this way the "pressure" that the steel insert will made over the dome during the cure process is uniform, avoiding any discontinuity spot that can cause leakage. So, the curvature internal limit is the collar radius of the steel insert.

To join the two boundaries the initial idea was to maximize the internal volume of the dome or to use an elliptical curve. After a research in the literature, as suggested by ECSS documents, pressure vessels domes have generally a torispherical shape. A torispherical dome is the surface obtained from the intersection of a spherical cap with a tangent torus. In the image 4.11 is possible to see the file used to create several different torispherical shapes. The figure 4.12 compares them to the elliptical curvature (in green the elliptical dome and in red the steel insert).

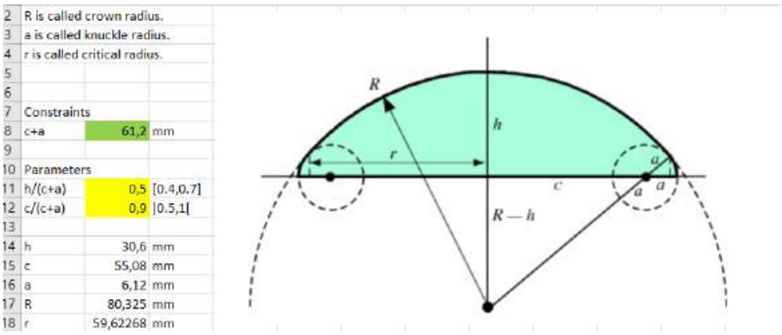

2	R is called crown radius.		
3	a is called knuckle radius.		
4	r is called critical radius.		
5			
6			
7	Constraints		
8	c+a	61,2	mm
9			
10	Parameters		
11	h/(c+a)	0,5	[0.4,0.7]
12	c/(c+a)	0,9	[0.5,1[
13			
14	h	30,6	mm
15	c	55,08	mm
16	a	6,12	mm
17	R	80,325	mm
18	r	59,62268	mm

Figure 4.11: Excel file that calculates the parameters to draw a torispherical dome.

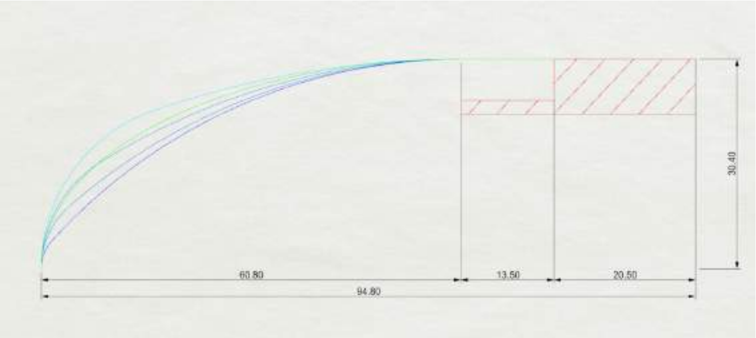

Figure 4.12: Comparison between torispherical and elliptical shapes

For the structural study of the dome, a more complex analysis is necessary, due to the presence of different materials and to the thickness of the dome, that in the top end it reaches high values.
The model created in Ansys workbench is visible in the figure 4.13, where:

- The modules A,B and C are, respectively, the geometries of the tank tube, the end-closure and the steel insert;
- The module C also create a mesh of the insert with solid elements;
- The module D is an ACP module, it define the lay-up of the tank tube with a given stacking sequence and create the mesh using shell elements, the tank is considered as thin shell composite structure;
- The module E is an ACP module, it define the lay-up of the end-closure with a given stacking sequence and create the mesh using solid elements, the dome is considered as thick shell composite structure.
- The module F is the solver, after have defined the bonded areas, the boundary conditions and the loads it resolves the numerical problem, it also shows some results.
- The modules G and H are dedicated ACP post process modules that permit a deeper investigation of the results obtained on the composite structures.

Resuming, the tank is considered as a thin shell composite structure, the steel insert as a solid model and the end-closure as a thick shell composite structures. The 3 meshes are generated separately, then they are merged in a unique static structural simulation.

In the images below (4.14) are shown the two contact area, the first one between the dome and the steel insert and the second one between the end-closure and the tank shell. This is called bond area because during the manufacturing the two pieces will be bonded using an epoxy adhesive.

To calculate the length of this cylindrical section is used the equation :

$$L_B = \frac{F_{axial} SF}{\tau_{adh}} \tag{4.3}$$

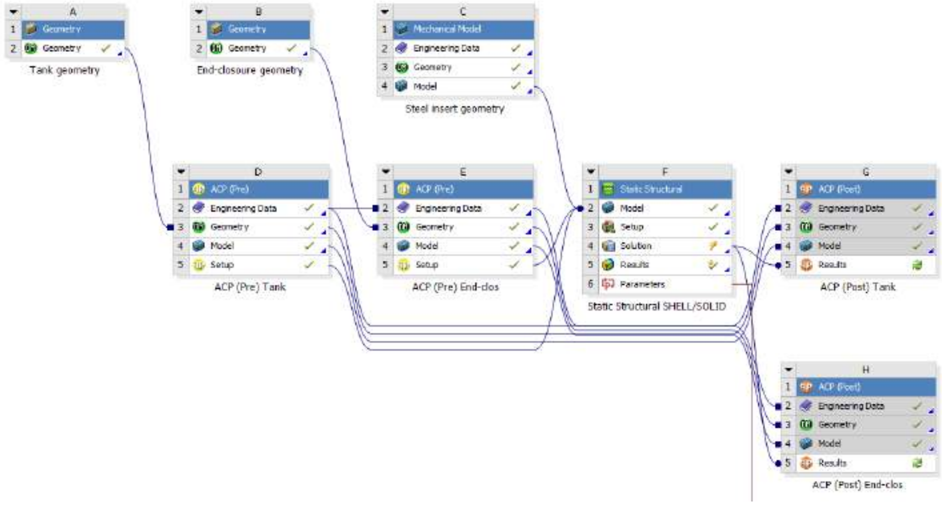

Figure 4.13: Ansys Workbench model.

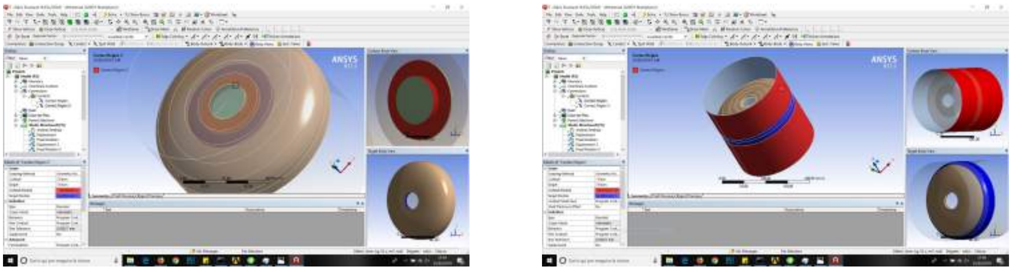

(a) Between the dome and the insert. (b) Between the dome and the tank.

Figure 4.14: Contact areas created by the solver.

with:

$$\tau_{adh} = 27\,\text{MPa};$$
$$SF = 2;$$
$$F_{axial} = (2\text{MEOP})\phi_{in}/4;$$

results:

$$L_B = 25\,\text{mm}$$

As was done for the tank design, the design process has been divided in two steps:

1. An elliptical dome shape is considered, the aim is to find a lay-up that satisfy all the requirements with no failure;

2. The torispherical domes are compared with the elliptical one and the lay-up will be optimized.

After first iterations the resulting lay-up is shown in figure 4.15, in the 3D model and in a plane section of it. It is possible to recognize the empty space in the plane section where the steel insert is positioned. The thickness varies along the dome, increasing in the area where the pressure load are perpendicular to the plies, causing a bending stress. In the bond area the fibers are oriented parallel to the solicitation, so a thin thickness is sufficient to outstand it. The thickness where the curvature begin has been noticed that is quite important, not for the local failure, but for the total deformation of the dome and consequently, for the stress produced on the bond area.

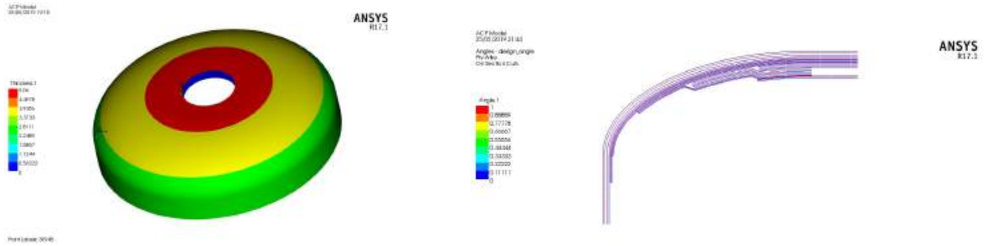

(a) 3D model. (b) Section plane of the model.

Figure 4.15: Dome layup after first design phase.

The deformation in the longitudinal and transversal directions, with the safety factor plot, are shown in the figures 4.16.

To continue in the second design phase, where the comparison between the different shapes and the optimization of the layup will occur, the surface of hte dome's geometry where divided in a similar way, to have a feasible confrontation between the results and between the weights.

This surface division are visible in figure 4.17, it consists in:

- Bond-top area, a ply that covers the bond area and all the end-closure surface;
- Top-1,2,3 areas, a ply that covers a portion of the end-closure surface;
- Middle, plies that are adjacent to the steel insert;
- Final area, the ply that covers, internally, the dome surface.

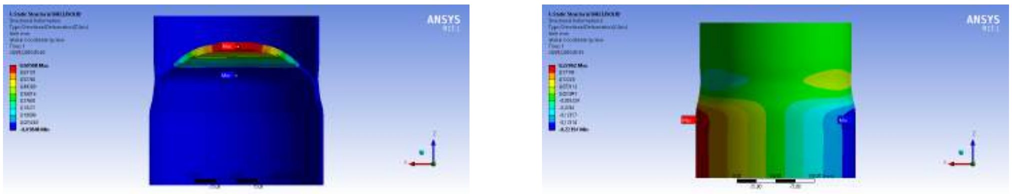

(a) Longitudinal deformation. (b) Transversal deformation.

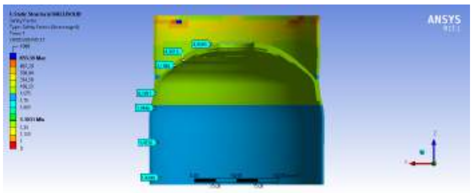

(c) Safety factors plot.

Figure 4.16: Results from the first design phase.

The value of the area of each division are listed in the table 4.6:

	Ellipse	TS 06	TS 07	TS 08	TS 09
bond-top, [mm^2]	46502,83	47638,29	46422,76	45519,78	44832,78
top-1, [mm^2]	24316,31	23851,67	24118,74	24650,61	25060,9
top-2, [mm^2]	14787,71	14696,83	14854,42	14965,27	15044,8
top-3, [mm^2]	6950,36	6946,95	6957,14	6963,93	6968,63
middle, [mm^2]	12117,36	12026,48	12184,07	12294,92	12374,45
final, [mm^2]	36684,73	37820,19	36604,66	35701,68	35014,68
Total, [mm^2]	34589,91	35725,37	34509,84	33606,86	32919,86

Table 4.6: Areas value of the surface division for each dome shape.

The TS end-closure indicates a torispherical shape where, with reference at the figure 4.11, were calculated varying the second parameter of the *Excel* sheet within the interval [0.6-0.9].

Actually, comparison and layup optimization have been done in parallel. The first two geometries to be compared where the elliptical and the TS-09. The first layup chosen (for the optimization) was really light, the intention was to begin with a SF below one. Each stacking sequence in this paragraph refers to the surface division, so a [8,2,4,6,9,3] layup means:

(a) Bond-top. (b) Top-1.

(c) Top-2. (d) Top-3.

(e) Middle. (f) Final.

Figure 4.17: Dome's surface division.

	Number of plies
bond-top	8
top-1	2
top-2	4
top-3	6
middle	9
final	3

The results of this first comparison are shown in figures 4.18 and listed in the table 4.7.

	Weight, [g]	Def long, [mm]	Def trans, [mm]	SF
Ellipse	281	2,84	0,3	0,42
TS 09	276	1,65	0,2	0,62

Table 4.7: Results from the first comparison.

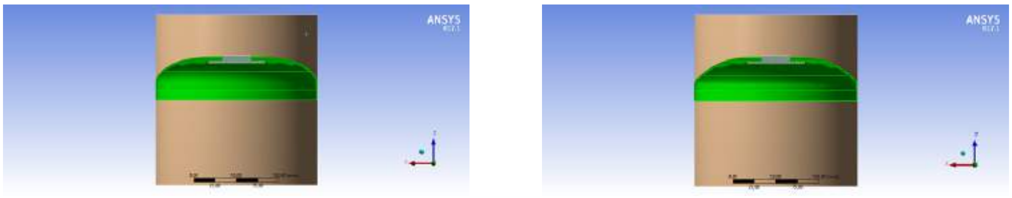

(a) Elliptical geometry. (b) TS-09 geometry

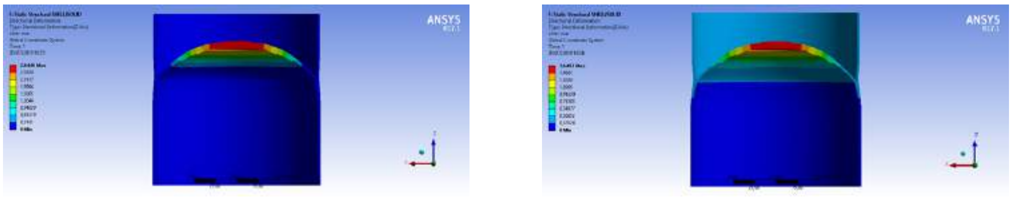

(c) Longitudinal deformation, ellipse. (d) Longitudinal deformation, TS 09.

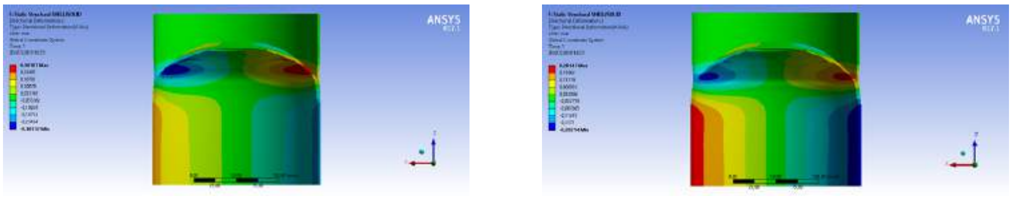

(e) Transversal deformation, ellipse. (f) Transversal deformation, TS 09.

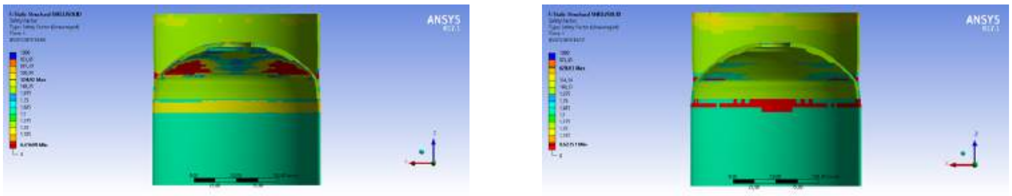

(g) Safety factor, ellipse. (h) Safety factor, TS 09.

Figure 4.18: Comparison between the elliptical dome geometry and the TS-09 one.

As expected, with this layup the end-closure will fail under the internal pressure load. But interesting is to see that the torispherical dome TS-09 performs better than the elliptical one, moreover it is also lighter. The elliptical dome undergoes to a greater total deformation, for that reason the SF are smaller. At this point, the TS-09 will be take as reference. For the subsequent confrontation it will be compared to the thorisperical dome TS-06. The two intermediate ones (TS-07 and TS-08) are really similar to the elliptical one, we want to see what happen on the other "side".
The new layup analyzed is [10,4,2,4,9,3], to try to reinforce globally the end-closure.

As before, the results of this second comparison are shown in figures 4.19 and listed in the table 4.8.

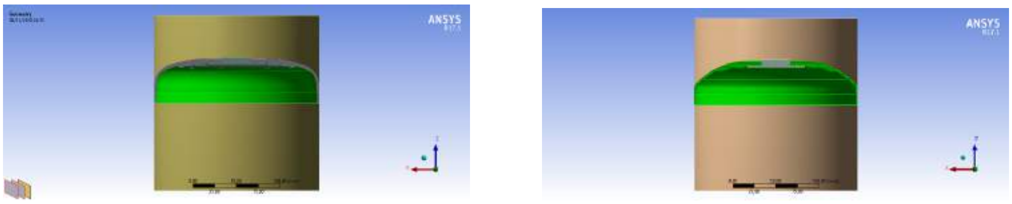

(a) TS-06 geometry. (b) TS-09 geometry

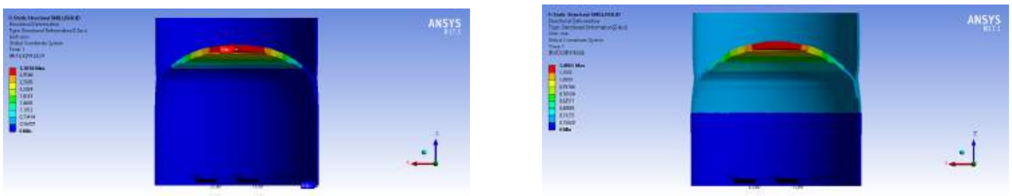

(c) Longitudinal deformation, TS-06. (d) Longitudinal deformation, TS 09.

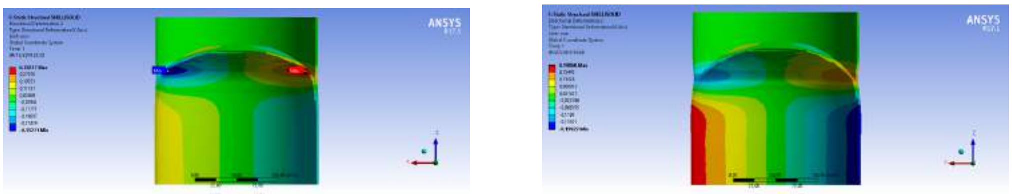

(e) Transversal deformation, TS-06. (f) Transversal deformation, TS 09.

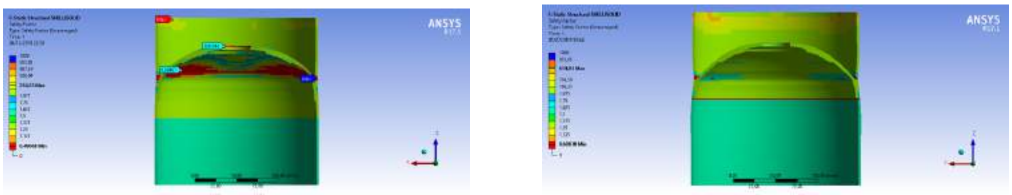

(g) Safety factor, TS-06. (h) Safety factor, TS 09.

Figure 4.19: Comparison between the TS-06 and TS-09 dome geometries.

Surprisingly, the TS-09 torispherical dome performs much better than its 'mate', being lighter. The total deformation is lower than the one experienced by the TS-06 dome, anyway the SF value still not satisfy the requirements. Other analysis have been run, changing the stacking sequence to find out the best compromise between weight and safety factor.

After the firsts two iterations the TS-09 shape are chosen as the final shape for the end-closure to be designed.

At the end of this series of simulation, the layup that better performed is the number 7. It ensures a good value for the safety factor without being the

	Weight, [g]	Def long, [mm]	Def trans, [mm]	SF
TS 09	312	1,40	0.20	0,60
TS 06	322	3,30	0,35	0,49

Table 4.8: Results from the second comparison.

	Stacking sequence	Weight, [g]	Safety Factor
1	[6,2,4,4,4,10,3]	339	0.76
2	[6,2,4,4,4,10,4]	352	0.81
3	[6,2,6,4,2,10,3]	349	0.84
4	[6,2,6,4,2,10,4]	362	0.90
5	[6,2,8,4,0,10,4]	372	0.96
6	[6,2,10,2,0,10,3]	376	1.02
7	[6,4,10,0,0,10,3]	371	1.06
8	[6,6,8,0,0,10,3]	374	1.03
9	[6,2,12,0,0,10,3]	367	0.99

Table 4.9: Layup optimization for the TS-09 shape.

heavier solution. Also the layup number 9 gave an interesting result, with a deeper analysis and after some experimental data could represent a good direction to follow to obtain a lighter piece. The chosen layup is visible in the figures 4.20.

To conclude the end-closure design two more simulation have done. One has included the tank tube with the overlaps, and one have included the adhesive layer in the bond area. The results of these latest analysis are shown in figures 4.21 and listed in the table 4.10.

	Def long, [mm]	Def trans, [mm]	SF
With adhesive layer	1,11	0.27	1.10
With the tube overlap	0.46	0,50	1.08

Table 4.10: Results from the second comparison.

The presence of the adhesive layer does not change the situation from the previous investigation, instead of the overlap tank tube, its no-symmetrical circumferential deformation halves the longitudinal elongation, while increases

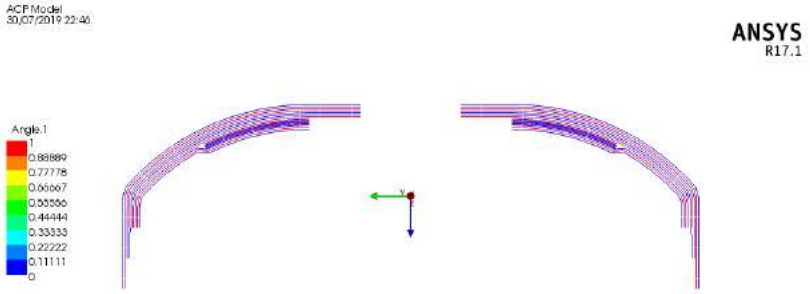

Figure 4.20: Lay-up scheme for the end-closure

the total transversal deformation, as expected. The intent was to verify that the overlap tube does not worsen the safety factor value, and that the stresses experienced by the adhesive were acceptable, as reported in table 4.11.

	FE analysis value	Reference Value
Shear stress, [MPa]	18	27
Peel stress, [MPa]	15	38

Table 4.11: Results from the second comparison.

A 3D plane section of the final geometry of the end-closure is shown in the figure 4.22.

4.6 Tank assembly

In this section are reported the geometrical characteristic of the oxidizer tank assembly.

The internal volume of the end-closure measures 1,28 L, while the total internal volume required in the tank is 43,2 L + 2,15 L.
This means that the domes are collocated at distance of 1510 mm.
The weights of the parts and of the assembly are reported in the table 4.12.

A section plane of the oxidizer tank assembly, with an overall view of the tank inserts in the fluidic system and a drawing of it are shown in the figures 4.23.

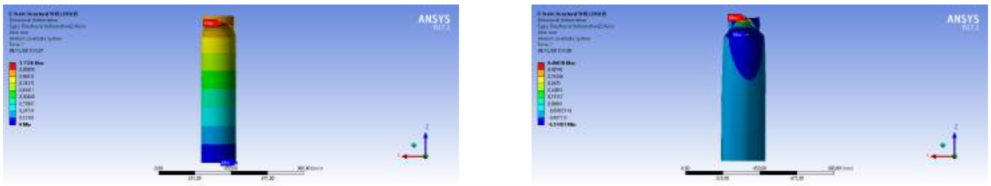

(a) Longitudinal deformation, adhesive layer.

(b) Longitudinal deformation, tube overlap.

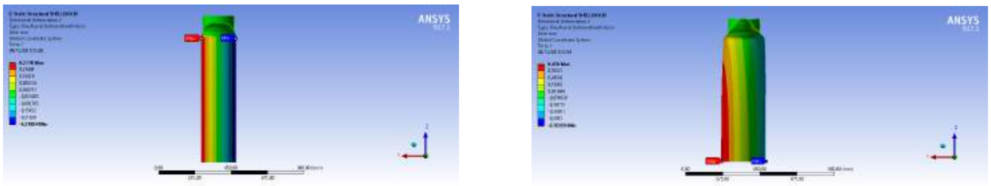

(c) Transversal deformation, adhesive layer.

(d) Transversal deformation, tube overlap.

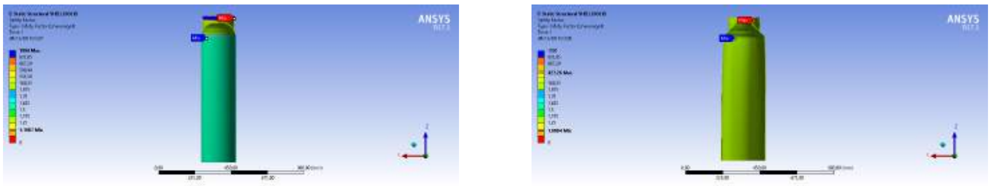

(e) Safety factor, adhesive layer.

(f) Safety factor, tube overlap.

Figure 4.21: Results of the last analysis.

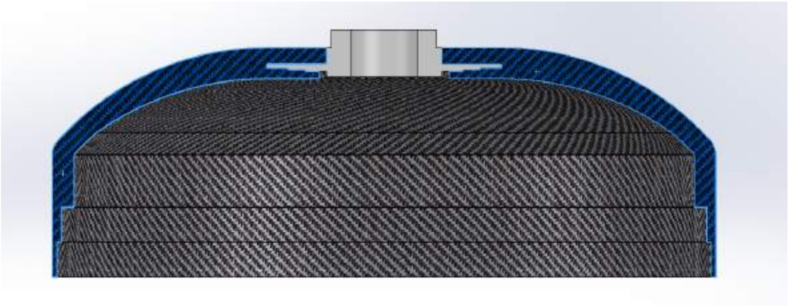

Figure 4.22: 3D plane section of the end-closure.

Part	Part weight, [g]	Number of parts	Weight, [g]
End-closure	440	2	880
Steel insert	90	2	180
Anti-vortex	100	1	100
Tank tube	15	1	4260
Total			5420

Table 4.12: Weight of the oxidizer tank parts.

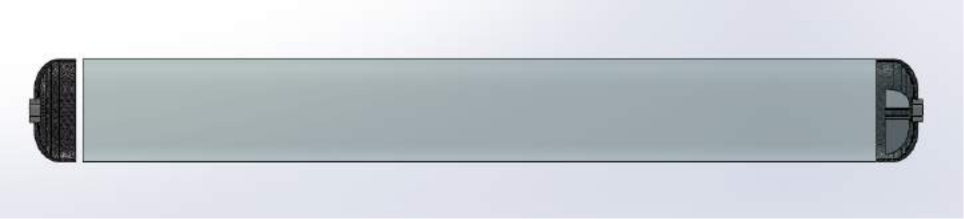

(a) Section plane of the oxidizer tank.

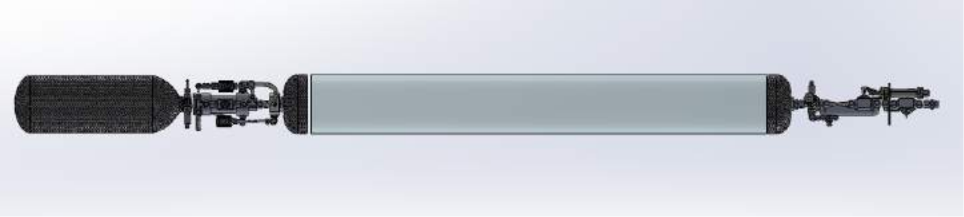

(b) Overall view of the fluidic line.

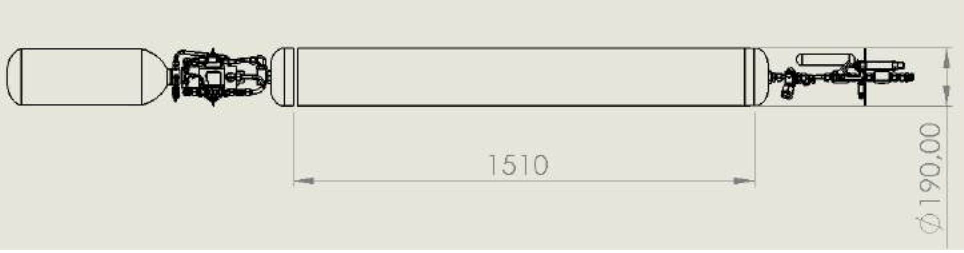

(c) Drawing of the fluidic line.

Figure 4.23: CAD view of the designed parts.

Chapter 5

Conclusions

During the preliminary design phase, the minimum thickness required for the tank structure to carry the loads was calculated:

Method	Thickness required $[mm]$	Weight $[kg]$
Netting	1.25	1.84
CLT	3.00	4.40
FE design	2.91	4.26

The gap between the thicknesses derives from two distinct contribution. The predominant one is the difference within the theories themselves, because the netting analysis hypothesizes that the load is carried only by the reinforcement fibers, that means no attention is paid about a possible matrix failure when, for example, a single ply is stretched in the weakest direction, i.e. perpendicularly to the fibers. The only failure parameter considered by netting theory is the ultimate tensile strength of the reinforcements. The CLT, instead, considers both directions, calculating the failure conditions at the lamina level for each ply. Even in failure models that not differentiate between reinforcement and matrix failures, the fact that the ply has a lower ultimate strength in the direction perpendicular to the fibers allows the CLT to partly describe the phenomenon, foreseeing a possible disruption. That's why the netting analysis was really helpful in the beginning of the composite era, when the standard technology to manufacture composite pressure vessels were the fillament winding, with the presence of an internal liner the only

aim of the carbon fibers was to strengthen the vessel resistance.
Eventually, a minor contribution to these thickness differences is that during the netting analysis just the internal pressure load was considered, conversely, in the *MatLab* script, also the external loads due to the flight phase are added.

The design of the tank carried out in the fourth chapter has defined that the necessary thickness of the cylindrical part is of 2,91 mm. There is a small difference with the result of the *MatLab* script, in fact the theory underlying the structural calculation of composite materials is the CLT. The use of the FEM becomes important when optimizing the chosen layup as it is possible to analyze and visualize the structure in its entirety, going to readjust locally, where necessary. Anyway, the script proved to be a useful pre-dimensioning tool for an almost immediate calculation of the geometric and physical properties of the rocket returning acceptable results.

The production technology chosen, for both the carbon tube and the end-closures, is common and well established. The cost, however, may not be so affordable if the number of pieces produced remains low, since a large part of the budget is destined for the production of mandrels and molds. A technical trouble that can be found pursuing this path is the bonding phase, very little is found in the literature about structural bonding that has to guarantee pressure sealing. Then, the need to be compatible with the oxidizer used reduces the number of adhesives to choose from. This aspect will be analyzed in depth with experimental tests, both of compatibility and sealing.

The expected final weight of the oxidizer tank is 5,42 kg. The result obtained in the computer design phase is more than satisfactory compared to a similar metal structure. In fact, by making a small comparison here, it is possible to see that steel structures are heavier, without considering that in these simplified formulas the term of the welding efficiency, which is necessary for the realization of the piece, has not been taken into account. Only the aluminium alloy reaches comparable results (a slightly lighter actually), but, as said, no welding is taken into consideration. Probably the actual weight would be higher, the structure more fragile and more fatigue susceptible.

Metal alloy	Tensile strength, [MPa]	Thickness, [mm]	Weight [kg]
AISI 304L	280	2.06	14.6
AL 2024-T851	380	1.53	3.86

Finally, even if the weight obtained is acceptable, it remains in any case only the first step, as it presents numerous margins for improvement. In fact, a more accurate model of the loads to which the structure will be subjected, also thanks to the tests that will be carried out in the field, makes it possible to orientate the plies optimally to align them with the more stressed directions. Anyway, it should not be forget that in some phases of lamination it will not be possible for the technical personnel to reproduce the desired orientations faithfully.

The study carried out during this thesis has shown the feasibility of a liner-less composite tank for a hybrid propulsion system of a sounding rocket, representing a strong innovation in what is the state of the art.

Bibliography

[1] ANSYS Inc. “ANSYS Composite PrepPost User’s Guide”. In: *ANSYS Manual* 15317.November (2013), pp. 724–746. URL: `http://148.204.81.206/Ansys/readme.html`.

[2] Francesco Barato. “Numerical and Experimental Investigation of Hybrid Rocket Motors Transient Behavior”. In: January (2013).

[3] Benjamin Spilker. *material matmatch*. URL: `https://matmatch.com/blog/metals-in-space-how-superalloys-changed-the-rocket-landscape/`.

[4] Gail Chapline et al. “Materials and Manufacturing”. In: *Advanced Materials Research* 299-300 (2011). ISSN: 10226680. DOI: `10.1201/b15806-10`.

[5] *CLT science*. URL: `https://www.sciencedirect.com/topics/engineering/classical-lamination-theory`.

[6] ESA MiniTEXUS. “European Users Guide to Low Gravity Platforms. Sounding Rockets”. In: (2010), pp. 1–47.

[7] Seconda Facolta, D I Ingegneria, and C O N Sede A Cesena. “Caratterizzazione meccanica a compressione di un composito unidirezionale mediante attrezzatura CLC In Strutture e Materiali Aerospaziali LM”. In: (2012).

[8] Reza Mohammadzadeh Gheshlaghi, Mohammad Hassan Hojjati, and Hamid Reza Mohammadi Daniali. “Analysis of composite pressure vessels”. In: *Fracture of Nano and Engineering Materials and Structures - Proceedings of the 16th European Conference of Fracture* Figure 1 (2006), pp. 335–336.

[9] *ham-let*. URL: `https://www.ham-let.com/`.

[10] Alma Mater et al. "Analisi numerica e sperimentale del comportamento a compressione di materiali compositi". In: ().

[11] Mil_Hdbk-762. "Military Handbook Design of Aerodynamically Stabilized Free Rockets". In: *Contract* 762.July (1990).

[12] F Moretto et al. "Feasibility Study of Hybrid Propulsion System for Sounding Rocket Application". In: ().

[13] *NAROM*. URL: `https://www.narom.no/undervisningsressurser/sarepta/rocket-theory/rocket-dynamics/4-1aerodynamics-and-forces-acting-on-the-rocket/`.

[14] Alfred Puck and H Matthias Deuschle. "Progress in the Puck Failure Theory for Fibre Reinforced Composites : Analytical solutions for 3D-stress". In: *Composites Science and Technology* 62.3 (2002), pp. 371–378.

[15] U.Galvanetto R. Olsson. *laminate notes*.

[16] Angela Schrader. *Autodesk*. 2016. URL: `https://knowledge.autodesk.com/support/helius-pfa/learn-explore/caas/simplecontent/content/what-the-difference-between-first-ply-failure-and-progressive-failure.html` (visited on 12/05/2019).

[17] Michael Standridge. *Materials2*. 2014. URL: `https://www.aerospacemanufa%20cturinganddesign.com/article/amd0814-materials-aerospace-manufacturing/`.

[18] C.T. Sun, B.J. Quinn, and J. Tao. "Comparative Evaluation of Failure Analysis Methods for Composite Laminates." In: *U.S. Department of Transportation* -.May (1996), p. 133. URL: `http://trid.trb.org/view.aspx?id=523207`.

[19] B. W. Tew. "Preliminary design of tubular composite structures using netting theory and composite degradation factors". In: *Journal of Pressure Vessel Technology, Transactions of the ASME* 117.4 (1995), pp. 390–394. ISSN: 15288978. DOI: `10.1115/1.2842141`.

[20] William Wassmer. *Material Azom*. 2015. URL: `https://www.azom.com/article.aspx?ArticleID=12034`.